UNIVERSITÀ DEGLI STUDI DI MODENA E REGGIO EMILIA

DIPARTIMENTO DI INGEGNERIA "ENZO FERRARI"

PhD School

INDUSTRIAL AND ENVIRONMENTAL ENGINEERING

INGEGNERIA INDUSTRIALE E DEL TERRITORIO

XXXIV CYCLE

AN EXTENSIVE METHODOLOGY FOR 3D-CFD LAGRANGIAN SIMULATIONS OF BOTH GASOLINE AND DIESEL SPRAYS

Advisor:

Prof. Stefano Fontanesi

Co-Advisor:

Dr. Fabio Berni, PhD

Candidate:

Simone Sparacino

PhD School Director:

Prof. Alberto Muscio

Index

Abstract 4

Introduction 8

Motivation 8

Objectives 11

Thesis Overview 13

1. Fundamentals of 3D-CFD 14

1.1 Introduction to CFD modeling 14

1.2 Mass conservation 15

1.3 Momentum equation 16

1.4 Energy equation 17

1.5 Set of equations 19

1.6 Transport Equation for a Generic Variable 20

1.7 RANS Simulations and the k-ε and k-ω Models 20

1.8 Dispersed Multi-Phase Flow (Lagrangian Model) 23

1.8.1 Basic Conservation Equations for the Dispersed Phase 24

1.8.2 Basic Conservation Equations for the Continuous Phase 26

1.9 Eulerian Multi-Phase Flow (Volume of Fluid Method) 27

2. Tested Injectors and Operating Conditions 31

2.1 Spray G (Gasoline research injector) 31

2.2 INJ1 (single-hole gasoline research injector) 36

2.3 INJ2 (single-hole gasoline research injector) 38

2.4 INJ3 (5-hole gasoline prototype injector) 41

2.5 Spray A, SprayC and Spray D (single-hole diesel research injectors) 44

3. Models Methodology 47

3.1 Methodologies for droplet initialization 47

3.1.1 Blob Model 48

3.1.2 Distribution Functions 49

3.1.3 Inner-Nozzle Flow Simulations 49

3.1.4 Experimental Momentum Measurements 51

3.2 Secondary break-up models 53

3.2.1 Reitz Diwakar Model 54

3.2.2 KHRT Model 56

3.2.3 GruMo Model 58

3.3 Flash-Boiling Model 63
3.3.1 Flash-boiling Atomization Model 63
3.3.2 Flash-boiling Evaporation Model 65
3.3.3 Flash-boiling Droplet Break-Up Model 65
4. Numerical Setup 67
4.1 Numerical Setup – Primary Break-Up Study 67
4.2 Numerical Setup – Secondary Break-Up Study (GDI) 71
4.3 Numerical Setup – Secondary Break-Up Study (Diesel) 75
4.4 Numerical Setup – Flash Boiling Study 77
5. Results – Primary break-up Analysis 78
6. Results – Secondary break-up Analysis 92
6.1 Secondary break-up in Gasoline Injectors 92
6.2 Secondary break-up in Diesel Injectors 111
7. Results – Flash-Boiling Model 121
8. Conclusions 124
Bibliography 128

Abstract

A proper modelling of the injection process is mandatory in 3D-CFD in-cylinder simulations, in order to predict the correct formation of the air-fuel mixture, that directly affects combustion, knock and emissions. Therefore, the main goal of this thesis is the formulation of an extensive methodology for the numerical characterization of the injection process for both gasoline and diesel sprays. In particular, the attention is focused on three different phenomena, namely primary break-up, secondary break-up, and flash-boiling, which play a significant role in the spray evolution. In the present work, such aspects are investigated and an alternative solution for their modelling is proposed. Numerical simulations are carried out via commercial codes, i.e. STAR-CCM+ and STAR-CD, both licensed by Siemens. Results are validated using extensive experimental datasets consisting of injection rate, spray imaging, liquid penetration curve, and Phase Doppler Anemometry (PDA) data.

As for the primary break-up, an alternative atomization strategy is proposed, aiming at extending simulation predictive capabilities over a wider range of operating conditions. 3D-CFD Lagrangian simulations of two different multi-hole injectors are presented. The first is a 5-hole GDI prototype unit operated at ambient conditions, while the second one is the SprayG injector released by the Engine Combustion Network (ECN), characterized by a higher back pressure. Moreover, to validate the alternative primary break-up strategy adopted for the initialization of the droplets, an internal nozzle flow simulation is carried out on the Spray G injector, able to provide information on both velocity and diameter of the liquid jet at the nozzle exit.

As for the secondary break-up, a novel model, hereafter indicated as “GruMo”, is proposed. It aims at minimizing the secondary break-up calibration efforts in Eulerian-Lagrangian simulations for both gasoline and diesel sprays. For this goal, model parameters are assumed as functions of the ambient density, which directly impacts the disruption of liquid droplets into smaller ones. The set of functions for gasoline injectors is calibrated on a single-hole GDI injector for three different operative conditions. Thereafter model validation is carried out on two different GDI injectors: the first is again a single-hole while the second is the 5-hole GDI prototype mentioned above. In case of Diesel injection, model parameters are calibrated on the well-known SprayA still provided by the ECN, which can be assumed as representative of injectors for light-duty applications. Afterwards, the model is validated on two different single-hole injectors,

namely SprayC and SprayD, both representative of injectors for heavy-duty applications. The new "GruMo" model provides a good agreement between numerical and experimental outcomes for all the tested injectors, without any dedicated tuning. Conversely, the most popular models, such as Reitz-Diwakar and KHRT ones, adopted to simulate the same injectors with default calibration constants, provide results which significantly deviate from the experiments. The effects of turbulence model, minimum mesh size, time-step, and number of injected parcels per time-step, are outlined for the Spray A injector using the new GruMo secondary break-up model.

Finally, the flash-boiling phenomenon is faced. It can potentially play a key role to achieve the required fuel distribution inside the combustion chamber over a wide range of engine operating conditions. In fact, under certain conditions, the fuel undergoes extremely accelerated break-up and quickly evaporates. In the present work, the application of an alternative flash-boiling model, recently implemented by Siemens-PLM in STAR-CD, is shown on a single-hole research injector. The new flash-boiling model consists of three main parts: an atomization model able to compute the droplet initial conditions and the overall spray cone angle; an evaporation model and a droplet secondary break-up model.

It is useful to point out that the proposed and/or tested models can be easily implemented in any 3D-CFD code.

-

Nell'ambito di simulazioni 3D-CFD interno cilindro, una corretta modellazione del processo di iniezione è fondamentale per ottenere una valida previsione del miscelamento aria-combustibile, ovvero di combustione, autoaccensione, ed emissioni. Lo scopo principale di questa tesi è l'elaborazione di una metodologia estensiva per la caratterizzazione numerica del processo di iniezione per spray benzina e diesel. Tre fenomeni importanti per l'evoluzione dello spray sono stati analizzati: il break-up primario, il break-up secondario, ed il flash-boiling. Tali aspetti sono stati analizzati ed una metodologia alternativa per la loro modellazione è proposta. Le simulazioni numeriche sono state effettuate con due codici commerciali, STAR-CCM+ e STAR-CD, entrambi rilasciati da Siemens. I risultati sono validati tramite dati sperimentali in termini di portata di iniezione, immagini di spray, curve di penetrazione, ed analisi Phase Doppler Anemometry (PDA).

Per il break-up primario, una strategia di atomizzazione alternativa è proposta con lo scopo di estendere le capacità predittive delle simulazioni per un'ampia gamma di condizioni operative. A tal scopo sono presentate simulazioni Lagrangiane 3D-CFD per due iniettori multi-foro. Il primo è un prototipo GDI con 5-fori, operante a condizioni ambiente, mentre il secondo è l'iniettore SprayG fornito dall' Engine Combustion Network (ECN), caratterizzato da una maggiore contropressione. Inoltre, con lo scopo di validare la strategia alternativa di break-up primario, è riportata una simulazione interno iniettore per lo SprayG, con la quale si ottengono informazioni sulla velocità ed il diametro della colonna liquida in uscita dal polverizzatore.

Per il break-up secondario, un nuovo modello, d'ora in poi indicato come 'GruMo', è proposto. Lo scopo è quello di semplificare l'attività di calibrazione per il break-up secondario nelle simulazioni Euleriane-Lagrangiane per spray benzina e diesel. Pertanto, i parametri del modello vengono impostati come funzioni della densità ambiente, che incide direttamente sulla rottura delle gocce liquide. Il set di funzioni per iniettori benzina è calibrato su un iniettore mono-foro GDI per tre condizioni operative. In seguito, il modello viene validato su un differente iniettore mono-foro GDI, e sull'iniettore GDI 5-fori menzionato in precedenza. Per gli iniettori diesel i parametri del modello sono calibrati sul noto SprayA, fornito da ECN, il quale è rappresentativo di applicazioni commerciali leggere. Successivamente, il modello viene validato su due iniettori mono-foro, chiamati SprayC e SprayD, entrambi rappresentativi di applicazioni commerciali pesanti. Il modello 'GruMo' fornisce un buon accordo tra dati sperimentali e numerici per tutti gli iniettori testati, senza una calibrazione dedicata. Viceversa, i modelli più diffusi come il Reitz-Diwakar ed il KHRT, adottati per simulare gli stessi iniettori con costanti di calibrazione di default, forniscono risultati che differiscono significativamente dai dati sperimentali.

Infine, il fenomeno di flash-boiling viene analizzato. Esso ricopre potenzialmente un ruolo chiave nel conseguimento di una distribuzione di combustibile target all'interno della camera di combustione per un ampio intervallo di condizioni operative. Infatti, in determinate condizioni, il combustibile subisce un break-up estremamente rapido che porta ad un'accelerata vaporizzazione. In questo lavoro di tesi, è presentata l'applicazione di un modello di flash-boiling alternativo, recentemente implementato da Siemens-PLM in STAR-CD, su un iniettore mono-foro da ricerca. Il nuovo approccio consiste in tre parti principali: un modello di atomizzazione che determina le condizioni iniziali delle gocce e l'angolo di cono complessivo; un modello di vaporizzazione ed un modello di break-up secondario.

È utile sottolineare che i modelli proposti e/o testati nel presente lavoro possono essere facilmente implementati in qualsiasi codice 3D-CFD.

Introduction

Motivation

Nowadays Internal Combustion Engines (ICE) play an important role as form of propulsion worldwide, and they are subjected to significantly stringent regulations in terms of CO_2 and pollutant formations. For this reason, the complexity of powertrains is rapidly increasing with the introduction of innovative combustion processes [1,2], alternative ignition technologies [3,4], water injection [5], and hybridization [6]. Among different solutions, the exploration of physical phenomena characterizing the fuel injection process for both Gasoline Direct Injection (GDI), and Turbocharged Direct Injection (TDI) still represents a valid path towards the necessary emission reduction. The introduction of fuel in the combustion chamber is a crucial aspect for direct injection engines, given that the liquid break-up and its evaporation rate directly affect the mixture formation and the combustion efficiency, and consequently the engine behaviour in terms of performance, fuel consumption, and pollutant formation [7,11].

In this challenging scenario, Computational Fluid Dynamics (CFD) can support the ICE progress by reducing cost-and time-to-market. This is particularly important in the automotive industry as the vehicle manufacturers budgets are divided between electrification and research on ICEs and, therefore, there is a stronger exploitation of virtual technologies for both design and validation stages. CDF simulations are relatively low cost compared with physical experiments, in which the setup to get essential engineering data can be expensive. In addition, CFD simulations can be executed in a short period of time, and the desired outcomes can be introduced early in the design process. Another important aspect in using a virtual approach consists in the ability to theoretically simulate any physical condition, with a great control over the process and the possibility to isolate specific phenomena.

Spray simulations are based on Eulerian-Lagrangian approaches that rely on different models describing the spatial and temporal evolution of the injected fuel. Among the physical phenomena to be modelled, primary break-up, secondary break-up, and flash boiling play a critical role.

The primary break-up is the process that leads to the formation of small fuel drops from the liquid column exiting the nozzle hole; depending on the relative velocity between the liquid and the ambient, and the properties of the fuel, it is possible to characterize the primary break-up

regimes that directly impact the break-up length (distance from the nozzle exit at which the first liquid drops are generated) and the size of the first droplets detached from the fuel column. All the parameters that influence the primary break-up process are grouped into the not-dimensional Weber liquid number, defined as:

$$We_l = \frac{\rho_l \, u_{rel}^2 D}{\sigma_l} \tag{1}$$

where u_{rel} is the relative velocity between fuel and air, D is the diameter of the liquid column, ρ_l and σ_l are the density and the surface tension of the injected fuel, respectively. Another important parameter to consider is the density of the ambient in which the liquid is introduced: a higher value involves an increase in the break-up rate due to the rise of disruptive forces.

The secondary break-up is the mechanism for which the first liquid drops (parent droplets), undergo a rapid decrease of diameter and a consequent disruption in smaller ones (child droplets). This process is mainly influenced by the aerodynamic interaction between the drop and the medium, and the characteristic parameters are grouped into the not-dimensional Weber gaseous number, defined as:

$$We_g = \frac{\rho_g \, u_{rel}^2 D_d}{\sigma_l} \tag{2}$$

where ρ_g is the ambient density, and D_d is the parent droplet diameter.

In numerical Lagrangian simulations of injection processes, the description of the liquid phase requires the existence of drops. For this reason, simulation of spray formation always begins with droplets starting to penetrate into the combustion chamber, and the task of primary break-up models is to determine the starting conditions of these drops, such as initial diameter and velocity components (spray angle), which are mainly influenced by the flow conditions inside the nozzle holes. Several models are available in literature for the simulation of break-up mechanisms in 3D-CFD analyses [12,16]. As for the initial droplet diameter, a common approach in the industrial field consists in the adoption of droplet diameter distribution functions deducted by experimental Phase Doppler Anemometry (PDA) data. In fact, such strategy provides a rapid spray calibration at the expense of the predictive capabilities of the numerical model. However, for the purpose of

experimental data validity, measurements are usually carried out at least 20 mm in the axial direction far from the injector tip, where droplets have already experienced a substantial secondary break-up. Consequently, Lagrangian simulations are frequently characterized by values of droplet initial diameters even one order of magnitude smaller than the geometrical nozzle hole diameter. Such approach is proved to be strongly dependent from the pressure value in the combustion chamber at the start of injection [17].

Secondary break-up mechanisms are often simulated in the 3D-CFD framework with the popular models of Reitz-Diwakar [18], and KHRT [19], both implemented in the code through differential equations that describe the computational parcels disruption rate due to aerodynamic forces at the liquid-air interface. These equations are characterized by constants calibrated on experimental evidence, which can be exploited for tuning. Therefore, predictive capabilities of the secondary break-up models are limited to specific operating conditions, in terms of injection parameters and ambient gas thermodynamic state. In an ICE working cycle, large variations of operating conditions occur, leading to a complicated ad-hoc model constant calibrations in order to obtain a proper simulation of the spray development inside the combustion chamber for all the injection duration.

Particularly for GDI engines, the challenging task to obtain the required fuel distribution and atomization inside the combustion chamber over a wide range of engine operating conditions can be achieved via flash-boiling. Such phenomenon occurs when the liquid fuel is injected in an ambient characterized by a static pressure lower than the fuel saturation pressure for a specific temperature, and it causes instabilities of the fluid that operates under superheated conditions (the superheat rate is defined as the difference between the temperature of injected droplets and the saturation temperature of the fuel at ambient pressure). The rapid reduction in pressure or the increase in the superheat rate cause the fuel to enter a metastable state with a significant thermal energy, which is absorbed through the sudden flash-boiling process. The result of this significant energy transfer is a fast vapor nucleation inside the liquid: during the injection, vapor bubbles grow up and burst due to the rapid drop of the liquid pressure from the nozzle to the ambient level. However, due to high injection pressure, flash-boiling can also occur inside the nozzle where the gaseous phase generates an under-expanded jet of fuel vapor at the nozzle exit, together with the liquid phase. Spray morphology and air-fuel mixing are strongly influenced by

flash-boiling phenomenon, and the effect of different injector structures with different types of fluid were reported in [20,26].

Objectives

The main goal of this thesis is the formulation of an extensive methodology for the numerical characterization of the injection process for both gasoline and diesel sprays, with the aim to reduce the dependency from the operating conditions and, consequently, reduce the calibration efforts. Primary break-up, secondary break-up, and flash-boiling phenomena are extensively investigated in the 3D-CFD numerical framework via commercial codes, i.e., STAR-CCM+ and STAR-CD, both licensed by Siemens. All the numerical results are validated against experimental data in terms of injection rate, spray imaging, liquid penetration curve, and PDA data. The experimental datasets are provided by the SprayLAB of Perugia University, and by the Engine Combustion Network (ECN).

As for the primary break-up, the common approach of small droplet initial diameters described before, is exploited for two different GDI injectors. The first one is a 5-hole GDI prototype injector provided by the SprayLAB [27], operating with a backpressure equal to the ambient pressure; the second one is the well-known SprayG provided by ECN, characterized by a backpressure equal to 0.6 MPa. The adoption of small diameters (close to 10 μm), inherited from PDA measurements, provides consistent results if the backpressure is close to the ambient one, while it shows unacceptable misalignment with experimental outcomes if the value of the backpressure increases. Therefore, larger droplet diameters (closer to the hole size of 165 μm) are tested for the Spray G, able to supply a representation of the spray in line with the experiments; in order to confirm the importance of bigger droplet diameters, an internal nozzle flow simulation of the Spray G injector is carried out. The outputs of such simulation consist in droplet initial conditions to be applied to Lagrangian simulations, in terms of droplet velocities and diameters. These last are found to be moderately greater than 130 μm, thus closer to nozzle hole dimension and one order of magnitude larger than values provided by PDA measurements ad 15 mm far from the injector tip. This leads to the conclusion that a simpler blob model with droplet dimension equal to hole diameter may perform much better in terms of 3D-CFD numerical results than distribution functions with small diameters. Eulerian Multiphase nozzle internal flow simulations represent a valid approach to evaluate droplet initial conditions; however, they require the internal nozzle

geometry to be executed. If the latter is not available, an alternative approach developed by the SprayLAB can be exploited, which is based on experimental momentum measurements as described in [28,29].

As for the secondary break-up, an alternative model is proposed, hereafter briefly indicated as "GruMo". This approach aims at minimizing the secondary break-up calibration efforts in Eulerian-Lagrangian simulations for both gasoline and diesel sprays, via the introduction of model parameters that are assumed as functions of the ambient density, which directly affects the disruption of liquid droplets into smaller ones. In addition, a zonalization of the break-up regimes is introduced: near the nozzle, where the relative velocity between fuel and air is high, and the droplets are big, only stripping break-up is enabled; on the other hand, adequately far from it, only bag break-up mechanism is considered. For the sake of brevity, and to simplify the approach, only the effect of ambient density is accounted for, while the influence of other factors impacting the break-up such as injection pressure and temperature, turbulence model, and computational mesh size, is not currently explored. The set of functions for gasoline injectors is calibrated on a single-hole GDI injector (hereafter named as INJ1) for three different operating conditions, and successively model validation is carried out on two different GDI injectors: the first is another single-hole (hereafter named as INJ2) while the second is the 5-hole prototype (hereafter named as INJ3) mentioned above. In case of Diesel injection, model parameters are calibrated against the well-known Spray A, provided by the ECN, which can be assumed as representative of injectors for light-duty applications. Afterwards, the model is validated at the same operating condition on two different single-hole injectors, namely Spray C and Spray D, both representative of injectors for heavy-duty applications. The new "GruMo" model provides a good agreement between numerical and experimental outcomes for all the tested injectors, without any dedicated tuning. Conversely, as mentioned above, the most popular models, such as Reitz-Diwakar and KHRT ones, adopted to simulate the same injectors with default calibration constants, provide results which significantly deviate from the experiments. As for the Spray A injector, the influence of the turbulence model, the minimum mesh size, the simulation time-step, and the number of injected parcels per time-step is addressed in this manuscript. It is renowned that such parameters strongly influence numerical results in spray simulations in terms of spray morphology and penetration, and it is important to understand such dependency to obtain a proper simulation of the injection process in engine simulations.

Finally in this work, a flash boiling model recently implemented in STAR-CD V.2019.1 [30] is tested and validated against experimental outcomes provided again by the SprayLAB. The novel flash-boiling model consists of three main parts: an atomization model able to compute droplet initial conditions and the overall spray cone angle; an evaporation model that considers the superheat degree, and finally a droplet break-up model that simulates the bubble nucleation and growth inside the liquid droplets. The single-hole research injector INJ2 is analysed in a constant volume chamber with a backpressure equal to 0.04 MPa, in order to replicate an engine part-load operation. Specifically, to evaluate the effect of the fuel temperature on the flash-boiling phenomenon, two different conditions are investigated: a subcooled one characterized by a fuel temperature equal to 303.15 K, and a flashing one in which the fuel temperature is equal to 393.15 K. Numerical results for both subcooled and flashing conditions show a good agreement with experimental data, and the new flash-boiling model is able to reproduce the physical phenomena occurring in this peculiar condition.

Thesis Overview

A brief overview of the thesis is provided in the following sections. This manuscript contains eight chapters that cover the fundamentals of CFD modeling (Chapter 1), the tested injectors with the relative operating conditions (Chapter 2), the methodology for the investigated numerical models (Chapter 3), the numerical setup adopted for each numerical simulation (Chapter 4), a discussion about numerical results concerning the primary break-up (Chapter 5), the secondary break-up (Chapter 6), and the flash-boiling (Chapter 7), and finally the overall conclusions (Chapter 8).

1. Fundamentals of 3D-CFD

1.1 Introduction to CFD modeling

Governing equations describing the flow motion are named “Navier-Stokes” equations. They are based on three of fluid physics, i.e., mass conservation (also known as continuity), momentum conservation (also known as Newton’s second law) and energy conservation (also known as first law of thermodynamics). An important assumption is that the fluid is considered as a “continuum”, since the analyses are carried out on “macroscopic” scales (i.e., bigger than 1µm) and the molecular structure of the fluid and the molecular motion can be ignored and disregarded. Fluid behaviour is described in terms of macroscopic properties such as velocity, pressure, density, temperature, and their spatial and temporal derivatives, all considered as average values over a huge number of single molecules which can be approximated as a point in space (or a single fluid particle), defined as the smallest fluid element which is not influenced by the single molecules’ action.

A fluid element of size δx_i, δx_j , δx_k , with generic coordinates and volume is considered and a sketch of it is reported in Figure 1.

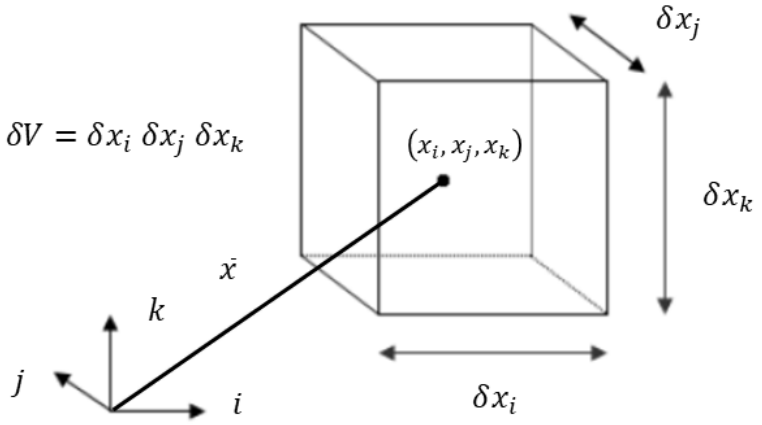

Figure 1. Finite control volume

All the fluid properties are functions of both time and space:

$$p = p\ (x_i, x_j, x_k, \mathrm{t}) \tag{3}$$

$$\rho = \rho\ (x_i, x_j, x_k, \mathrm{t}) \tag{4}$$

$$T = T\ (x_i, x_j, x_k, \mathrm{t}) \tag{5}$$

$$\bar{u} = \bar{u}\ (x_i, x_j, x_k, \mathrm{t}) \tag{6}$$

This dependency will not be further remarked for the sake of simplicity.

1.2 Mass conservation

Mass conservation equation is based on the balance between fluid mass entering and exiting the domain, i.e., the fluid element or "control volume". The net rate of mass increase/decrease over time is:

$$\frac{\delta}{\delta t}\ (\rho \cdot \delta x_i \cdot \delta x_j \cdot \delta x_k) = \frac{\delta \rho}{\delta t} \delta x_i \cdot \delta x_j \cdot \delta x_k \tag{7}$$

Mass flow through a surface is the product of density, area, and velocity component normal to the surface. It is positive if mass flow is entering and negative if exiting. The net balances contributions through each surface bounding the element are:

$$\begin{aligned}
&\left[\rho\, u_i - \frac{\delta \rho\, u_i}{\delta x_i} \cdot \frac{1}{2} \cdot \delta x_i\right] \cdot \delta x_j \delta x_k - \left[\rho\, u_i + \frac{\delta \rho\, u_i}{\delta x_i} \cdot \frac{1}{2} \cdot \delta x_i\right] \cdot \delta x_j \delta x_k + \\
&\left[\rho\, u_j - \frac{\delta \rho\, u_j}{\delta x_j} \cdot \frac{1}{2} \cdot \delta x_j\right] \cdot \delta x_i \delta x_k - \left[\rho\, u_j + \frac{\delta \rho\, u_j}{\delta x_j} \cdot \frac{1}{2} \cdot \delta x_j\right] \cdot \delta x_i \delta x_k + \\
&\left[\rho\, u_k - \frac{\delta \rho\, u_k}{\delta x_k} \cdot \frac{1}{2} \cdot \delta x_k\right] \cdot \delta x_i \delta x_j - \left[\rho\, u_k + \frac{\delta \rho\, u_k}{\delta x_k} \cdot \frac{1}{2} \cdot \delta x_k\right] \cdot \delta x_i \delta x_j
\end{aligned} \tag{8}$$

Equating the two expressions and dividing by the control volume δV, it is possible to obtain the following compact notation:

$$\frac{\delta}{\delta t} \nabla \cdot\ (\rho\, u) = 0 \tag{9}$$

which represents the compact form of the 3D continuity (or mass conservation) equation for a compressible fluid. The first term on the left is the rate of density (i.e. mass per unit volume) increase/decrease within the control volume, while the second is the algebraic sum of the fluxes entering/exiting the volume through the bounding surfaces and is also named "convective term", i.e. due to the fluid motion.

1.3 Momentum equation

Following Newton's Second Law, the acceleration a of a body is parallel and directly proportional to the net force 'F' and inversely proportional to the mass 'm'. Also here, the variation of a physical quantity is caused by both the temporal variation of the quantity and the net flow through the surface bounding the control volume. Similarly to mass, the momentum variation for a fluid element can be expressed as:

$$\rho\,\bar{u} \;\Rightarrow\; \frac{\delta}{\delta t}(\rho\,\bar{u}) + \nabla\cdot\rho\,\bar{u}\bar{u} = \rho\bar{f} + \;\nabla\cdot\bar{\Pi} \tag{10}$$

The first term represents the rate of increase of momentum per unit volume. The second term represents the variation of momentum due to convection through the control volume surface, and it can also be written as:

$$\bar{u}\,\frac{\delta\rho}{\delta t} + \;\rho\frac{\delta\bar{u}}{\delta t} + \;\rho\bar{u}\cdot\nabla\bar{u} + \bar{u}\nabla\cdot\rho\,\bar{u} = \bar{u}\,\left(\frac{\delta\rho}{\delta t} + \nabla\rho\,\bar{u}\right) + \rho\left(\frac{\delta\bar{u}}{\delta t} + \bar{u}\nabla\bar{u}\right) \tag{11}$$

$$\nabla\cdot\rho\bar{u}\bar{u} = \rho\bar{u}\cdot\nabla\bar{u} + \bar{u}(\nabla\cdot\rho\,\bar{u}) \tag{12}$$

Using the above expression in the momentum equation combined with the continuity equation, the following expression is obtained:

$$\rho\frac{D\bar{u}}{Dt} = \rho\bar{f} \;+\; \nabla\cdot\bar{\Pi} \tag{13}$$

As for the forces acting on the fluid parcel, we usually distinguish between mass forces 'f' and surface forces, where the first type is grouped in a single term called the "mass force source". Mass forces act "remotely" on the whole fluid mass. A typical example is gravity, for which the force per unit mass is the gravitational acceleration vector. The second term represents the surface forces acting on the fluid element. Stresses can be split in normal stresses and shear stresses and are grouped in the tensor. The expression for the momentum conservation is of general use and loses its generality only when peculiar expressions are defined for the stress tensor: for example, for many gases and liquids a correlation between stresses and rate of

deformation was observed. Fluids exhibiting that behaviour are usually referred to as Newtonian Fluids.

1.4 Energy equation

The energy equation is derived from the first law of thermodynamics, expressed as:

$$\frac{dE}{dt} = \frac{dQ}{dt} + \frac{dL}{dt} \tag{14}$$

Following the same procedure of before, energy variation in time for a fluid particle and per unit volume can be expressed as the product of density and energy material derivative:

$$\rho \frac{dE}{dt} \tag{15}$$

The work done on the fluid particle in the infinitesimal time interval is exerted by the forces acting on the element surface times the velocity component parallel to the forces themselves. The work can be derived from the previous equations, and considering the component along the i-direction it is possible to write that:

$$\begin{aligned}
&\left[\left(pu_i - \frac{\delta(pu_i)}{\delta x_i}\cdot\frac{1}{2}\delta x_i\right) - \left(\tau_{ii}\,u_i - \frac{\delta(\tau_{ii}\,u_i)}{\delta x_i}\cdot\frac{1}{2}\delta x_i\right)\right]\delta x_j\delta x_k + \\
&\left[-\left(pu_i - \frac{\delta(pu_i)}{\delta x_i}\cdot\frac{1}{2}\delta x_i\right) + \left(\tau_{ii}\,u_i + \frac{\delta(\tau_{ii}\,u_i)}{\delta x_i}\cdot\frac{1}{2}\delta x_i\right)\right]\delta x_j\delta x_k + \\
&\left[-\left(\tau_{ji}u_i - \frac{\delta(\tau_{ji}u_i)}{\delta x_j}\cdot\frac{1}{2}\delta x_j\right) + \left(\tau_{ji}\,u_i + \frac{\delta(\tau_{ji}\,u_i)}{\delta x_j}\cdot\frac{1}{2}\delta x_j\right)\right]\delta x_i\delta x_k + \\
&\left[-\left(\tau_{ki}u_i - \frac{\delta(\tau_{ki}u_i)}{\delta x_k}\cdot\frac{1}{2}\delta x_k\right) + \left(\tau_{ki}\,u_i + \frac{\delta(\tau_{ki}\,u_i)}{\delta x_k}\cdot\frac{1}{2}\delta x_k\right)\right]\delta x_i\delta x_j
\end{aligned} \tag{16}$$

Summing the three previous equations and dividing by δV, we get the total work exerted on the fluid particle by the surface forces. The work by the mass forces, mainly due to the variation of potential energy, is described, as for the momentum equations, by a scalar source term 'S_E', "source of energy per unit volume" in the considered time interval. The final expression is:

$$[-\nabla \cdot (\rho\, \bar{u})] + \left[\frac{\delta(u_i\tau_{ii})}{\delta x_i} + \frac{\delta(u_i\tau_{ji})}{\delta x_j} + \frac{\delta(u_i\tau_{ki})}{\delta x_k} + \frac{\delta(u_j\tau_{ij})}{\delta x_i} + \frac{\delta(u_j\tau_{jj})}{\delta x_j} + \frac{\delta(u_j\tau_{kj})}{\delta x_k} + \frac{\delta(u_k\tau_{ki})}{\delta x_i} + \frac{\delta(u_k\tau_{kj})}{\delta x_j} + \frac{\delta(u_k\tau_{kk})}{\delta x_k}\right] + S_E \quad (17)$$

The heat exchanged by the fluid particle with the environment is now considered. The vector $\bar{q}$ represents the heat flux exchanged through conduction. The overall heat flux can be obtained by summing all the contributions (positive if entering in the control volume, negative if exiting from the control volume) through the element bounding surfaces. For example, the contribution along the i-direction is:

$$\left[\left(q_i - \frac{\delta q_i}{\delta x_i}\cdot\frac{1}{2}\delta x_i\right) - \left(q_i + \frac{\delta q_i}{\delta x_i}\cdot\frac{1}{2}\delta x_i\right)\right]\cdot \delta x_j \delta x_k = -\frac{\delta q_i}{\delta x_i}\cdot \delta x_i \delta x_j \delta x_k \quad (18)$$

The overall flux due to conduction exchanged by the fluid element per unit volume is equal to:

$$-\nabla \cdot \bar{q} = -\frac{\delta q_i}{\delta x_i} - \frac{\delta q_j}{\delta x_k} - \frac{\delta q_k}{\delta x_k} \quad (19)$$

The application of the Fourier's Law for heat conduction allows to link the thermal flux to the local temperature gradient, which can be expressed in compact notation as:

$$\bar{q} = -k\nabla \mathrm{T} \quad (20)$$

Where 'k' is the "heat transfer coefficient". Combining the above expressions it is possible to obtain a new formulation for the heat exchange due to conduction by the fluid element per unit volume, defined as:

$$-\nabla \cdot \bar{q} = \nabla \cdot (k\nabla \mathrm{T}) \quad (21)$$

Substituing the above expressions the energy equation for a fluid particle can be derived as:

$$\rho \frac{DE}{Dt} = -\nabla \cdot (\rho \bar{u}) + \frac{\delta(u_i \tau_{ii})}{\delta x_i} + \frac{\delta(u_i \tau_{ji})}{\delta x_j} + \frac{\delta(u_i \tau_{ki})}{\delta x_k} + \frac{\delta(u_j \tau_{ij})}{\delta x_i} + \frac{\delta(u_j \tau_{jj})}{\delta x_j} + \frac{\delta(u_j \tau_{kj})}{\delta x_k} + \frac{\delta(u_k \tau_{ki})}{\delta x_i} + \frac{\delta(u_k \tau_{kj})}{\delta x_j} + \frac{\delta(u_k \tau_{kk})}{\delta x_k} + \nabla \cdot (k \nabla \mathrm{T}) + S_E \quad (22)$$

1.5 Set of equations

The previously described equations are implemented in each control volume so that a system of five scalar equations is obtained: one equation of mass conservation, three equations for the momentum and, finally, one equation for the energy. These partial differential equations describe the 3D motion of a fluid. The unknowns are pressure, density, three velocity components and temperature. In order to close the system, a further equation is required. For example, if the assumption of "ideal gas" is adopted for the fluid, the relative well-known state equation can be adopted:

$$\frac{\mathrm{p}}{\rho} = R\mathrm{T} \quad (23)$$

where 'R' is the gas constant. It is important to remind that in the case of uncompressible fluids (liquids and/or low-speed gases) density can be considered as a constant, which means that no connection exists between energy equation on one side and mass and momentum equations on the other side, since temperature (which defines the internal energy 'i') is not dependent on density itself. Under that assumption, the flow field is computed only through the continuity and momentum equations, while energy equation can be solved subsequently, once the velocity vector and the pressure field are known throughout the computational domain.

1.6 Transport Equation for a Generic Variable

Repeating the previous path for a generic variable ϕ, we get a similar equation which describes the transport of ϕ within the fluid flow-field:

$$\frac{\delta(\rho\phi)}{\delta t} + \nabla \cdot (\rho \cdot \phi \cdot \bar{u}) = \nabla \cdot \left(\Gamma_\phi \cdot \nabla_\phi\right) + S_\phi \tag{24}$$

The first term defines the temporal variation of ϕ within the control volume δV; the remaining three terms quantify the variation of ϕ by means of different phenomena. It is clear that ϕ will change within the control volume if any fluid particles crossing the fluid element at the given time, drag the variable ϕ into or out of δV. This effect is expressed by the second term, which is named convective transport, i.e. due to motion of the fluid particles. Nevertheless, even a still fluid can transport any variable ϕ by means of diffusion, i.e. due to molecular agitation, and this transport is quantified by the third term, named diffusive transport, where the constant Γ_ϕ is referred to as "diffusivity of ϕ". The fourth term quantifies the so-called sources of ϕ; within this term, both "positive or production" and "negative or dissipation" sources are included. In common practice, the term S_ϕ defines the quantity of ϕ which is generated or destroyed within the control volume in the time interval 't'; it is important to remark that these are not flows entering into or exiting from δV, but they are internal variations which have nothing to deal with either transport or diffusion through the elements surrounding the considered control volume.

1.7 RANS Simulations and the k-ε and k-ω Models

The Reynolds-Averaged Navier-Stokes equations (RANS) are derived from the time-averaging operation performed on the Navier-Stokes original set of equations. Time-averaging is based on the decomposition of a generic fluctuating variable into a mean part and a fluctuation around the mean value. The resulting set of equations expresses the time-averaged behaviour, or in case of quasi-periodic flows such as those in internal combustion engines, phase-averaged flow realizations. RANS equations need closure terms to model the Reynolds Stresses, i.e. the product terms between velocity fluctuations. In this context the 2-equations k-ε turbulence model is developed and it is still nowadays the most widespread and used model for turbulent flows in

commercial CFD software. The idea is that of introducing two transport equation for k and ε. These have the form of:

$$\frac{\delta(\bar{\rho}k)}{\delta t} + \nabla \cdot (\bar{\rho}k\bar{u}) = \nabla\left(\frac{\mu_t}{\sigma_k}\nabla \mathrm{k}\right) + 2\mu_t\widetilde{S_{ij}}\widetilde{S_{ij}} - \bar{\rho}\varepsilon \tag{25}$$

$$\frac{\delta(\overline{\rho\varepsilon})}{\delta t} + \nabla \cdot (\bar{\rho}\varepsilon\bar{u}) = \nabla\left(\frac{\mu_t}{\sigma_\varepsilon}\nabla\varepsilon\right) + C_{1\varepsilon}\frac{\varepsilon}{k}2\mu_t\widetilde{S_{ij}}\widetilde{S_{ij}} - C_{2\varepsilon}\frac{\varepsilon}{k}\bar{\rho}\varepsilon \tag{26}$$

The modelled equations give a relation for the energy transfer represented by the energy-cascade process, which is determined by the problem-dependent large-scale motions. The equations above, represents the turbulent kinetic energy and its dissipation rate process at a small scale.

The origin of the model comes from experimental observations: at high Reynolds numbers, the energy dissipation rate and the turbulent kinetic energy undergo variations in time which are more or less proportional. An increase of k corresponds to an increase of ε of equal intensity, and vice versa; the same happens for decreasing rates. This fact, from a mathematical perspective, is converted into a direct proportionality between the productive and dissipative terms of k and ε: this assumption is called “turbulent equilibrium hypothesis”. The mentioned time correlation which stands between ‘k’ (defined in m^2/ s^2) and the dissipation rate ‘ε’ (defined in m^2/ s^3) represents the inverse of the timescale of the large-scale eddies, i.e. it indicates the turn-over frequency of the large-scale eddies, measured in s^{-1}.

One major advantage of k-ε model is that it is based on the Boussinesq assumption typical of eddy viscosity turbulence models. It allows to simplify the evaluation of the turbulent stresses, reducing computational times and explaining why such models are the most used from an industrial point of view for the analysis of turbulent flows. Another advantage is their considerable robustness: from a computational point of view they are, surely, highly stable, and efficient. On the contrary, some inner simplifications in the transport equations can lead to poor accuracy in the representation. Major error sources in two-equation models are the turbulent equilibrium assumption and the Boussinesq hypothesis. As for the turbulent equilibrium assumption, this is sufficiently true only for free flows at high Reynolds numbers. Boussinesq hypothesis introduces the concept of eddy viscosity in perfect analogy with the molecular; the definition as a scalar,

implicitly, imposes an isotropy condition to the eddy viscosity. This assumption leads to a linearity between the strain rate and the Reynolds stresses, which is never verified, except for very simple flows, far from solid walls; for complex fields, highly distorted, where geometry effects are relevant (bended pipes, etc.), a linear relation is wrong.

3D Lagrangian simulations presented in the following hereafter are based on a RANS approach, coupled with a k-ε model [31,37] that comprises transport equations for the turbulent kinetic energy 'k' and its dissipation rate ε. In these models, k and ε are chosen as typical turbulent velocity scale and length scale, respectively. The options differ from each other in one of the following respects:

- The form of the equations
- The treatment of the near-wall region
- The relation between Reynolds stresses and the rates of strain

Those models that use a linear relationship between Reynolds stresses and strains are classified as linear models; those that do not are classified as non-linear. The main alternatives in the linear category that can be employed for Lagrangian simulations are:

- The "standard" model [31,33], in which the high Reynolds number forms of the k and the ε equations are used in conjunction with algebraic law-of-the-wall representation of flow, heat and mass transfer [31].
- The "Renormalisation Group" (RNG) version of the k-ε model [34,35], here after denoted as RNG k-ε. This is employed in high Reynolds number form in conjunction with law-of-the-wall functions. A low Reynolds number version of the RNG model is also provided in which transport equations for k and ε are solved everywhere, including the near-wall regions [38]. The wall law is therefore not required for the near-wall regions with this model.
- The so-called "realizable" k-ε model, a variant of the linear k-ε model where C_μ is no longer constant but a function designed to prevent physically unrealistic values for the Reynolds Stress tensor components.

As for the Eulerian internal nozzle flow simulations, the alternative approach of k-ω model is employed, where ω is the specific dissipation rate proportional to ε/k. In particular, the SST variant [39] is utilized, which have options for law-of-the-wall and low Reynolds number wall treatment.

1.8 Dispersed Multi-Phase Flow (Lagrangian Model)

Dispersed multi-phase flows are found in a wide variety of industrial plant process, including liquid and solid-fuelled combustors, spray driers, cyclone dust separators, and chemical reactors. In all cases the flow consists of a “continuous” phase, which may be gaseous or liquid, and one or more “dispersed” phases in the form of solid particles, liquid droplets, or gas bubbles. In general, the motion of the dispersed phase will be influenced by that of the continuous one and vice versa via displacement and interphase momentum, mass, and heat transfer effects. The strength of the interactions will depend on the dispersed particle’s size, density, and number density. If the flow is laminar, each element released from a point will follow a smooth unique trajectory, i.e. the motion is deterministic. On the other hand, individual elements introduced into a turbulent carrier flow will each have their own, random path due to interaction with the fluctuating turbulent velocity field. Elements may also interact with each other (i.e. collision). If the dispersed phase is volatile, soluble, or reactive, mass transfer occurs between the phases. This is accompanied by interphase heat transfer, which may also arise due to the interphase temperature differences. Interphase mass transfer causes size changes in the dispersed elements. Thus, even if the initial size distribution is uniform (monodispersed), these effects will produce a variable-size population. The size change may also be produced by fluid-dynamic forces acting on the dispersed elements, causing them to break up into smaller elements. Inter-element collision processes may also produce the opposite effect, i.e. size increase due to coalescence or agglomeration. Finally, additional phenomena may occur if the dispersed elements strike a wall. For example, the result may be bouncing or shattering, according to the impact conditions.

In the Lagrangian/Eulerian framework [40] the conservation equations of mass, momentum and energy for the dispersed phase are written for each individual element. The governing equations for the carrier phase are expressed in Eulerian form and are suitably modified to consider of the presence of the dispersed phase. For flows involving a (comparatively) small number of dispersed elements, it is possible to solve a set of the aforementioned Lagrangian equations for every element. However, if the number of particles is large, a statistical approach is more practical. In this, the total population is represented by a finite number of computational parcels (samples), each of which represents a group (cluster) of elements having the same properties. However, the number of samples is not arbitrary; it must be large enough so that the properties of the full population are well represented. This can be assessed, in the absence of any

other measures, by performing calculations with different numbers of samples and comparing the results.

In turbulent flows, the random walk technique [41] is employed to introduce the fluctuating nature of the turbulent velocity field, which results in turbulent dispersion of the dispersed elements. For the sake of brevity, the dispersed phase will hereafter often be referred to as 'droplets'; indeed, some of the system-specific functions and correlations ('sub-models') will specifically refer to liquid droplets in a gaseous carrier stream. However, the overall framework is designed to accept alternative sub-models appropriate to other systems, e.g. involving solid particles or gas bubbles.

1.8.1 Basic Conservation Equations for the Dispersed Phase

The instantaneous fluid velocity and droplet velocity are denoted by u and u_d, respectively. The subscript 'd' denotes the droplet/dispersed phase, while non-subscripted quantities are taken to refer to the continuous phase, and the droplet position vector is denoted by x_d. The momentum equation for a droplet with mass m_d is:

$$m_d \frac{du_d}{dt} = F_{dr} + F_p + F_{am} + F_b \tag{27}$$

where F_{dr} is the drag force given by

$$F_{dr} = \frac{1}{2} C_d \, \rho \, A_d \, |u - u_d|(u - u_d) \tag{28}$$

where C_d is the drag coefficient (function of the droplet Reynolds number) and A_d the droplet cross-sectional area. F_p is the pressure force given by:

$$F_p = -V_d \nabla p \tag{29}$$

where V_d is the droplet volume and ∇p the pressure gradient in the carrier fluid (the pressure includes any hydrostatic components). F_{am} is the so-called "virtual mass" force, i.e. that required to accelerate the carrier fluid entrained by the droplet; the expression for this force is:

$$F_{am} = -C_{am}\rho V_d \frac{d(u_d - u)}{dt} \tag{30}$$

where C_{am} is the virtual mass coefficient, usually set to 0.5 [42]. F_b is a general body force term which represents the effects of gravity and accelerations present in a non-inertial coordinate frame. In the case of a rotating frame, the expression for such force becomes:

$$F_b = m_d[g - \omega \times (\omega \times r) - 2(\omega \times u_d)] \tag{31}$$

where g is the gravitational acceleration vector, ω the angular velocity vector, and r is the distance vector to the axis of rotation. Knowledge of the droplet velocity allows its instantaneous position vector x_d to be determined by integrating the following:

$$\frac{dx_d}{dt} = u_d \tag{32}$$

In the presence of mass transfer with a rate equal to F_m per unit surface area, the droplet mass rate of change is given by:

$$\frac{dm_d}{dt} = -A_s F_m \tag{33}$$

where A_s is the droplet surface area. For an evaporating/condensing single-component droplet, F_m can be expressed as [43]:

$$F_m = K_g p_t \ln \frac{(p_t - p_{v,\infty})}{(p_t - p_{v,s})} \tag{34}$$

where K_g is the mass transfer coefficient obtained by a correlation, and p_t, $p_{v,\infty}$, and $p_{v,s}$ are the gas pressure and partial pressures of the vapour in the droplet surroundings and at its surface, respectively. The surface vapour pressure is assumed to be equal to the saturation pressure at the droplet temperature T_d.

As for the energy conservation equation, the droplet energy balance considers the mechanisms of surface heat transfer rates q_d'' per unit surface area and loss/gain due to phase change, thus:

$$m_d c_{p,d} \frac{dT_d}{dt} = -A_s \dot{q}_d'' + h_{fg} \frac{dm_d}{dt} \tag{35}$$

where $c_{p,d}$ is the droplet specific heat, and h_{fg} the latent heat of phase change. The surface heat flux $\dot{q}_d''$ is given by the following equation:

$$\dot{q}_d'' = h(T_d - T) \tag{36}$$

where h is the heat transfer coefficient, obtained via a correlation.

1.8.2 Basic Conservation Equations for the Continuous Phase

The continuous phase conservation equations are essentially those of paragraphs 1.2, 1.3, and 1.4, with modifications whose origins and nature as follows:

- Account is taken of the displacement of the carrier fluid by the dispersed phase, measured by the fractional volume α occupied by the fluid. The necessary modifications to the fluid equations are:
  a) Replacement of the density ρ and effective viscosity μ_{eff} in the transport terms on the left-hand side by the products 'αρ', and 'α μ_{eff}', respectively.
  b) Multiplication of the right-hand terms representing volume-integrated sources and other effects by α.
- Interphase transfer effects are allowed for by including the appropriate source/sink terms, derived from the Lagrangian equations. The Lagrangian equations, when integrated over the control volume, yield the changes in the momentum, mass, and energy of each discrete element between its entry and exit. The sum of these changes for all elements crossing the volume provides, with change of sign, the net momentum, mass, and energy exchanged with the carrier fluid. These are the 'source terms' for the continuous phase equations.

It should be noted that, although a similar analysis could be performed in the case of the conservation equations for the turbulence parameters, there is considerable uncertainty as to how

to account for the direct effects of the discrete phase on the continuous phase turbulence. For the time being, therefore, these effects are ignored.

1.9 Eulerian Multi-Phase Flow (Volume of Fluid Method)

Multiphase flows, where several fluids flow in the domain of interest, play an important role in variety of industrial applications. In general, we associate phases with gases, liquids, or solids and as such some simple examples of multiphase flows are air bubbles rising in a glass of water, sand particles carried by wind, rain drops in air. The definition of phase can be generalized and applied to other fluid characteristics such as size, shape, density, and temperature. Numerical simulations of such flows need to handle additional complexity in comparison to simulating single phase flow due to the presence of interface across which there is a jump in fluid-fluid properties and the exchange of mass, momentum and heat between the phases occurs as well. For modelling considerations, such flows can be classified based on increasing spatial scales of interface between the phases, into dispersed (bubbly flow, droplet flow), mixed / intermittent (slug flow, churn flow) and separated / stratified (film flow, annular flow, horizontal stratified flow).

The volume tracking/interface capturing method of VOF (Volume of Fluid) [44] is adopted for Eulerian in-nozzle flow simulations. Indeed, such model is well suited for simulation of stratified multiphase flows which are characterized by large scale interface. It must be noted that the size of computational cell is critical in classifying the interface as large scale or a small scale. Since the volume tracking / interface capturing methods rely on resolving the interface completely, they are prohibitively expensive for simulating multi-scale flows where modelling of dispersed regime accurately is equally important. In the VOF multiphase model, the distribution of phases and the position of the interface are described by the fields of phase volume fraction α_i. The volume fraction of the phase 'i' is defined as:

$$\alpha_i = \frac{V_i}{V} \tag{37}$$

where V_i is the volume of phase 'i' in the cell, and V is the volume of the cell. The volume fractions of all phases in a cell must sum up to one:

$$\sum_{i=1}^{N} \alpha_i = 1 \tag{38}$$

where N is the total number of phases. Depending on the value of the volume fratcion, the presence of different phases or fluids in a cell can be distinguished as:

- $\alpha_i = 0$: the cell is completely void of phase 'i'
- $\alpha_i = 1$: the cell is completely filled with phase 'i'
- $0 < \alpha_i < 1$: values between the two limits indicate the presence of an interface between phases

The material properties that are calculated in the cells containing the interface depend on the material properties of the constituent fluids. The fluids that are present in the same interface-containing cell are treated as a mixture:

$$\rho = \sum\nolimits_i \rho_i \alpha_i \tag{39}$$

$$\mu = \sum\nolimits_i \mu_i \alpha_i \tag{40}$$

$$c_p = \sum\nolimits_i \frac{(c_p)_i \rho_i}{\rho} \alpha_i \tag{41}$$

where ρ_i is the density, μ_i the dynamic viscosity, and $(c_p)_i$ is the specific heat of phase 'i'. The distribution of phase 'i' is driven by the phase mass conservation equation:

$$\frac{\delta}{\delta t}\int_V \alpha_i dV + \oint_A \alpha_i v \cdot da = \int_V \left(S_{\alpha_i} - \frac{\alpha_i}{\rho_i}\frac{D\rho_i}{Dt}\right) dV - \int_V \frac{1}{\rho_i} \nabla \cdot \left(\alpha_i \rho_i v_{d,i}\right) dV \tag{42}$$

where a is the surface area vector, v is the mixture mass-averaged velocity, $v_{d,i}$ is the diffusion velocity, S_{α_i} is a user-defined source term of phase 'i', and $\frac{D\rho_i}{Dt}$ is the material or Lagrangian derivative of the phase densities ρ_i. The volume fractions are calculated as follows:

- When there are two VOF phases present, the volume fraction transport is solved for the first phase only. In each cell, the volume fraction of the second phase is adjusted so that the sum of the volume fractions of the two phases is equal to 1.
- When there are three or more VOF phases present, the volume fraction transport is solved for all phases. The volume fraction of each phase is then normalized based on the sum of the volume fractions of all phases in each cell.

The total mass conservation equation for all phases is given by:

$$\frac{\delta}{\delta t}\int_V \rho dV + \oint_A \rho v \cdot da = \int_V S dV \tag{43}$$

where S is a mass source term that is related to the phase source term as follows:

$$S = \sum_i S_{\alpha_i}\rho_i \tag{44}$$

The dependency on the volume fractions of the constituent phases of the fluid mixture is accounted for through the density, which is given by Eqn. (37). The momentum equation is:

$$\frac{\delta}{\delta t}\int_V \rho v dV + \oint_A \rho v \otimes v \cdot da$$

$$= -\oint_A pI \cdot da + \oint_A T \cdot da + \int_V \rho g dV + \int_V f_b dV \tag{45}$$

$$-\sum_i \int_A \alpha_i \rho_i v_{d,i} \otimes v_{d,i} \cdot da$$

where p is the pressure, I is the unity tensor, T is the stress tensor, and f_b is the vector of body forces. Finally, the energy equation can be written as:

$$\frac{\delta}{\delta t}\int_V \rho E dV + \oint_A \left[\rho H v + p + \sum_i \alpha_i \rho_i H_i v_{d,i}\right] \cdot da = -\oint_A \dot{q''} \cdot da + \oint_A T \cdot v da + \int_V f_b \cdot v dV + \int_V S_E dV \quad (46)$$

where E is the total energy, H is the total enthalpy, $\dot{q''}$ is the heat flux vector, and S_E is a user-defined energy source term. The terms that contain the diffusion velocity $v_{d,i}$ in all the previous equations, are due to the slip between phases.

2. Tested Injectors and Operating Conditions

In this chapter of the thesis, all the simulated injectors are introduced more in detail, including the main characteristics of the geometry, the operating conditions, and the available experimental data.

2.1 Spray G (Gasoline research injector)

The Spray G injector is analysed in this work with the purpose to understand the effect of initial droplet diameters on the spray development inside the combustion chamber. As it is shown in Figure 2, the Spray G is characterized by an 8-holes configuration. Main geometric parameters such at the plume cone angle and the drill angle are depicted in Figure 3.

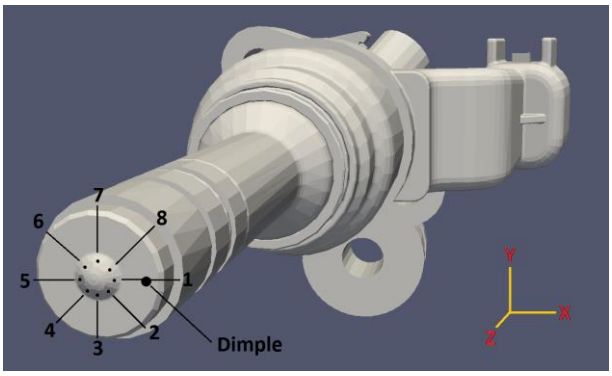

Figure 2. Spray G Injector Geometry

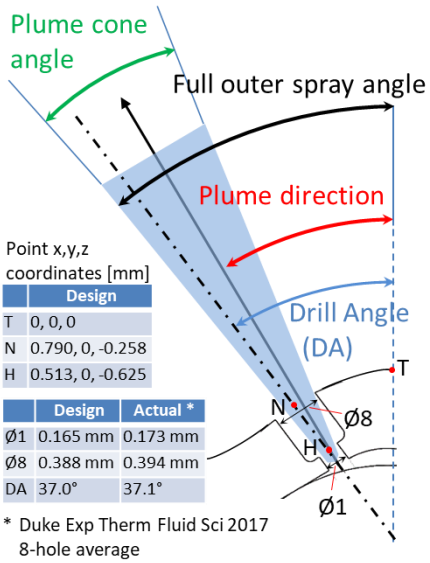

Figure 3. Spray G Main geometric specifications

Data from pattern study analysis [45] and x-ray radiography measurements performed at 2 mm far from the injector tip [46] proved a deflection of the spray plumes towards the injector axis, leading to a definition of the plume direction angle between $33 \div 34°$, compared to the $37°$ of the nominal drill angle. A single operative condition is considered for the Spray G, whose main characteristics are reported in Table 1. This is the most investigated operation in the ECN community, and various experimental data are available, provided by different institutions [47,49].

Fuel	Fuel Pressure	Fuel Temperature	Ambient Temperature	Ambient Pressure	Ambient Density
Iso-Octane (C_8H_{18})	20 MPa (a)	363 K	573 K	0.6 MPa (a)	3.5 kg/m^3

Table1. Spray G Operating Condition

The first available data consists in the measured mass flow rate with an injection pressure of 20 MPa, and an injection duration about $700 \cdot 10^{-6} s$:

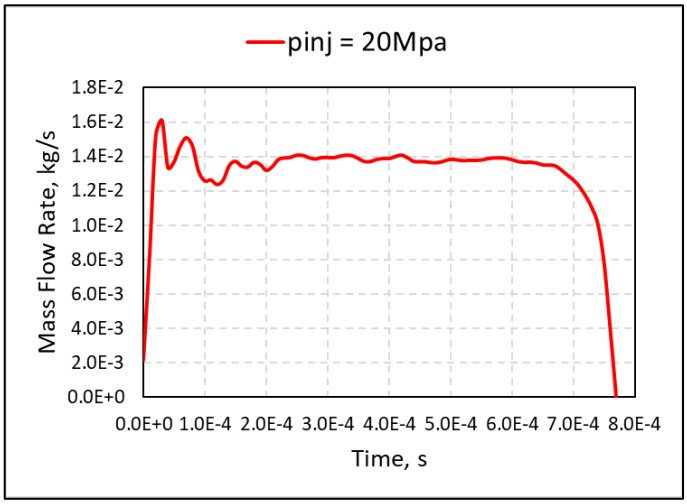

Figure 4. Mass Flow Rate for the Spray G injector

Nozzle hydraulic coefficients are obtained from mass flux and momentum flux measurements carried out at Càtedra de Motores Térmicos (CMT) in Valencia [50]. In particular, values for the discharge coefficient C_d, area coefficient C_a, and velocity coefficient C_v are provided on the ECN website [51] and reported in the following table:

C_d	0.5
C_a	0.73
C_v	0.69

Table 2. Spray G hydraulic coefficients

Definitions for the hydraulic coefficients are reported hereafter:

$$C_a = \frac{A_{eff}}{A}; \quad C_v = \frac{v}{v_{th}}; \quad C_d = \frac{\dot{m}_{r,i}}{A\, v_{th}\, \rho_l} = C_a \cdot C_v \tag{47}$$

where A and A_{eff} are the geometric and effective nozzle area, respectively, v_{th} and v are the theoretical and effective injection velocity, respectively, and $\dot{m}_{r,i}$ is the measured rate of injection. The global spray evolution is analysed through the Diffused-Back-Illumination (DBI) imaging. DBI uses the extinction produced by the spray droplets to provide a measure related to the liquid volume fraction along the path of the light. The advantage for quantification is that there is self-calibration for the initial intensity. In engine (high-pressure, high-temperature) environments, care must be taken to ensure that the diagnostics is not sensitive to vapor-phase beam steering from temperature/refractive index gradients. The diffuser angle and collection angle need to be quantified for a given setup, and the camera needs to be configured to accurately measure background intensity (with no transmitted DBI light). An example setup is shown in Figure 5. An image of the spray obtained with DBI technique at $500 \cdot 10^{-6} s$ after the start of injection is depicted in Figure 6. Liquid penetration curve extrapolated by imaging data is reported in Figure 7. Finally, PDA measurements are available at different locations on a plane 15 mm far from the injector tip, as depicted in Figure 8. As it possible to notice, for the sake of validity of the experimental data, only three locations are considered for the further comparison with numerical

outcomes. PDA data, considered for the validation of numerical results, are supplied in terms of Sauter mean diameter D32.

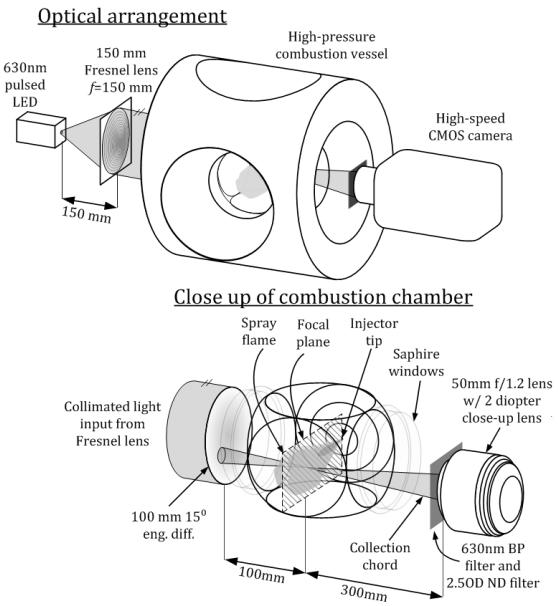

Figure 5. Diffused back-illumination for high-speed extinction imaging

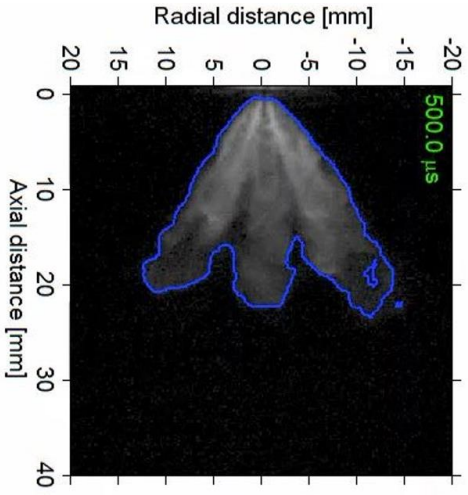

Figure 6. Spray Imaging obtained by DBI analysis

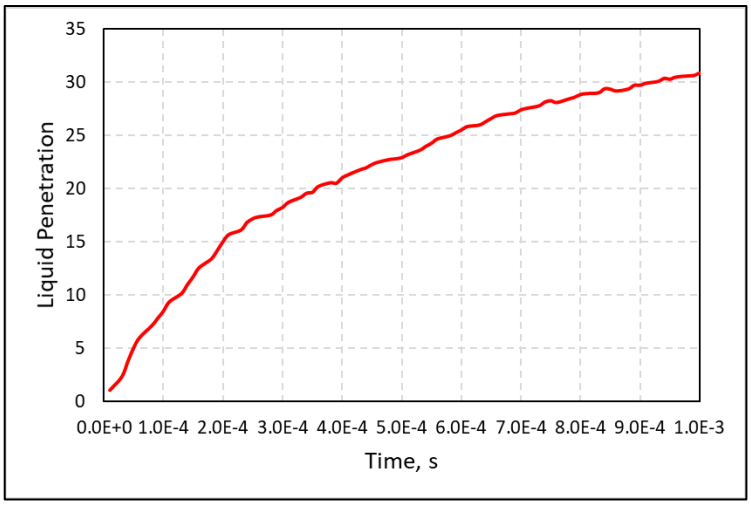

Figure 7. Spray G experimental liquid penetration curve

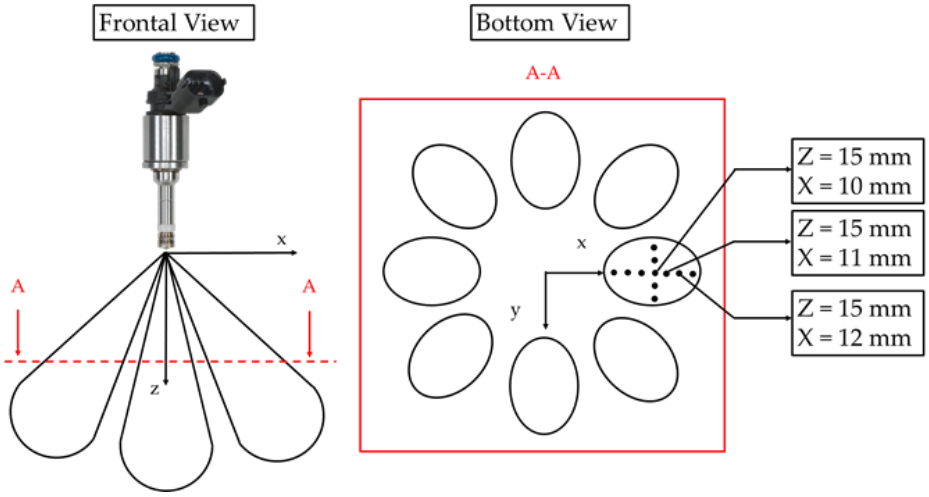

Figure 8. Spray G PDA measurement points

2.2 INJ1 (single-hole gasoline research injector)

The INJ1 is a single-hole research injector provided by the SprayLAB - University of Perugia, and it is employed in this work to calibrate the gasoline model constants for the GruMo secondary break-up model. The injector nozzle is characterized by a geometric hole diameter equal to $200 \cdot 10^{-6}\, m$, and a length-to-diameter ratio L/D equal to 1. The operating conditions for the INJ1 injector are listed in Table 3.

Fuel	Fuel Pressure	Fuel Temperature	Ambient Temperature	Ambient Pressure	Ambient Density
n-Heptane (C7H16)	10 MPa (a)	298 K	298 K	0.04; 0.1; 0.3 MPa (a)	0.47; 1.18; 3.55 kg/m^3

Table 3. INJ1 Operating Condition

The hydraulic characterization is carried out by a Zeuch-type injector analyser to provide the instantaneous mass flow rate curve, reported in Figure 9. The mass flow rate curve refers to a pressure difference between rail and ambient of 10 MPa, the excitation time is equal to $1.5 \cdot 10^{-3}\, s$, and the injected mass is about $3.9 \cdot 10^{-6}\, kg$.

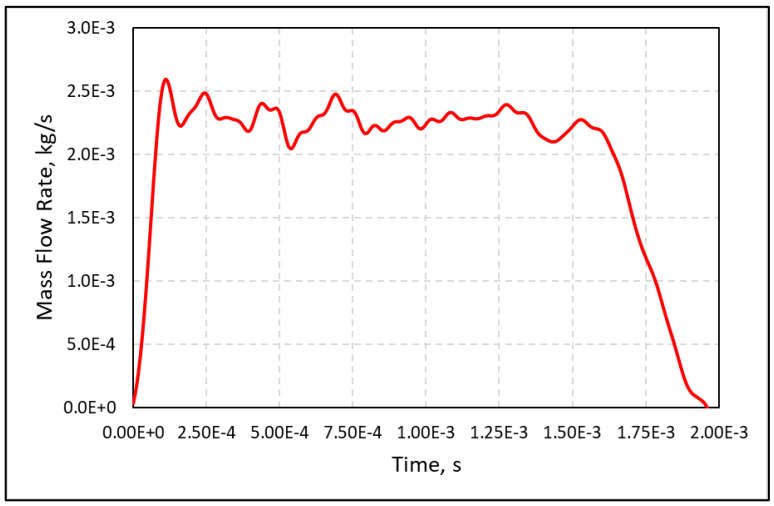

Figure 9. INJ1 Mass Flow Rate curve

Spray momentum flux measurement is available by means of a sensor positioned 5 mm far from the injector tip, which measure the instantaneous impact force [52,53]. The latter is reported in Figure 10. Momentum flux measurement is carried out with an ambient pressure equal to 0.1 MPa.

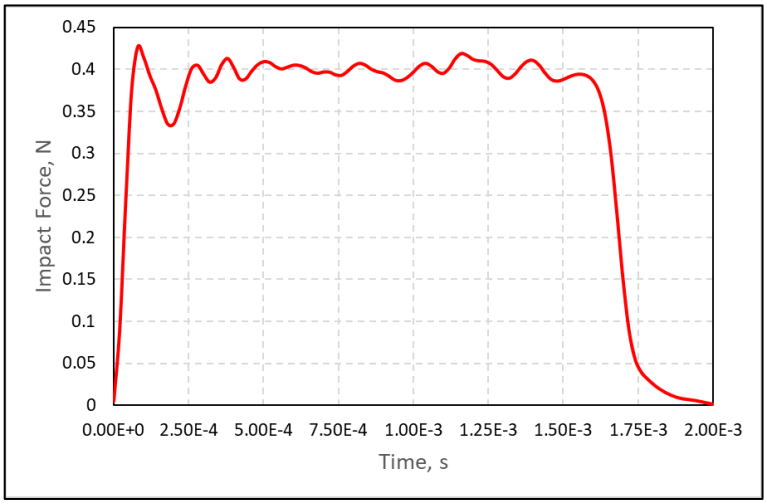

Figure 10. INJ1 momentum flux curve

Experimental liquid penetration curves for all the considered ambient pressures are reported in Figure 11.

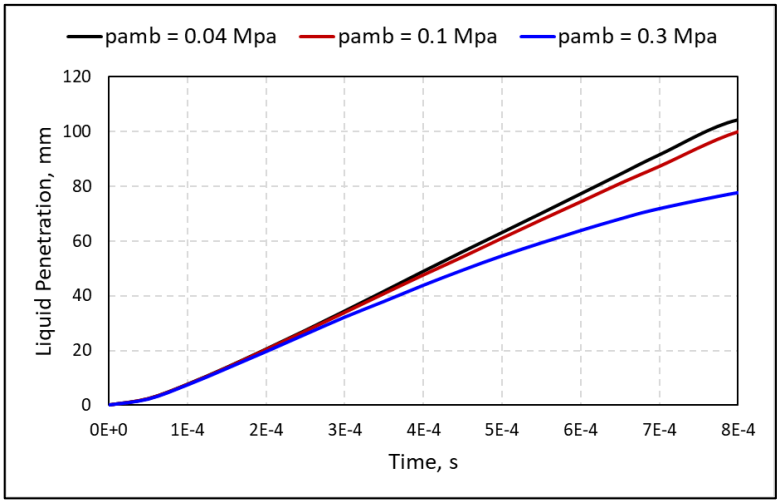

Figure 11. INJ1 experimental liquid penetration curves

Droplet size and velocity are investigated by PDA technique at different locations, as shown in Figure 12.

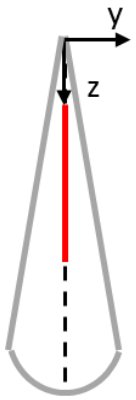

X [mm]	Y [mm]	Z [mm]
0	0	15
0	0	20
0	0	25
0	0	30
0	0	40
0	0	50
0	0	60

Figure 12. INJ1 PDA measurement points positions.

PDA data are supplied in terms of arithmetic mean diameter (D10), Sauter mean diameter (D32), and z-component of the velocity. For all the tested conditions, PDA experimental outcomes represent an average over 300 shots, and for each individual shot, data considered for the average pertain to a time window of $1 \cdot 10^{-3}\ s$ since the energizing time start, with the aim to focus on the static stage of the injection, excluding the very slow (or still) drops of the spray tail from the analysis.

2.3 INJ2 (single-hole gasoline research injector)

The INJ2 is a single-hole research injector provided by the SprayLAB-University of Perugia, and it is employed in this work to validate the gasoline model constants for the GruMo secondary break-up model, and to test the new flash-boiling model implemented in the commercial code STAR-CD by Siemens. The injector nozzle is characterized by a step-hole geometry, with a nominal orifice diameter equal to $175 \cdot 10^{-6} m$, and a length-to-diameter ratio L/D equal to 1. The operating conditions for the INJ2 injector are listed in Table 4. The experimental mass flow rate

profile reported in Figure 13 is considered for both analysed conditions. The curve evaluation is carried out with an excitation time of $1.5 \cdot 10^{-3}\ s$, and the injected mass is about $2.7 \cdot 10^{-6}\ kg$.

Fuel	Fuel Pressure	Fuel Temperature	Ambient Temperature	Ambient Pressure	Ambient Density
n-Heptane (C7H16)	10 MPa (a)	298 ;393 K	298 K	0.04 MPa (a)	0.47 kg/m^3

Table 4. INJ2 Operating Condition

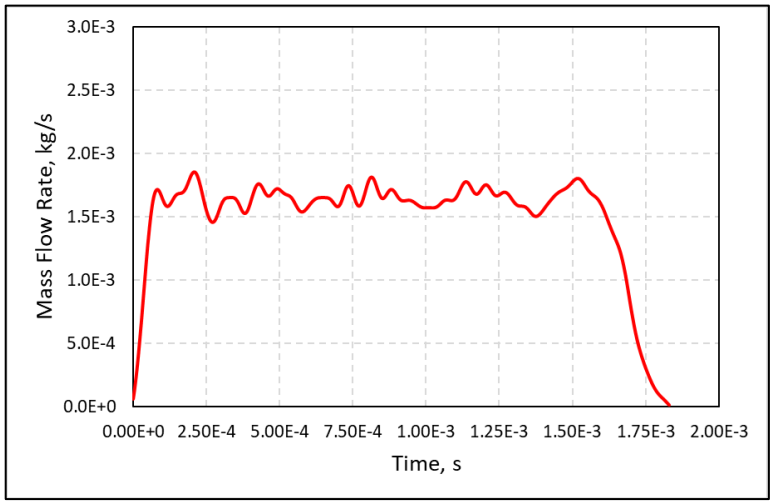

Figure 13. INJ2 Mass Flow Rate curve

Spray momentum flux, reported in Figure 14, is evaluated through experiments with the same methodology described for the INJ1 in the previous paragraph. For this injector, experimental impact force is measured with an excitation time equal to $1 \cdot 10^{-3}\ s$. Experimental liquid penetration curve extrapolated from the imaging analysis is depicted in Figure 15. Droplet size and velocity are investigated by PDA technique at different locations, as shown in Figure 16. PDA data are supplied in terms of arithmetic mean diameter (D10), Sauter mean diameter (D32), and z-

component of the velocity. PDA experimental outcomes represent an average over 300 shots, and for each individual shot, data considered for the average pertain to a time window of $2 \cdot 10^{-3}\ s$ since the energizing time start, in order to exclude the spray tails from the analysis.

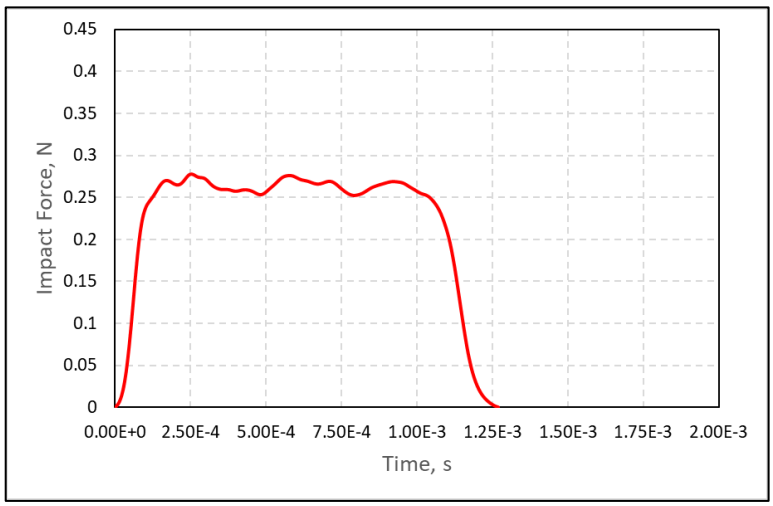

Figure 14. INJ2 momentum flux curve

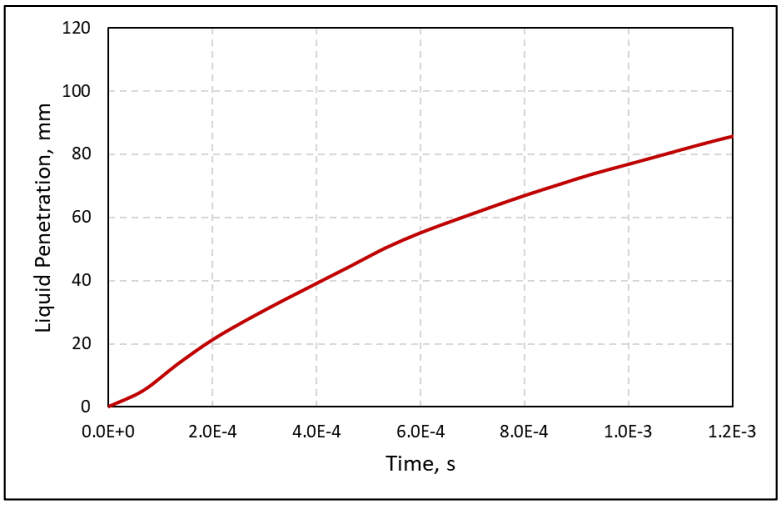

Figure 15. INJ2 experimental liquid penetration curve

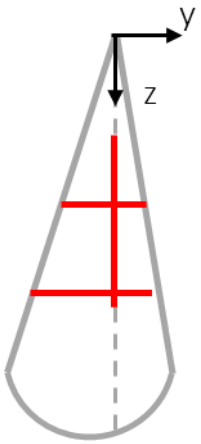

X [mm]	Y [mm]	Z[mm]
$-8 \leq X \leq 1$	0	30
$-12 \leq X \leq 2$	0	50
-3	0	$20 \leq X \leq 50$

Figure 16. INJ2 PDA measurement points positions. Stepping is 1 mm for X scan, 10 mm for Z scan

2.4 INJ3 (5-hole gasoline prototype injector)

The INJ3 is a 5-hole injector provided by the SprayLAB-University of Perugia, and it is employed in this work to understand the effect of both initial droplet diameters and injection pressure on the spray development inside the combustion chamber, and to validate the gasoline model constants for the GruMo secondary break-up model. It is a side-mounted, counter bore, GDI prototype, whose hole diameters are equal to $125 \cdot 10^{-6} m$. The injector is experimentally investigated in a wide range of injection pressures, from 5 up to 60 MPa; only three pressure levels (20,40, and 60 MPa) are considered for the study on the primary break-up, while an injection pressure of 10 MPa is adopted for the secondary break-up simulations. Operating conditions selected for further numerical investigations are reported in Table 5.

Fuel	**Fuel Pressure**	**Fuel Temperature**	**Ambient Temperature**	**Ambient Pressure**	**Ambient Density**
n-Heptane (C7H16)	10; 20; 40; 60 MPa (a)	298 K	298 K	0.1 MPa (a)	1.18 kg/m^3

Table 5. INJ3 Operating Condition

In order to obtain statistically significant results, injection rate profiles of 300 consecutive shots are measured: the mean mass flow rate profiles, for an energizing time of $1.5 \cdot 10^{-3}\ s$, and for the

examined pressures, are reported in Figure 17. Global evolution of the spray plumes is investigated by means of high-speed imaging, and the resulting average tip penetration curves for the most advanced plume are illustrated in Figure 18. Spray momentum flux curve, evaluated by a sensor positioned 5 mm far from the injector tip, is reported in Figure 19. Droplet sizing and velocities are investigated with a PDA analysis in different locations as illustrated in Figure 20. Experimental outcomes in the measurement stations are supplied in terms of arithmetic mean diameter (D10), Sauter mean diameter (D32), and z-component of the velocity.

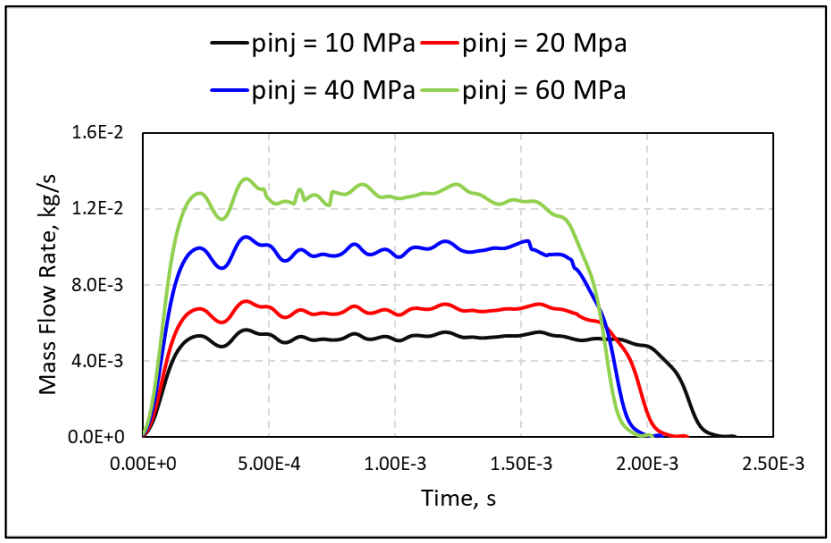

Figure 17. INJ3 Mass Flow Rate curves

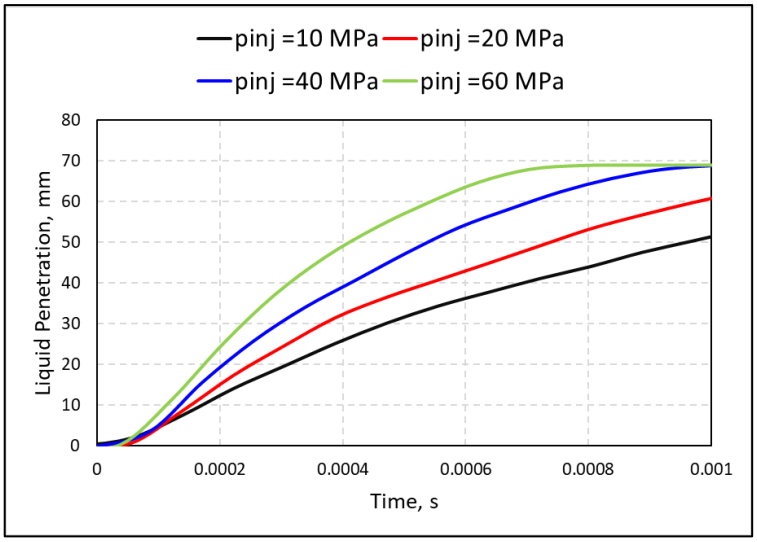

Figure 18. INJ3 experimental liquid penetration curves

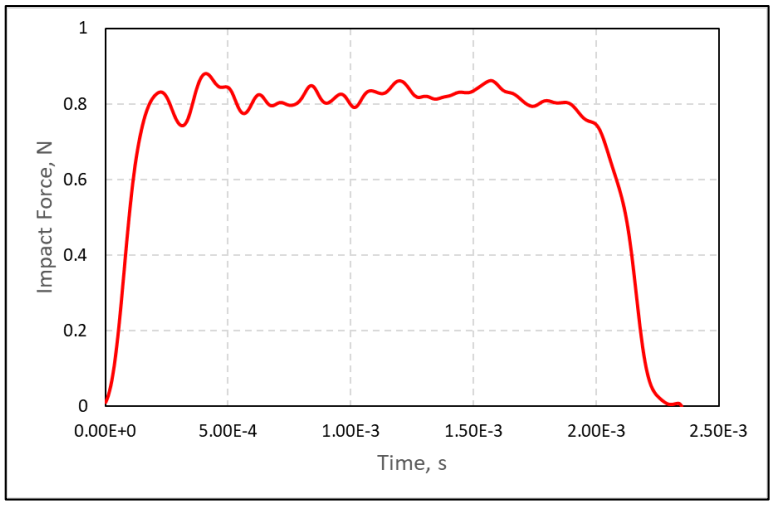

Figure 19. INJ3 momentum flux curve

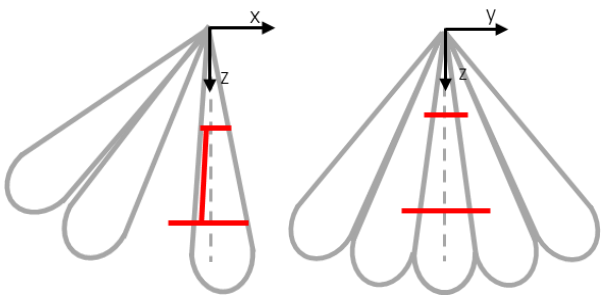

X [mm]	Y [mm]	Z[mm]
$-1.5 \leq X \leq 3.5$	0	20
$-6.5 \leq X \leq 6.5$	0	50
-0.6	$-2 \leq Y \leq 3$	20
-1.5	$-8 \leq Y \leq 6$	50
$-1.5 \leq X \leq -0.6$	-1	$20 \leq Z \leq 50$

Figure 20. INJ2 PDA measurement points positions. Stepping is 1 mm for X- and Y- scan, 10 mm for Z scan

2.5 Spray A, SprayC and Spray D (single-hole diesel research injectors)

In the present work, three single-hole injectors, provided by ECN, are analysed to elaborate the new GruMo secondary break-up model, suitable for diesel applications. All the nozzles are simulated at the same operating standard condition, characterized by ambient pressure, temperature, and density equal to 6 MPa (a), 900 K, and 22.8 kg/m^3 respectively. The adopted fuel is n-Dodecane, the injection pressure and temperature are equal to 150 MPa and 363 K, respectively. Spray A is further analysed in two different operative conditions (ambient density equal to 7.6 and 15.2 kg/m^3) in order to obtain the GruMo model parameters correlation against the ambient density. Nozzle diameters and hydraulic coefficients for the injectors, provided by the ECN community [51] are reported in Table 6. The Spray C nozzle is manufactured to intentionally produce cavitation within the hole, thus reducing the area coefficient C_a. On the other hand, Spray D nozzle is designed to minimize cavitation and, thus, the difference between the orifice diameter and the effective one.

Spray	**A**	**C**	**D**
Geometrical Diameter [µm]	84	200	186
Discharge Coefficient *Cd*	0.89	0.72	0.92
Area Coefficient *Ca*	0.98	0.87	0.93
Velocity Coefficient *Cv*	0.91	0.82	0.99
Effective Diameter [µm]	83	186	179

Table 6. Nozzle parameters for Spray A, Spray C, and Spray D

Mass flow rate curves for the three injectors are depicted in Figure 21. It is possible to notice that the static liquid length value for the Spray D is greater than the Spray C one, due to the different shape of the nozzle hole. As for the standard condition, both liquid and vapor penetration curve are provided for Spray A, Spray C, and Spray D, depicted in Figure 22 and Figure 23, respectively. As for the analysis of the ambient density effect on the secondary break-up, carried out for the Spray A, only liquid length curves are available and reported in Figure 24.

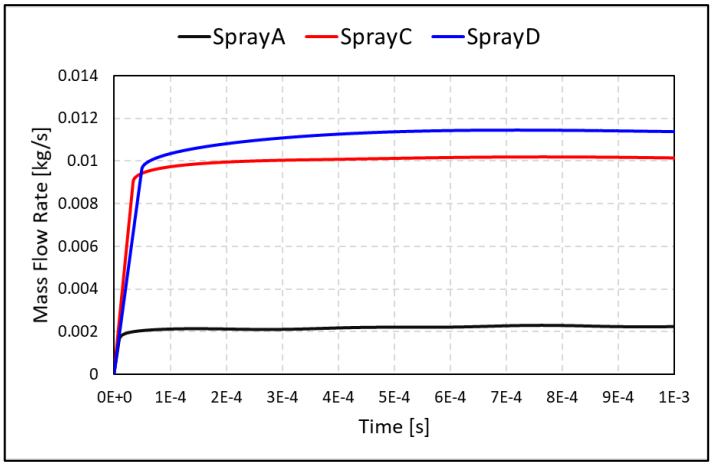

Figure 21. Diesel injectors Mass Flow Rate curves

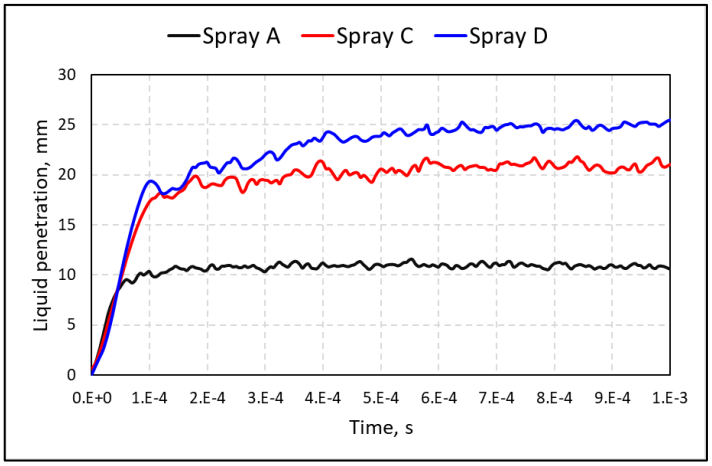

Figure 22. Liquid penetration curve for the Spray A, C, and D at the standard condition

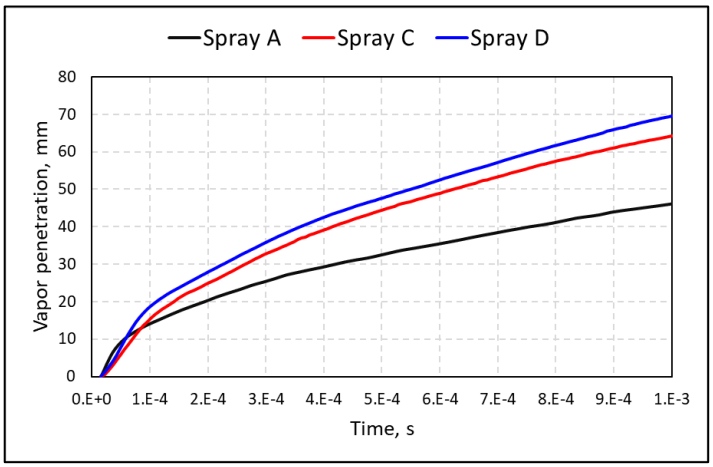

Figure 23. Vapor penetration curve for the Spray A, C, and D at the standard condition

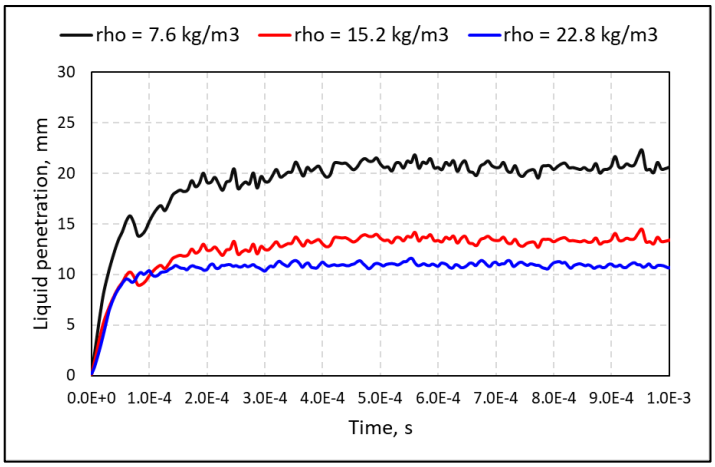

Figure 24. Liquid penetration curve for the Spray A injection with different ambient densities

3. Models Methodology

In this chapter, the different methodologies adopted for 3D-CFD spray simulations are introduced. At first, an overview on different approaches for droplet initialization is carried out. Then secondary break-up models of Reitz and KHRT are summarized, and the new GruMo model is supplied. At last, the novel flash-boiling model implementation is reported in detail.

3.1 Methodologies for droplet initialization

Lagrangian spray simulations requires the existence of drops inside the numerical domain, for this reason the liquid fuel column exiting the nozzle hole is replaced by the injection of computational droplets. The task of primary break-up models is to determine the initial conditions of these droplets, such as diameter and velocity components. There are only very few detailed models for the simulation of primary break-up of high-pressure sprays; the main reason is that the experimental investigation is extremely complicated because of the dense spray and the small dimensions. Thus, it is difficult to understand the relevant processes and to verify primary break-up models. Different classes of break up models exist concerning the way the significant mechanisms like aerodynamic induced, turbulence induced, and cavitation induced break up are treated. The simpler the model is, the less the input data are required. However, if the nozzle flow is poorly linked to the actual upstream conditions, a huge number of assumptions has to be made. This results in a significant loss of quality concerning the prediction of structure and starting conditions of the first spray near the nozzle; nevertheless, an advantage of simpler models is that their area of application is wider because of their global validity. Furthermore, detailed models often require a complete CFD simulation of the injector flow as input data, with a consequent increase of computational time. However, the close linking of injector flow and spray guarantees the most accurate simulation of both primary break-up process and mixture formation. It must be pointed out that all kind of models have their special field of application; depending on the available input data, the computational time, and the relevant break-up process of the specific configuration as well as the required accuracy of the simulation, the appropriate model has to be chosen.

3.1.1 Blob Model

The simplest and most popular way of defining the starting conditions of the first droplets at the nozzle hole exit of full-cone sprays is the so-called blob method [54], developed by Reitz. This approach assumes that atomization and drop break-up within the dense spray near the nozzle are indistinguishable processes and that a detailed simulation can be replaced by the injection of big spherical droplets with uniform size, which are then subject to secondary aerodynamic induced break-up. The diameter of these blobs equals the nozzle hole diameter and the number of drops injected per unit time is determined from the mass flow rate. Although blobs break-up due to their interaction with the gas, there is a region of large discrete liquid particles near the nozzle, which is conceptually equivalent to a dense core. A schematic representation of the blob-method is illustrated in Figure 25.

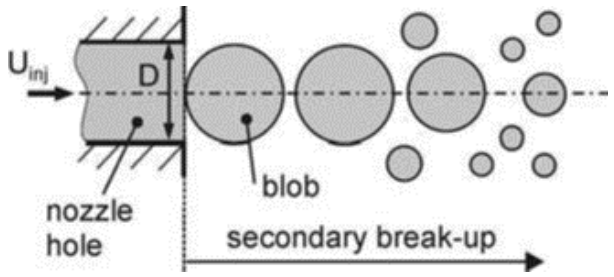

Figure 25. Blob-method by Reitz

Assuming slug flow inside the nozzle, the conservation of mass gives the injection velocity $U_{inj}(t)$ of the blobs as:

$$U_{inj}(t) = \frac{\dot{m}_{inj}(t)}{A_{hole}\,\rho_L} \tag{48}$$

where A_{hole} is the cross-sectional area of the nozzle hole, ρ_L is the fuel density, and $\dot{m}_{inj}(t)$ is the measured fuel mass flow rate. In order to define the velocity components of each blob, the spray cone angle ϕ must be known from measurements or has to be estimated using semi-empirical relations (e.g. Hiroyasu and Arai [55]).

3.1.2 Distribution Functions

This method assumes that the fuel is already fully atomized at the nozzle exit and that the distribution of drop sizes can be described by mathematical functions. In this case, a distribution of droplet sizes is injected. In high pressure sprays, neither the droplet sizes nor their distribution in the dense spray near the nozzle could be quantified experimentally up to now; thus the droplet size distribution must be guessed and iteratively adjusted until the measured drop sizes in the far field of the nozzle are similar to the simulated ones. This of course does not represent a detailed modeling of the relevant processes during primary break-up but can be used as an alternative to the mono-disperse injection of the blob-method in case no suitable atomization models can be used. The most used mathematical distribution is the Rosin-Rammler one, in which the initial droplet diameter D_d is evaluated as:

$$D_d = \overline{D}\,(-\ln\,(1-Y))^{\frac{1}{n}} \tag{49}$$

where $\overline{D}$ is the Rosin-Rammler diameter, Y is the mass fraction of the droplets with diameter less than D_d, and n is the distribution exponent. The mean diameter $\overline{D}$ can be chosen iteratively, or it can be inherited by PDA data as described before.

3.1.3 Inner-Nozzle Flow Simulations

Inner-nozzle flow simulations represent a crucial aspect of spray modeling, since they are able to provide essential information for the droplet initialization, such as diameter and velocity of the liquid column. A main goal in this PhD activity was to formulate a simplified and robust approach that considers the cavitation inside the nozzle, with a reduced computational time. A detailed review of the numerical models adopted in such approach is provided in Chapter 4. Simulations are carried out in the commercial software STAR-CCM+ licensed by Siemens. Different quantities are evaluated, and their definitions are reported in Table 7. A schematic representation of the evaluation of plume directions in the global reference system is depicted in Figure 26.

$SAVG_{x-velo}$	Surface average report at the nozzle exit for the X-velocity component in the global reference system.
$SAVG_{y-velo}$	Surface average report at the nozzle exit for the Y-velocity component in the global reference system.
$SAVG_{z-velo}$	Surface average report at the nozzle exit for the Z-velocity component in the global reference system.
α_x	$\text{atan}\left(\frac{SAVG_{y-velo}}{SAVG_{z-velo}}\right)$
α_y	$\text{atan}\left(\frac{SAVG_{x-velo}}{SAVG_{z-velo}}\right)$
$C_a\ (area\ coefficient)$	Surface average report at the nozzle exit of the liquid fuel volume fraction.
MFR	Mass flow report at the nozzle exit.

Table 7. Evaluated quantities in Eulerian in-nozzle flow simulations

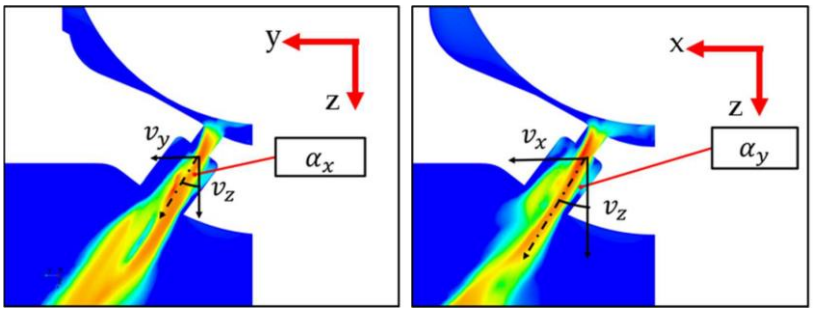

Figure 26. Angles providing plume directions in Eulerian in-nozzle flow simulations

The effective diameter used to initialize the droplets in Lagrangian simulations can be estimated as:

$$D_{eff} = D_{geom}\sqrt{C_a} \tag{50}$$

Such quantity can be used in the blob-method, replacing the nozzle-hole geometrical diameter. The effective injection velocity is evaluated by means of the discharge coefficient C_d, and velocity coefficient C_v:

$$C_d = \frac{MFR}{\dot{m}_{f,th}}; \qquad C_v = \frac{C_d}{C_a} \;\Rightarrow\; U_{inj,eff} = U_{th} \cdot C_v \tag{51}$$

where U_{th} is the theoretical velocity derived by the Bernoulli's principle.

3.1.4 Experimental Momentum Measurements

Momentum measurements can be proficiently employed to evaluate the droplet initial conditions for numerical simulations relying on a blob model. An approach was developed at the SprayLAB of the University of Perugia [28],[56], and it is briefly resumed in the following. The experimental measured total steady-state momentum flux $\dot{M}$ is given by the sum of the momentum fluxes of each single hole $\dot{M}_\iota$, and it corresponds to the steady-state impact force F of the whole spray on a target surface, positioned at a given distance from the injector tip. A simplified definition, adopted in this work, to express the momentum flux is:

$$\dot{M} = F = \dot{m}_{eff}\, v_{eff} \tag{52}$$

where $\dot{m}_{eff}$ is the effective mass flow rate, and v_{eff} is the effective injection velocity. Effective mass flow rate can be exploited as:

$$\dot{m}_{eff} = \rho\, A_{eff}\, v_{eff} \tag{53}$$

and consequently the momentum flux can be rewritten as:

$$\dot{M} = \dot{m}_{eff} \frac{\dot{m}_{eff}}{\rho\, A_{eff}} = \frac{\dot{m}_{eff}^2}{\rho\, C_a\, A_0} \tag{54}$$

where C_a is the area coefficient, and A_0 is the geometrical area of the nozzle. In this case, both A_0 and A_{eff} refer to the whole injector, i.e. they are the sums of the geometrical and effective areas of the nozzle holes, respectively. Since $\dot{m}_{eff}$ and $\dot{M}$ are provided by the experimental hydraulic

characterization and the momentum flux measure, respectively, the area coefficient C_a can be obtained as:

$$C_a = \frac{\dot{m}_{eff}^2}{\rho \, \dot{M} \, A_0} \cong C_{a,i} \tag{55}$$

In case of multi-hole injectors, the area coefficient of each single hole $C_{a,i}$ is approximated with C_a which represents, instead, the coefficient of the whole spray. Thanks to the contraction coefficient and the experimental momentum flux referred to the single hole, the effective mass flow rate $\dot{m}_{eff,i}$ and diameter $D_{eff,i}$ for each single hole can be obtained as:

$$\dot{m}_{eff,i} = \sqrt{\rho \, C_{a,i} \, A_{0,i} \, \dot{M}_i} \tag{56}$$

$$D_{eff,i} = \sqrt{\frac{4 \, C_{a,i} \, A_{0,i}}{\pi}} \tag{57}$$

Then, from the experimental mass flow rate, it is possible to calculate the discharge coefficient $C_{d,i}$ as:

$$C_{d,i} = \frac{\dot{m}_{eff}}{\dot{m}_{th,i}} = \frac{\dot{m}_{eff}}{A_{0,i}\rho v_{th}} = \frac{\dot{m}_{eff}}{A_{0,i}\rho\sqrt{\frac{2\left(p_{inj} - p_{amb}\right)}{\rho}}} \tag{58}$$

where p_{inj} and p_{amb} are the injection and the ambient pressure, respectively. The effective injection velocity can be evaluated as in equation (51).

3.2 Secondary break-up models

As stated earlier, Secondary break-up is the disruption of liquid droplets into smaller ones caused by aerodynamic forces due to the relative velocity between the droplets and the surrounding gas. The surface tension force opposes to the deformation and, thus, to the break-up, trying to keep the droplets spherical. The surface tension increases with the local curvature, thus the smaller the droplet diameter is, the higher the value of the critical relative velocity required to generate droplet instability and, thus, break-up becomes. Such competition is formalized by the dimensionless gas phase Weber number in equation (2), which represent the ratio between aerodynamic force and surface tension. From experimental investigations, is known that, based on the Gas Weber number, different droplet break-up mechanisms exist [59], as depicted in Figure 27.

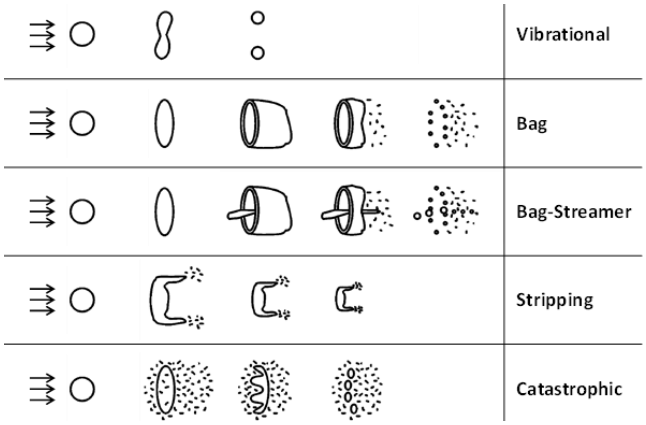

Figure 27. Droplet secondary break-up regimes

Following the criteria proposed by Pilch and Erdman [60], at We_g≤6 only Vibrational mode occurs. Oscillations develop at the natural frequency of the drop, and, under certain conditions, they can increase up to the droplet decomposition into a few large fragments. Vibrational breakup does not necessarily occur in every instance and the overall breakup time is long compared to the other breakup mechanisms. Consequently, it is not usually considered. For 6< We_g≤25, a bag-like deformation characterises the droplet break-up. Further increasing the Weber number (i.e. at 25< We_g≤50), an additional jet appears leading to the so-called Bag-Streamer (or Bag-and-Stamen or Bag-Jet) regime. Then, for 50<Weg≤175, the Stripping mechanism is the main promoter, characterized by very small child droplets which are continuously ripped off the parent one due to

shear forces. Finally, at We_g>175, Catastrophic break-up dominates, and it shows two different stages. On the one hand, the strong deceleration causes oscillations with large amplitude and wavelength, producing few large droplets. On the other hand, surface waves with short wavelengths are stripped off forming small child droplets. At engine-like conditions all the described break-up mechanisms can occur. However, the disintegration process mainly takes place near the nozzle where the Weber number is remarkably high. Moving downstream from the nozzle, Weber numbers significantly reduce because droplet diameters and velocities decrease. Existing and most diffused secondary break-up models for gasoline and Diesel sprays, namely the Reitz-Diwakar and the KHRT, do not account for all the mechanisms of Figure 27. As for the former, only Bag and Stripping are accounted for. As for the latter, it combines two sub models, based on Kelvin-Helmholtz and Rayleigh-Taylor theories, respectively. Kelvin-Helmholtz sub model considers instabilities due to the slip velocity of the droplet, similarly, to Stripping regime. Conversely, Rayleigh-Taylor instabilities are due to the droplet deceleration, as in the catastrophic regime. For both the Reitz-Diwakar and KHRT models, each break-up regime is characterized by two constants: the first prescribing the onset of the specific mechanism, the second specifying the timescale.

3.2.1 Reitz Diwakar Model

The Reitz-Diwakar model [18], [54] assumes that droplet break-up due to aerodynamic forces occurs in one of the following modes:

- 'Bag break-up', in which the non-uniform pressure field around the droplet causes it to expand in the low-pressure wake region and eventually disintegrate when surface tension forces are overcome.
- 'Stripping break-up', a process in which liquid is sheared or stripped from the droplet surface.

In each case, theoretical studies have provided a criterion for the onset of break-up and concurrently an estimate of the stable droplet diameter,$D_{d,stable}$, and the characteristic time scale τ_b of the break-up process. This allows the break-up rate to be calculated from:

$$\frac{d\,D_d}{dt} = \frac{\left(D_d - D_{d,stable}\right)}{\tau_b} \tag{59}$$

where D_d is the instantaneous droplet diameter.

As for the bag break-up, instability is determined by a critical value of the Weber number We:

$$We = \frac{\rho\,|u - u_d|^2\,D_d}{2\,\sigma_d} \geq C_{b1} \tag{60}$$

where σ_d is the surface tension coefficient, and C_{b1} is an empirical coefficient [18]. The stable droplet size is that which satisfies the equality in the above equation. The associated characteristic time is:

$$\tau_b = \frac{C_{b2}\,\rho_d^{1/2}\,D_d^{3/2}}{4\,\sigma_d^{1/2}} \tag{61}$$

in which $C_{b2} = \pi$. As for the stripping break-up, the criterion for the onset regime is:

$$\frac{We}{\sqrt{Re_d}} \geq C_{s1} \tag{62}$$

where C_{s1} is a coefficient equal to 0.5 [18] and Re_d is the droplet Reynolds number defined as:

$$Re_d = \frac{\rho_{gas}\,|u - u_d|\,D_d}{\mu_{gas}} \tag{63}$$

where ρ_{gas} and μ_{gas} are density and molecular viscosity of the gas, respectively. The characteristic time scale for this regime is:

$$\tau_s = \frac{C_{s2}}{2}\left(\frac{\rho_d}{\rho_{gas}}\right)^{1/2}\frac{D_d}{|u - u_d|} \tag{64}$$

where C_{s2} is an empirical coefficient [18].

3.2.2 KHRT Model

The KHRT droplet break-up model [19] consists of a composite process in which Kelvin-Helmholtz (KH) aerodynamic instabilities growing on a droplet surface are simultaneously calculated with Rayleigh-Taylor (RT) instabilities resulting from the deceleration of the injected droplets. The two physical models compete with each other and the one predicting the fastest onset of an instability gives rise to a break-up event. In a break-up triggered by the KH process, small droplets are shed by the parent computational parcel to form a new parcel. In an RT break-up, all droplets break up completely into new droplets of different sizes. Their number is then adjusted to conserve mass while at the same time ensuring that the original number of parcels remains the same. The overall process is illustrated schematically in Figure 28. In the KH model, a parent droplet with radius larger than the wavelength Λ_{KH} of the growing unstable surface wave will break into a new parent and child droplet pair. The size (diameter) of the stable child droplet is:

$$D_s = 2B_0\Lambda_{KH} \tag{65}$$

where B_0 is a model constant with default value 0.61.

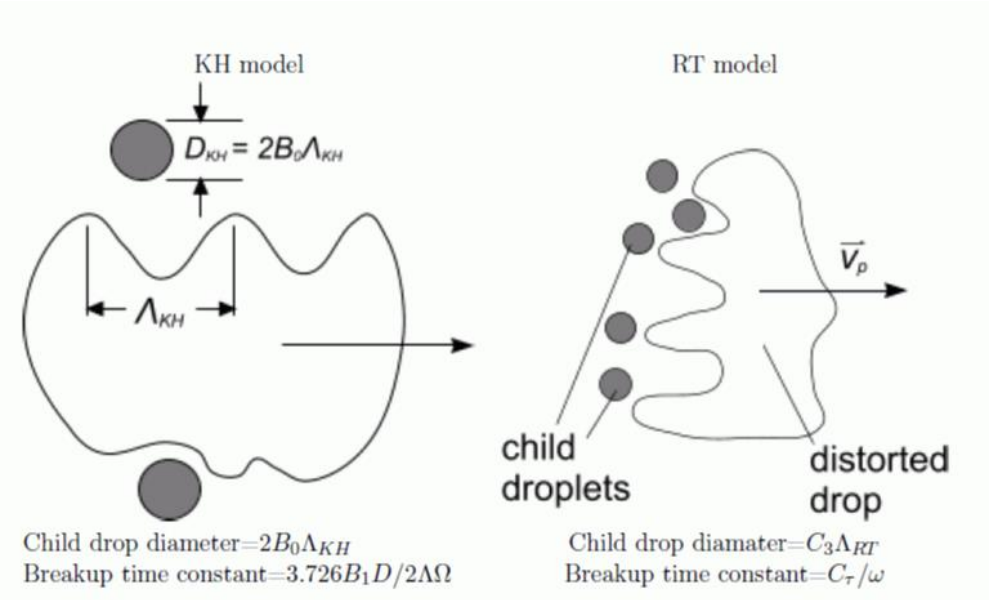

Figure 28. Angles providing plume directions in Eulerian in-nozzle flow simulations

The rate of change of the parent droplet diameter is given by:

$$\frac{d\,D_d}{dt} = -\frac{\left(D_d - D_{d,stable}\right)}{\tau_{KH}} \tag{66}$$

where the characteristic break-up timescale τ_{KH} is calculated using the expression [54],[58]:

$$\tau_{KH} = \frac{3.726\,B_1\,\frac{D}{2}}{\Lambda_{KH}\,\Omega_{KH}} \tag{67}$$

where B_1 is a model constant with default value of 40, and Ω_{KH} is the growth rate of the fastest growing wave. Detailed expressions for the latter can be found in the original publication [19]. As the diameter of the parent droplet shrinks, its total mass decreases. If the difference between the original and the new parcel mass is greater than a given threshold (typically 3% of the original mass) the smaller droplets are shed off to form a new parcel.

For an RT break-up to occur, the droplet diameter should be larger than the wavelength Λ_{RT} of the fastest growing wave, scaled by a constant C_3 (default value is set to 0.1):

$$D = C_3\Lambda_{RT} \tag{68}$$

Furthermore, sufficient time greater than the RT break-up timescale τ_{RT} must have elapsed since the last RT break-up. Λ_{RT} is obtained by calculating the corresponding wave number $k_{RT} = 2\pi/\Lambda_{RT}$ which maximizes the growth rate given by:

$$\omega(k) = -k^2\left(\frac{\mu_l+\mu_g}{\rho_l+\rho_g}\right) + \sqrt{k\left(\frac{\rho_l-\rho_g}{\rho_l+\rho_g}\right)a - \frac{k^3\sigma}{\rho_l+\rho_g} + k^4\left(\frac{\mu_l+\mu_g}{\rho_l+\rho_g}\right)^2} \tag{69}$$

while the characteristic time scale is expressed as:

$$\tau_{RT} = \frac{C_\tau}{\omega_{RT}}, \qquad \omega_{RT} = \omega(k_{RT}) \tag{70}$$

where C_τ is a model constant often set equal to 1.

3.2.3 GruMo Model

GruMo break-up model, whose schematic representation is shown in Figure 29, is similar to the Reitz-Diwakar one but, compared to the latter, it splits the computational domain in two zones, separated by a "transition distance" T_d.

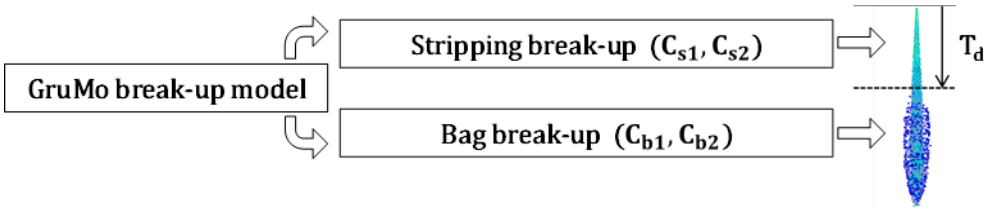

Figure 29. GruMo break-up model scheme

The reason for this separation is related to both experimental evidence and the adopted initialization for the droplets. On the one hand, PDA experimental data for gasoline injectors (available starting from 15 mm after the injector tip and on) reveal that, at 15 mm, droplet dimension is already much smaller than the nozzle hole geometrical diameter and, thereafter, break-up is slow. On the other hand, large droplet diameters are used for the initialization. In fact, initial droplet diameter is set through a modified Rosin-Rammler (RR) distribution whose size constant is the nozzle hole effective diameter, i.e. large enough to be comparable to the geometrical one. In order to combine the adopted initialization (characterized by large droplets) with the experimental data at 15 mm, a fast break-up mechanism is required in the near-nozzle region to quickly lower the diameters. Further away, a much slower break-up rate is adopted, in agreement with the experimental evidence. T_d is therefore introduced, which allows the adoption of two different break-up rates. According to [19], [59], [61], Stripping is assumed near the nozzle, where We_g is higher, while Bag is accounted for downstream T_d. Although the transition distance concept is motivated by physics-based considerations, it is purely empirical. It is, in fact, just a numerical expedient to simplify the calibration and to formulate simple correlation functions between model parameters and operating conditions. In principle, a twofold brake-up rate could be obtained even with existing models (i.e. without imposing a “transition distance”); however,

they are potentially characterized by a continuous competition between the mechanisms everywhere in the domain. In other words, each break-up regime can occur and the predominant one is determined, per each droplet, based on the local conditions. Therefore, it is not possible to determine a priori which type of mechanism a droplet is experiencing. Conversely, via zonalization, the identification of the governing break-up mechanism is straightforward, as it simply depends on the droplet position in the injection domain. This allows a much faster calibration of the model parameters (if needed) and the possibility to easily correlate them with the investigated ambient density. It is useful to point out that T_d is purposely defined as "transition distance" to distinguish it from the break-up length (B_L) concept, widely diffused in many implementations of the KHRT model, such as the one proposed by Braga et al. [62]. Based on experimental observations [63,64], B_L is adopted to eliminate the strong breaking effect of Rayleigh-Taylor instabilities near the nozzle; from the injector tip up to B_L, only Kelvin-Helmholtz submodel is allowed to work. In fact, B_L should represent the length of a region characterized by the presence of a liquid core (or at least ligaments) and where the main phenomenon is the primary break-up, i.e. the disruption of the liquid column and not the droplet secondary break-up. Hence the difference with respect to T_d is straightforward. The latter simply aims at separating the effect of the two considered secondary break-up regimes, without considering the presence of a liquid core region. Moreover, there is another important difference between the two quantities: T_d is constant. If, on the one hand, this remarkably simplifies the tuning process of the secondary break-up model, on the other hand the forced separation of the drop disruption regimes has a non-negligible impact on the GruMo model parameters. In this regard, a critical analysis on the adopted T_d value (15 mm for gasoline injectors and 8 mm for diesel ones) is carried out in the results section, to clarify if it is reasonable (from a physical standpoint) and to evaluate its effect on the GruMo break-up model parameters. Conversely, B_L is variable with the operating conditions and its formulation usually includes a constant C_{BL}. As pointed out by Ren et al. [65], B_L has a huge impact on the results and a proper tune of C_{BL} is mandatory to obtain a good agreement with the experiments. Therefore, from a practical perspective, the adoption of B_L would require further calibration effort.

Compared to the Reitz-Diwakar, the second main difference of the GruMo approach regards the model constants, which become ambient density dependent parameters. In fact, as it will be evident in the result section, traditional models are not able to properly work with the constants suggested in their respective reference papers and, mostly, to provide a reliable estimation of the break-up rate at any condition without an ad-hoc case-by-case calibration of the

constants. This is confirmed by existing literature. In [66] an investigation of a multi-hole gasoline injector for engine applications is carried out by means of the KHRT model, and they conclude that the optimum agreement with the experiments can be achieved with model constants that remarkably differ from the reference literature. In [67] Wang and Zhao investigate an outward-opening piezoelectric gasoline injector by means of the Reitz-Diwakar and KHRT models. As for the former, there is no chance to obtain satisfying results at different backpressures with a unique set of model constants. As for the latter, despite different values compared to the reference paper are adopted, a single set of model constants leads to promising outcomes for both the investigated ambient pressures. However, the numerical-experimental comparisons proposed by Wang and Zhao unsatisfactorily include only liquid jet penetrations. No information is provided in terms of droplet diameter which is the crucial aspect when evaluating the capabilities of a secondary break-up model. In [68] Beale and Reitz test the KHRT model both in Diesel and gasoline injectors and they confirm the need of an ad-hoc (even if minimal) tuning of the model constants moving from Diesel nozzles to gasoline ones. Moreover, for the investigated Diesel atomizers, no information is provided in terms of droplet diameter. As for the analysed gasoline injector, a gaunt comparison in terms of Sauter Mean Diameter (SMD) is provided between simulations and experiments but only focused on a single operating condition. Thus the effectiveness of the calibrated setup is not proven at different conditions. Given the impossibility to adopt a unique setup, attempts to consider variable constants in the secondary break-up model can be found in literature. In [69] Brulatout et al. exploit a design of experiment (DOE) method to obtain effective calibrations of the Reitz-Diwakar and KHRT models on a single Diesel injector operation; then they propose a formulation that allows to extrapolate the C_3 constant included in the wavelength equation of the RT model at different injection pressures compared to the investigated one, to extend the capabilities of the KHRT model. In [70] Costa et al. adopt the same approach (DOE) to calibrate the secondary break-up model constants, based on the operating conditions, in different gasoline injectors. Similarly, in [71] Nsikane et al. use DOE to calibrate, case-by-case, the KHRT constants on the well-known Spray A (provided by the Engine Combustion Network) operated at several conditions. However, the main shortages of the works proposed by Brulatout, Costa, Nsikane and their respective co-workers deal with the lack of a validation against droplet size experimental data. Only liquid and vapour penetrations are considered. In addition, compared to Brulatout which corrects a posteriori the calibration resulting from DOE proposing a somewhat consistent behaviour of C_3 Costa and Nsikane show trends that seem to be not fully coherent (or at least

hard to be explained). In [72] Van Dam and Rutland investigate a multi-hole GDI injector over wide ranges of ambient pressure and temperature, with both Large Eddy Simulation (LES) and Reynolds-Average Navier-Stokes Equation (RANS) approaches to turbulence. After ad-hoc calibrations of the spray model at the different investigated conditions, they propose correlations to modify the KHRT model constants based on the specific conditions, mostly in terms of ambient density. However, even in this case, only liquid and vapour penetrations and imaging are considered for comparison against the experiments. No information is provided in terms of droplet diameters.

Similarly to the work of Van Dam and Rutland, in the present manuscript the constants of the proposed GruMo model become variable parameters to be modified based on the conditions. However, another noteworthy novelty of the present work is that the proposed parameter values are extensively validated against experimental measures of particle size and velocity, which is the most important aspect when the attention is focused on secondary break-up models. Moreover, the calibration of the parameters is carried out manually for each single investigated condition. As it will be visible in the result section, this is fundamental to obtain simple, linear, and coherent trends for the GruMo model parameters.

For the GruMo model implementation, the first quantity to be defined is the distance of each droplet from the nozzle $DIST_{inj}$:

$$DIST_{inj} = \sqrt{\left(x_{inj} - x_d\right)^2 + \left(y_{inj} - y_d\right)^2 + \left(z_{inj} - z_d\right)^2} \tag{71}$$

where x_{inj}, y_{inj}, z_{inj} and x_d, y_d, z_d are the coordinates of injector tip and droplet, respectively. If $DIST_{inj} \leq T_d$, only Stripping regime is enabled, and the condition for the latter to take place is reported in equation (72), from which a quantitative estimation of the stable droplet diameter $(D_{Stripping})$ can be inferred. In fact, stripping condition reduces to a comparison in terms of drop diameter. Break-up occurs only if droplet diameter is larger than $D_{Stripping}$. Droplets for which Stripping condition is not satisfied do not undergo break-up between injector tip and T_d. Characteristic time of break-up is reported in equation (73). Both $D_{Stripping}$ and $\tau_{Stripping}$ are inherited from the original Reitz-Diwakar model. It is interesting to point out that, unlike for example in Arcoumanis et al. [73] and Pilch et al. [60], stripping condition does not simply consist in a threshold to be overcome by We_g, but it relies on both Weber and Reynolds numbers. Such

criterion was originally proposed by Rabin et al. [74] which experimentally investigated the liquid shearing off the periphery of a non-burning Rocket Propellant-1 drop.

$$\frac{We_g}{\sqrt{Re_d}} > C_{s1} \rightarrow D_d > \frac{4C_{s1}^2\,\sigma_d^2}{\rho_{gas}\,\mu_{gas}\,v_{rel}^3} = D_{Stripping} \tag{72}$$

$$\tau_{Stripping} = \frac{C_{s2}}{2}\left(\frac{\rho_d}{\rho_{gas}}\right)^{1/2}\frac{D_d}{v_{rel}} \tag{73}$$

C_{s1} and C_{s2} are model parameters. In the original version of the Reitz-Diwakar model, the former is equal to 0.5 and the latter ranges from 0.5 to 20. ρ_d, D_d and σ_d are density, diameter, and surface tension of the droplet. ρ_{gas} and μ_{gas} are density and molecular viscosity of the gas. If $DIST_{inj} > T_d$, a Bag-like break-up is assumed. Stable droplet diameter (D_{Bag}) and characteristic time of break-up (τ_{Bag}) are inherited from the Reitz-Diwakar model and reported in the following equations:

$$We_g > C_{b1} \rightarrow D_d > \frac{2\,C_{b1}\,\sigma_d}{\rho_{gas}\,v_{rel}^2} = D_{Bag} \tag{74}$$

$$\tau_{Bag} = \frac{C_{b2}\,\rho_d^{1/2}\,D_d^{3/2}}{4\sigma_d^{1/2}} \tag{75}$$

$\mathrm{C_{b1}}$ and $\mathrm{C_{b2}}$ are model parameters. In the original version of the Reitz-Diwakar model the former is set to 6 according to Wierzba [75] and the latter is equal to π.

Regardless the mechanism, the break-up rate is calculated in the following equation:

$$\frac{dD_d}{dt} = \frac{(D_d - D_{d,stable})}{\tau_b} \tag{76}$$

where stable diameter ($D_{d,stable}$) and characteristic time of break-up (τ_b) can be equal to $D_{Stripping}$ and $\tau_{Stripping}$ or D_{Bag} and τ_{Bag}, based on the distance from the injector tip.

3.3 Flash-Boiling Model

In GDI engines, at specific conditions, flash boiling can occur both inside and outside the nozzles and it massively impacts spray characteristics. However, internal nozzle flow simulations via a Eulerian approach imply significant computational efforts and require detailed CAD geometry of the injector. To provide an accurate prediction of droplet characteristics at nozzle exit under flash boiling conditions, 0D sub models can be adopted. In STAR-CD, the flash boiling atomization and evaporation models developed by Price [76,77] are implemented in combination with the vapor bubble breakup model proposed by Senda [78]. The latter considers flash boiling effects on droplet breakup after injection.

3.3.1 Flash-boiling Atomization Model

Experimental outcomes show that the amount of flash boiling is mainly determined by superheat degree ΔT_{SD} , defined as:

$$\Delta T_{SD} = T_{inj} - T_{sat,\infty} \tag{77}$$

where T_{inj} is the injection temperature and $T_{sat,\infty}$ is the saturation temperature at ambient pressure. It is assumed that the flash boiling atomization model is activated when superheat rises above a predefined threshold value, for example 10 K. When flash boiling occurs, the injected droplet velocity is obtained from:

$$U_{eff} = \frac{A_n}{\dot{m}} (P_s - P_\infty) + U_{vena} \tag{78}$$

where A_n is the nozzle area, $\dot{m}$ is the mass flow rate of injection, P_s is the saturation pressure at the fuel injection temperature, and P_∞ is the ambient pressure. The velocity at the vena contracta U_{vena} is obtained from:

$$U_{vena} = \frac{\dot{m}}{A_n \rho_l C_c} \tag{79}$$

where ρ_l is the density of the liquid, and C_c is the contraction ratio defined as the ratio between the mean velocity and the U_{vena}. In this work C_c is calculated with an empirical formula. The spray cone angle is modelled as [77]:

$$\theta = a\beta^2 + b\beta + c \tag{80}$$

where β is a non-dimensional parameter that depends on the ratio between the saturation pressure and the ambient pressure as well as on the surface tension of the fuel. Default values of the coefficients a, b and c are -3.208, 366.61 and -10324 respectively. At flash boiling conditions, vapour is generated inside the nozzle and the resulting volume flowrate $\dot{V}_{vap}$ is calculated as:

$$\dot{V}_{vap} = N_{nuc}\, f\, V_b\, S_{nozzle} \tag{81}$$

where N_{nuc} is the nucleation site density per unit surface area, V_b is the bubble departure volume, f is the bubble departure frequency, and S_{nozzle} is the inner surface area of the nozzle orifice. The liquid volume flowrate is calculated as:

$$\dot{V}_{liq} = \dot{V}_{total} - \dot{V}_{vap} \tag{82}$$

Making the hypothesis that the liquid volume flowrate corresponds to the volume of the droplet exiting the nozzle, it is possible to evaluate the initial droplet diameter as:

$$D_d = \left(\frac{6\,\dot{V}_{liq}}{\pi}\right)^{\frac{1}{3}} \tag{83}$$

The flash boiling atomization model estimates the effective velocity of the droplets U_{eff}, their diameter at the nozzle exit D_d, and the cone angle θ considering flash boiling effects such as vapor generation inside the nozzle and reduction of efflux section.

3.3.2 Flash-boiling Evaporation Model

In addition to the mass transfer $\dot{m}_{sc}$ predicted by the standard evaporation model, driven by heat transfer from ambient gas to droplets, evaporation due to flash boiling is predicted with an additional term $\dot{m}_{sh}$ [76]:

$$\dot{m}_{sc} = AP\frac{ShD_i}{T_f R_f D_d}\ ln\left(\frac{P\ -P_v}{P\ -P_s}\right) \tag{84}$$

$$\dot{m}_{sh} = \frac{A\alpha\Delta T_{SD}}{H_l} \tag{85}$$

where A is the droplet surface area, P is the ambient pressure, Sh is the non-dimensional Sherwood number, D_i is the binary diffusion coefficient, T_f is the temperature of the vapor film, R_f is the specific gas constant of the vapor film, P_v is the partial vapor pressure in the cell, P_s is the saturation pressure of the fuel, H_l is the latent heat of vaporization, and α is the overall heat transfer coefficient given by empirical functions [77]:

$$\begin{aligned} \alpha &= 760\ \Delta T_{SD}^{0.26}\ if\ 0 \leq\ \Delta T_{SD}\ \leq 5 \\ \alpha &= 27\ \Delta T_{SD}^{2.33}\ if\ 5 \leq\ \Delta T_{SD}\ \leq 25 \\ \alpha &= 13800\ \Delta T_{SD}^{0.39}\ if\ \Delta T_{SD}\ \geq\ 5 \end{aligned} \tag{86}$$

3.3.3 Flash-boiling Droplet Break-Up Model

Flash boiling can occur outside the nozzle as well, promoting droplet break-up and leading to significantly smaller droplets. In this paper the bubble nucleation and growth model of Senda [80] is adopted for the simulation of droplet breakup due to flash boiling occurring inside droplets outside of the nozzle. Firstly, bubbles are created through a nucleation process within the droplets, whose bubble number density N is obtained from:

$$N = C\ exp\left(\frac{-\Delta A}{\Delta T_{SD}}\right) \tag{87}$$

where C and ΔA are model constants having values of 1.11x1012 and 5.28, respectively. Bubble growth is secondly modelled by solving the following equation:

$$R\ddot{R} + \frac{3}{2}\dot{R}^2 = \frac{1}{\rho}\left(P_w - P_\infty\right) \tag{88}$$

and

$$P_w = P_s + \left(P_{r0} + \frac{2\sigma}{R_0}\right)\left(\frac{R_0}{R}\right)^{3n} - \frac{2\sigma}{R} - \frac{4\mu_l\dot{R}}{R} - \frac{4k\dot{R}}{R^2} \tag{89}$$

where R is the bubble radius, R_0 is the initial bubble radius (with 10 µm default value), P_∞ is the ambient pressure, P_{r0} is the pressure at the nozzle orifice, μ_l is the liquid viscosity, σ is the surface viscosity coefficient set by default to 1.25x10-5 Ns/m. Droplet breakup due to flash boiling only occurs when the bubble volume fraction ε exceeds a threshold volume fraction ε_{max} set to 0.55:

$$\varepsilon = \frac{V_{bubble}}{V_{bubble} + V_{liquid}} > \varepsilon_{max} \tag{90}$$

When droplet breakup occurs, the number of child droplets generated is taken as twice the number of bubbles.

4. Numerical Setup

4.1 Numerical Setup – Primary Break-Up Study

As for the Lagrangian simulations, the computational domains consist in a block-shaped vessel whose characteristic dimensions are 40x40x80 mm for the Spray G, and 130x140x180 mm for the INJ3. The computational meshes consist of hexahedral cells with cone-shaped refinements, whose minimum size is set to 0.5 mm for both injectors [81]. Spray G minimum cell size value was chosen in accord to the ECN community standards, to have a good compromise between simulation accuracy and computational cost [90]. Images of computational vessels are reported in Figure 30 and Figure 31.

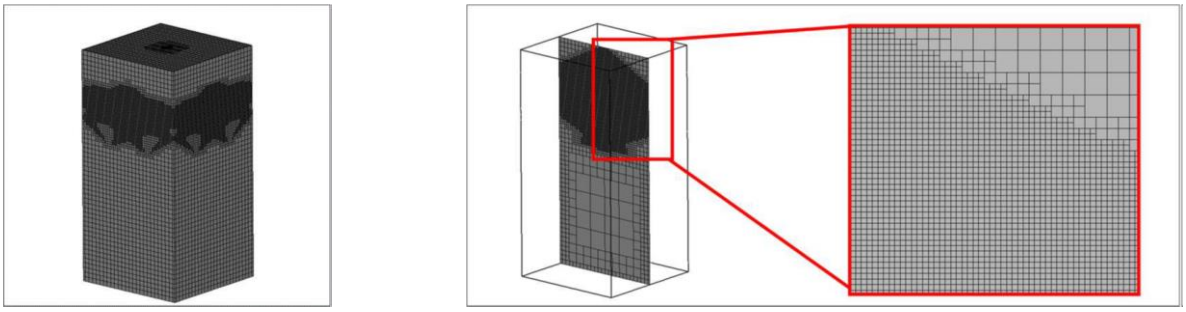

(a) (b)

Figure 30. (a) Numerical grid of computational vessel adopted for the Spray G 3D-CFD simulations; (b) Mesh section with cone-shaped mesh refinements for the Spray G vessel.

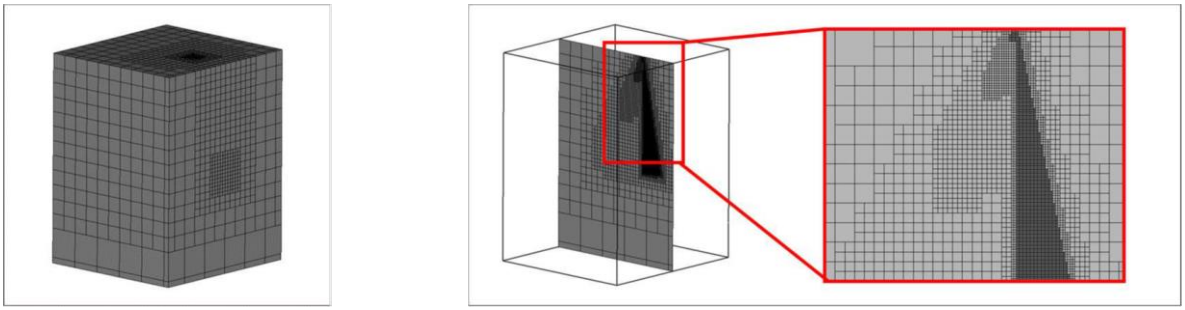

(a) (b)

Figure 31. (a) Numerical grid of computational vessel adopted for the INJ3 3D-CFD simulations; (b) Mesh section with cone-shaped mesh refinements for the INJ3 vessel.

A Reynolds-averaged Navier-Stokes (RANS) approach to turbulence is adopted for all the simulations. The widely diffused k-ε RNG two-equation turbulence model is adopted [82]. A combined Eulerian-Lagrangian approach allows to properly account for both vessel gaseous ambient and the dispersed liquid phase [40]. The second order Monotone Advection and Reconstruction Scheme (MARS) numerical scheme is adopted for momentum, temperature, and turbulent quantities transport equations. For both the injectors, 15 parcels are injected from each single nozzle at every time-step; the latter is equal to $1 \cdot 10^{-6}\, s$ with the purpose to keep the maximum Courant number well below unity. The computational domain is initialized with the experimental pressure and temperature values; since vessel is supposed to be quiescent, 'k' and 'ε' initial values are set equal to 0. Apart from the top of the domain, which is treated as a non-slip adiabatic wall, all other boundaries are set as pressure outlets. Single-component Lagrangian parcels are injected, whose properties are inherited from the National Institute of Standards and Technology (NIST) database both for the liquid and the vapor phase [83]. For both injectors, experimental injection rate profiles are adopted as mass flow rates. Moreover, the syringe-like effect described in [27] is taken into account to improve numerical outcomes during the first stage of injection. In fact, the first numerical liquid parcel was not injected when injection rate is greater than zero. Rather, the numerical injection timing is fixed as the instant, detected by the experimental high-speed imaging, at which liquid exits from the nozzle holes, which is approximately equivalent to the instant at which cumulative injected volume become positive. As a consequence of this effect, both initial mass flow rates and velocities are characterized by non-zero values. Primary break-up is replaced by a simplified blob model, and as for the secondary break-up, only Reitz's model is considered for the analysis of the INJ3. For the Spray G, both Reitz's and KHRT models are used. For all the simulations proposed in the primary-break up study, no secondary break-up model constants are modified compared to the reference papers [18,19],[61].

As for the INJ3, droplet initial diameters are mainly based on experimental outcomes, and are equal to 8,7, and 6 μm for injection pressure of 20, 40, and 60 MPa, respectively. As for the initial droplet velocities at start of injection, values are chosen to match penetration curves, while static initial velocities are estimated from experimental static mass flow rates. For all the investigated conditions, the cone angle of each single plume is set equal to 30°, as indicated by the experiments.

As for the Spray G, at first the same droplet initialization strategy is adopted. In particular, the initial droplet diameter is set equal to nearly 10 μm, which roughly corresponds to the experimental SMD measured on a plane 15 mm away from the injector tip. As for the static initial droplet velocity, a reliable estimation can be obtained thanks to the availability of the hydraulic coefficients, as reported in Chapter 2. Initial droplet velocity at the start of injection is determined, similarly to the previous injector, in order to match penetration curves at the first stage of the injection. Finally, the cone angle of each single plume is set equal to 30°, as reported by experimental outcomes. Afterwards, in order to understand the effect of droplet initial diameter on the spray development, larger initial diameters are also investigated (20, 50, 80, and 110 μm).

Inner-nozzle flow simulations are carried out with a dedicated methodology, developed during the PhD activity, for the Spray G injector, at the same operating condition considered for the Lagrangian simulations. Among the different CAD files available on the ECN website, the so called "Generation 1" is considered, which represents the nominal geometry of the injector, with nozzle diameters equal to 165 μm. Static condition with a needle-lift equal to 45 μm is simulated (corresponding to the maximum one) [51]. As for the computational mesh, polyhedral cells are adopted in the core region, while prism layers are preferred at the walls, to improve near-wall modeling. Mesh refinements are locally introduced, such as in the needle seat region. Minimum and maximum cell sizes are 10 μm and 50 μm, respectively [84]. The total number of fluid cells is nearly seven million. The computational domain and related numerical grid are reported in Figure 32.

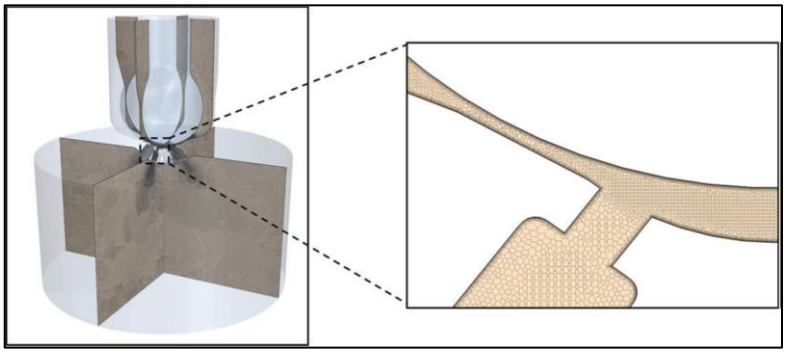

Figure 32. Computational domain and numerical grid adopted in the inner-nozzle flow simulation

As for the CFD setup, a steady Eulerian Multiphase approach is adopted along with the VOF model described in Chapter 1 , which is able to predict the distribution of the interface between immiscible phases. The Schnerr-Sauerr cavitation model is used to predict the vapour formation close to the nozzle [89]. In order to prevent numerical instabilities, properties (such as density and viscosity) are constant and calculated at the injection temperature. Time-step size is equal to $1 \cdot 10^{-7} s$ to accomplish the Courant-Friedrichs-Lewy condition. Boundary conditions are depicted in Figure 33.

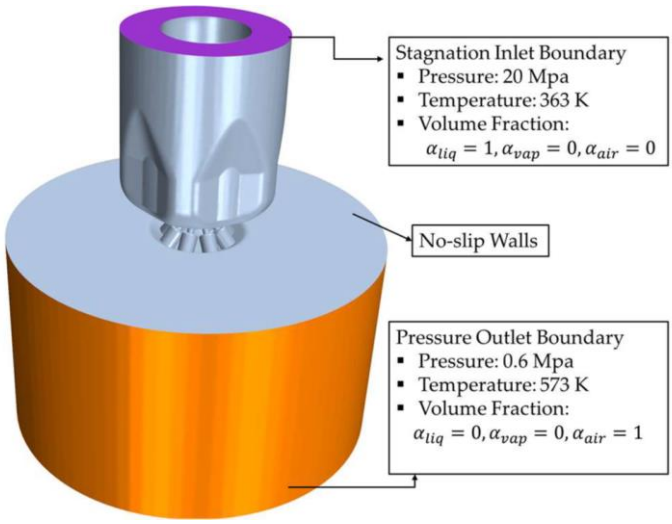

Figure 33. Boundary types used in the inner-nozzle flow simulation.

As for the turbulence modeling, the two-equation k-ω SST model [39] is adopted to close the set of Reynolds-Averaged Navier-Stokes equations. The so called "All-y+" wall treatment is preferred for the near wall modeling [85,88]: this model relies on a hybrid approach able to work as a Low-Reynolds wall treatment for y+ values belonging to the viscous sub-layer, and as a High-Reynolds one for y+ values pertaining to the fully turbulent region. In order to compare numerical and experimental outcomes, sections are purposely created at hole exits (before the hole steps), as reported in Figure 34. Such sections are used to measure quantities such as mass flow rate and hydraulic coefficients.

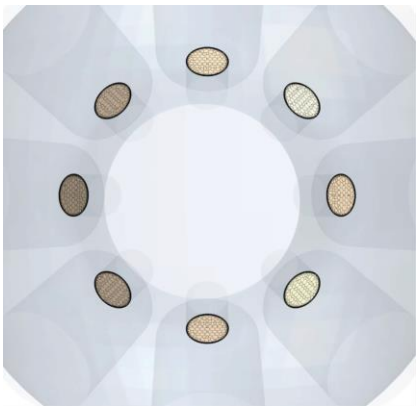

Figure 34. Output nozzle sections used for the evaluation of simulation outcomes.

4.2 Numerical Setup – Secondary Break-Up Study (GDI)

As for the Eulerian in-nozzle flow simulations, only the internal-nozzle geometry of the INJ1 is available. The same approach described in the previous paragraph for the Spray G is employed, and all the INJ1 operating conditions are investigated, in order to analyse the effect of ambient pressure variations on the hydraulic coefficients of the injector. A mesh made of predominantly hexahedral cells is adopted in the core region, with a characteristic cell size of 40 µm. Refinements down to 10 µm are introduced near the needle seat and the nozzle. A multi-layer prismatic mesh is chosen at the walls, to enhance the near-wall modelling. Specifically, 10 layers are adopted with a total thickness of 10 µm. Only a quarter of the original geometry is simulated, according to the symmetry on x-z and y-z planes. The total number of fluid cells is nearly 1.5 million; simulations are performed with a needle lift equal to 100 µm (corresponding to the maximum one). A detail of the mesh is reported in Figure 34. Boundary conditions are depicted in Figure 35.

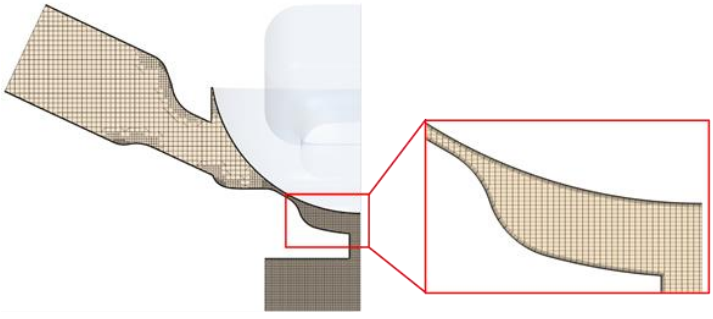

Figure 34. Computational mesh for the in-nozzle flow simulations of the INJ1.

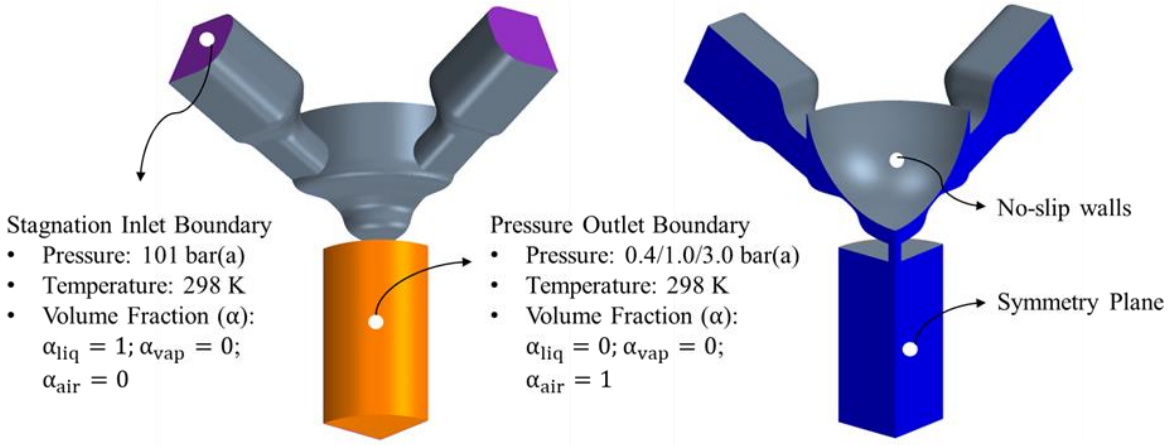

Figure 35. Boundary conditions for the in-nozzle flow simulations of INJ1.

Lagrangian simulations are carried out in quiescent chamber for all the injectors. Computational domains are block-shaped vessels whose characteristic dimensions are 60 x 60 x 160 mm for the INJ1, 65 x 65 x 160 for the INJ2 and 65 x 70 x 180 mm for the INJ3. For all the injectors, symmetries are exploited. In particular, for the INJ1 only a quarter of the domain is considered due to symmetries with respect to x-z and y-z planes. For the remaining injectors, only the symmetry around y-z plane is accounted for. Numerical grids consist of hexahedral cells, and they include cone-shaped refinements for the spray core region, with cell size of 0.5 mm (common for all the injectors). This value represents a trade-off between a limited computational cost and a reduced mesh dependency [90]. Numerical grids are shown in Figure 36.

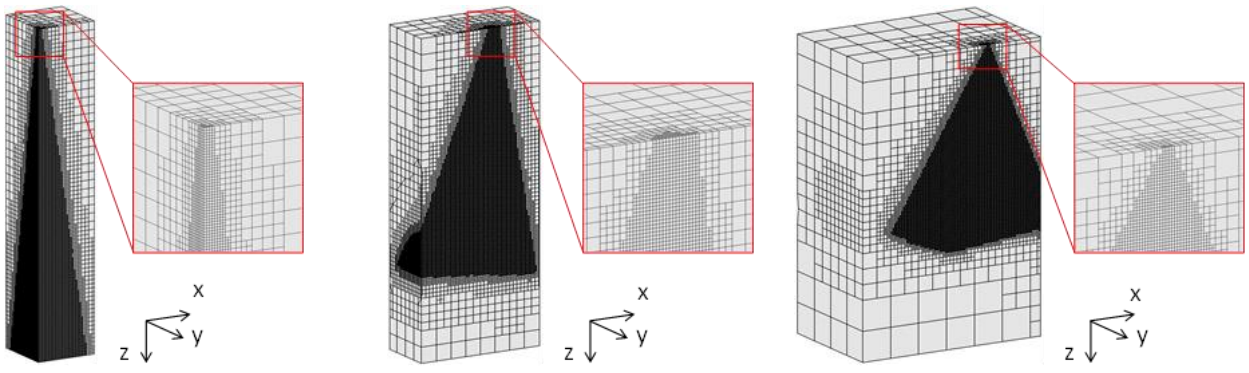

Figure 36. Numerical grids, along with details, for INJ1, INJ2, and INJ3 in the seconary break-up study.

Same Lagrangian setup described in the previous paragraph is used for all the three injectors. The atomization is replaced by a blob model in which the initial diameter is imposed via distribution function, and the disruption of the big droplets (namely blobs) which should replicate the primary

break-up is demanded to the secondary break-up model. Blob initial conditions derive from the experimental momentum outcomes as widely described in the Chapter 3. It is important to point out two aspects. Firstly, the INJ3 is characterized by holes of equal diameter and similar momentum fluxes, therefore, for the sake of simplicity, the total momentum flux is assumed to be equally distributed among the holes. For this reason, mass flow rate, hydraulic coefficients and droplet initial conditions are common for all the jets. Secondly, since the experimental momentum measures are available at 1 bar(a) of back pressure, hydraulic coefficients can be obtained only at the same condition. As a consequence:

- for the INJ1, $C_{d,i}$, $C_{a,i}$ and $C_{v,i}$ are missing for the other analysed ambient pressures (i.e. 0.4 and 3 bar(a)). However this is not a critical limitation. In fact, for reduced variations of the back pressure, the differences in terms of hydraulic coefficients are negligible. In order to prove such behaviour, Eulerian internal-nozzle simulations on the INJ1 are proposed for the three different investigated conditions. As it will be shown afterwards, the hydraulic coefficients provided by the Eulerian analyses result nearly the same for all the back pressures, confirming that a unique set of values can be used for the different operations.
- for the INJ2, coefficients are available for a back pressure which slightly differs from the investigated one, the latter being equal to 0.4 bar(a). Nevertheless, as a consequence of the Eulerian simulation findings on the INJ1, for the INJ2 the hydraulic coefficients obtained via experiments at 1 bar(a) can be exploited at 0.4 bar(a) of back pressure.
- for the INJ3, no assumption is needed as hydraulic coefficients are available at 1 bar(a) which corresponds exactly to the investigated back pressure.

Table 8 resumes, for all the injectors, the experimentally derived hydraulic coefficients, and the consequent values of $D_{eff,i}$ and $v_{eff,i}$ obtained with the methodology previously outlined, to be adopted in the Lagrangian simulations.

	INJ1	INJ2	INJ3
C_d	0.684	0.580	0.536
C_a	0.728	0.620	0.673
C_v	0.940	0.934	0.796
D_{eff} [µm]	171	138	103
v_{eff} [m/s]	160	160	136

Table 8. Hydraulic coefficients and resulting initial droplet conditions, experimentally derived at 1 bar, for the INJ1, INJ2, and INJ3 in the secondary break-up study.

As for the initial diameter, it is imposed via a modified RR distribution, whose formulation is here reported:

$$D_{RR} = D_{eff}\ (-ln\ (1 - Y))^{\frac{1}{5}} \tag{91}$$

Y is the mass fraction of the droplets with diameter less than D_{RR}. The distribution mean diameter and exponent are equal to D_{eff} and 5 respectively. A modification of the distribution function reported in equation (91) is made afterwards clipping the maximum diameter, as shown in the following equation:

$$\begin{cases} if\ D_{RR} \leq D_{eff}\ \rightarrow D_d = D_{RR} \\ if\ D_{RR} > D_{eff}\ \rightarrow D_d = D_{eff} \end{cases} \tag{92}$$

In fact, for most of the droplets, the initial diameter can be reasonably estimated as prone to D_{eff} and this is the reason why the size constant of the RR is fixed to D_{eff}. But simultaneously, droplet diameter cannot be larger than the effective diameter of the hole (namely D_{eff}), that is why the maximum value is limited to D_{eff}. The resulting cumulative volume distributions are depicted in Figure 37.

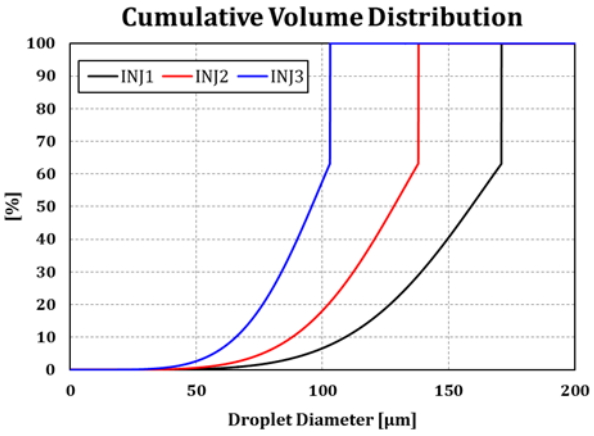

Figure 37. Modified Rosin-Rammler volume distribution for INJ1, INJ2, and INJ3 in the secondary break-up study

The semi-cone angle is fixed to nearly 3°, 12° and 15° for INJ1, INJ2 and INJ3 respectively. As for the first, the same angle is adopted for all the conditions. As for the last, the same value is exploited for all the nozzle holes. The GruMo model is employed for the secondary break-up for all the investigated injectors and conditions. For comparison, two widely diffused models are used as well, namely the Reitz-Diwakar and the KHRT, for which the adopted constants are equal to the values found in the reference papers [18,19],[61].

4.3 Numerical Setup – Secondary Break-Up Study (Diesel)

As for the study of the secondary break-up of Diesel injectors, Spray A, Spray C, and Spray D are analysed through Lagrangian simulations. Computational domain consists in a cube-shaped vessel whose characteristic dimension is 108 mm for Spray A and 124 mm for both Spray C and Spray D. The numerical grid consists of hexahedral cells, and it includes refinement in the spray core region, whose dimensions are reported in Figure 38. The characteristic cell size in the refinement is 0.5 mm, common for all the injectors.

Spray	A	C, D
L1 [mm]	8	16
H1 [mm]	20	35
L2 [mm]	30	45
H2 [mm]	40	50

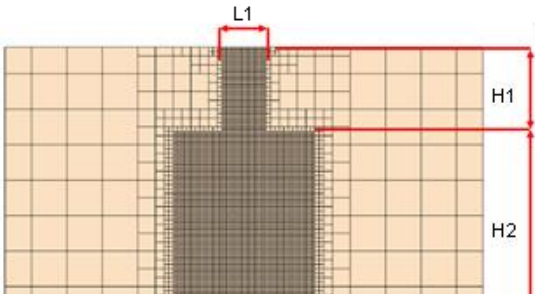

Figure 38. Numerical grids adopted for Spray A, Spray C, and Spray D.

Turbulence is modelled via a Reynolds-Averaged Navier-Stokes (RANS) approach for all the simulations. In particular, the k-ε STANDARD two-equation turbulence model is adopted for all the injectors. A combined Eulerian-Lagrangian approach is employed to properly represent both the vessel gaseous ambient and the dispersed liquid phase. The second order numerical Monotone Advection and Reconstruction Scheme (MARS) is adopted for momentum, temperature, turbulent quantities, and scalars transport equations. Time-step is nearly 1e-7 s to hold the maximum Courant number below unity, while the number of injected parcels per time-step is set equal to 30 for each injector. Computational domain is initialized with experimental pressure and temperature values and, to replicate the experimental quiescent vessel conditions, initial turbulent intensity is set equal to 0 for all the cases. All the boundaries are set as a non-slip adiabatic wall. Properties of the single-component fuel are inherited from the National Institute of Standards and Technology (NIST) database for both the liquid and the vapour phases [83]. Mass flow rate for each injector is provided by the ECN and the syringe-like effect described in [27] is considered to improve numerical results during the ballistic stage of the injection. Atomization is replaced by a blob model with distribution function, and disruption of the big drops (namely blobs) which should replicate the effect of the primary break-up is demanded to the secondary break-up model. Blob initial conditions derive from the hydraulic coefficients provided by ECN, described in Chapter 3 . The initial diameter relies on the nozzle effective diameter, which is evaluated from the geometrical one and the area coefficient, and it is imposed via a Rosin-Rammler (RR) distribution whose diameter and exponent are equal to the nozzle effective diameter and 5, respectively. The RR distribution is modified clipping the maximum diameter to the nozzle effective one. As for the initial velocity, it is calculated from the velocity coefficient, which in turn corresponds to the ratio between discharge and area coefficients. The GruMo secondary break-up model is applied for the standard operating condition (ambient density equal to 22.8 kg/m^3) and for all the injectors with the same constants: Cb1 = 1.5, Cb2 = 0.8, Cs1 = 0.5 and Cs2 = 17.5. A comparison with the widely diffused Reitz-Diwakar model [18],[54] is carried out, with model constants extrapolated from the reference papers: Cb1 = 6, Cb2 = 3.14, Cs1 = 0.5 and Cs2 = 20.

As for the Spray A, sensitivities of different parameters are carried out, in order to understand the effects on numerical outcomes in terms of both liquid and vapor penetration:

- Ambient density sensitivity: simulations with three different ambient densities are carried out (7.6, 15.2, and 22.8 kg/m3) in order to extend the validity of the GruMo model parameter correlations to Diesel injectors.
- Turbulence model sensitivity: a comparison between the k-ε STANDARD and the k-ε RNG model is carried out, at the standard operating condition, using the GruMo secondary break-up model.
- Mesh size sensitivity: a comparison between cell size in the mesh refinement equal to 1.5, 1.0, 0.5, and 0.4 mm is carried out at the standard operating condition, using the GruMo secondary break-up model.
- Number of parcels sensitivity: different values of injected parcels per time-step (15, 30, and 60) are tested at the standard operating condition, using the GruMo secondary break-up model.
- Time-step sensitivity: time-step values of $5 \cdot 10^{-8}\, s$, $1 \cdot 10^{-7}\, s$, and $5 \cdot 10^{-7}\, s$ are investigated at the standard operating condition, using the GruMo secondary break-up model.

4.4 Numerical Setup – Flash Boiling Study

Lagrangian simulations of the INJ2 are carried out in both standard and flashing conditions (reported in Chapter 2), to evaluate the new flash-boiling model implemented by Siemens in the commercial code STAR-CD. The same setup described in the paragraph 4.2 is adopted for such simulations, in terms of numerical grid, droplets initialization, turbulence model, number of injected parcels, and time-step. As for the spray semi-cone angle, in the subcooled case it is imposed equal to 12° according to the experimental imaging; for the flashing case, the semi-cone angle value is calculated by the flash boiling atomization model. As for the secondary break-up, the Reitz-Diwakar model [18], [54] is adopted; values of the model constants are calibrated in the subcooled case and then they are retained in the flashing one, with the aim to evaluate the reliability of the flash boiling breakup model contribution to the estimation of the reduction of droplet size due to bubbles burst inside the liquid droplets.

5. Results – Primary break-up Analysis

In this chapter, numerical results of the Spray G and the INJ3 are depicted, with the aim to understand the effect of the droplet initial diameters on 3D-CFD Lagrangian simulations of injection processes.

Starting from the INJ3, The first comparison between numerical and experimental data deals with liquid penetrations. Comparisons at 20, 40 and 60 MPa are reported in Figures 39-41 respectively:

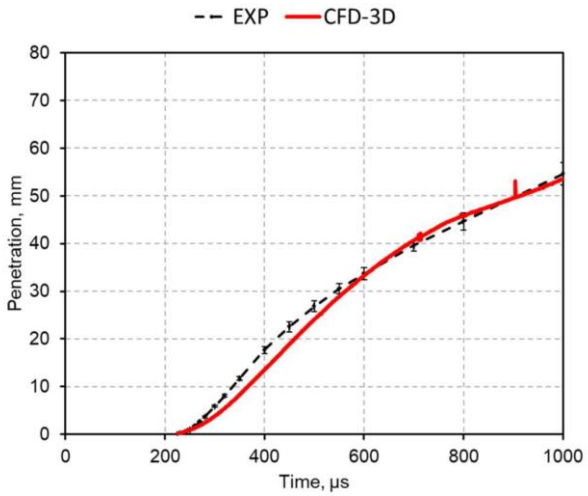

Figure 39. Comparison between numerical and experimental penetrations for the INJ3 at 20 MPa.

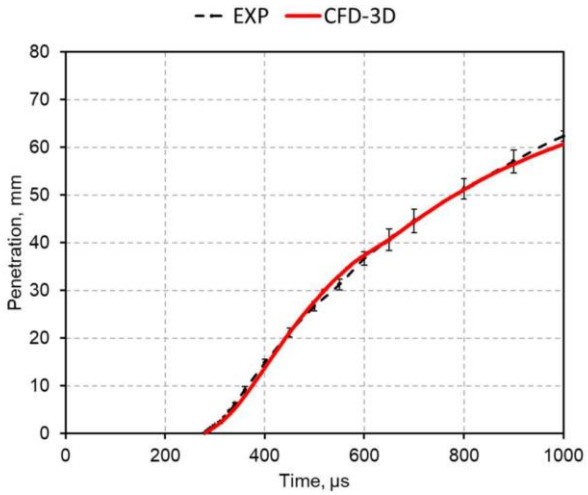

Figure 40. Comparison between numerical and experimental penetrations for the INJ3 at 40 MPa.

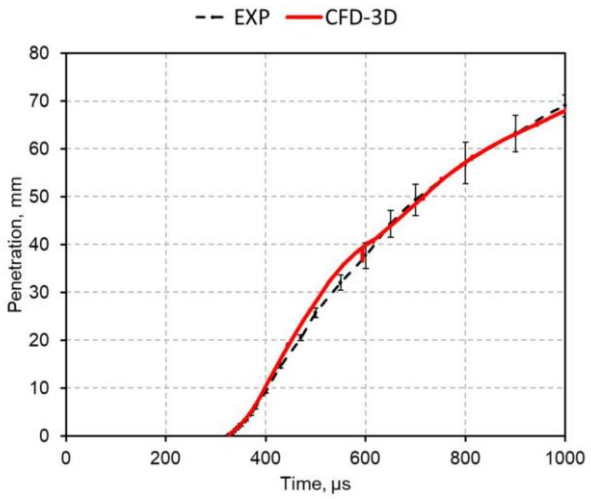

Figure 41. Comparison between numerical and experimental penetrations for the INJ3 at 60 MPa.

It is useful to point out that numerical spray penetrations are computed as the distance from the injector nozzle outlet section at which 99 % of the plume mass is met, consistently with a widely diffused practice [91]. Moreover, for all the conditions, despite liquid penetration along the injector axis considers the whole spray, it is always determined by the central plume whose axis is almost coincident with the injector one. That said, numerical penetrations closely reproduce experimental outcomes for all the investigated conditions. As for the comparison in terms of PDA data, experimental values represent an average over a specific time interval; for a proper comparison, the same time average is considered also for the numerical results. PDA comparison is carried out at 20, 30, 40, and 50 mm downstream the injector tip, as reported in Chapter 2. From the tip up to a 20 mm distance, experimental data spherical validation is too low to ensure reliable outcomes: this is the reason why, at 20 mm, differences between experimental and numerical outcomes are most evident, as visible in Figure 42 and Figure 43. At 30, 40 and 50 mm, experimental mean droplet diameters (D10) and velocities are reasonably matched by numerical results for each analysed injection pressure. In fact, both experiments and simulations show a decrease of the geometric diameter for increasing injection pressures. It is worthwhile to point out that initial droplet diameters and values measured at 20, 30, 40, and 50 mm away from the tip are very similar, which proves that secondary break-up poorly affects results for the chosen numerical setup in terms of initial diameters. As for the average velocities, it is interesting to note that, despite an increasing initial velocity with injection pressure, an inversion of the trend can be

noticed for injection pressures higher than 40 MPa. This behaviour is well captured by both simulations and experiments.

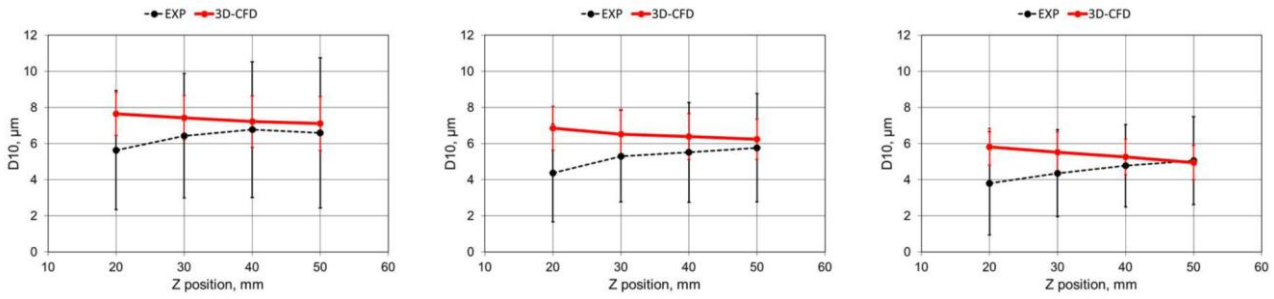

(a) (b) (c)

Figure 42. Comparison between numerical and experimental mean diameters for the INJ3 at: (a) 20 MPa (b) 40 MPa and (c) 60 MPa.

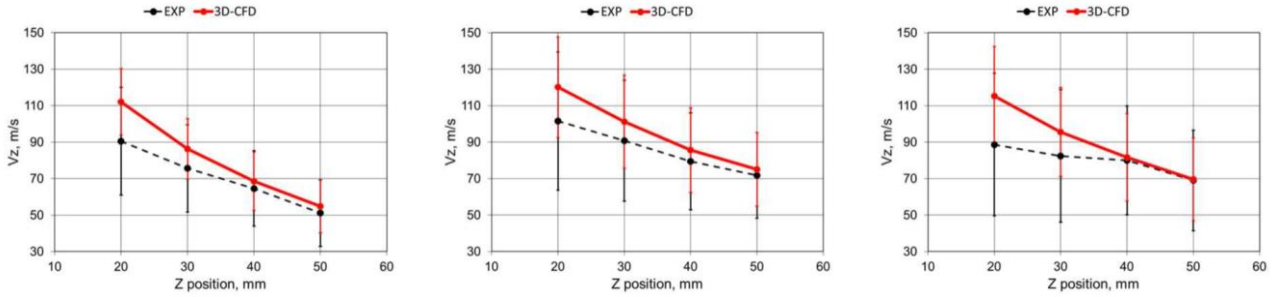

(a) (b) (c)

Figure 43. Comparison between numerical and experimental mean velocities for the INJ3 at: (a) 20 MPa (b) 40 MPa and (c) 60 MPa.

The last comparison between experimental and numerical data, for the INJ3, is carried out in terms of imaging. Significative snapshots during the injection event are chosen and reported in Figures 44-46.

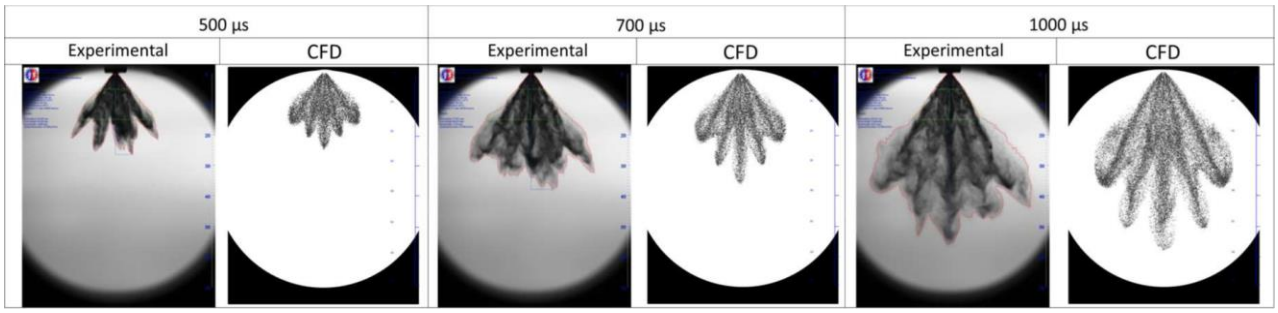

Figure 44. Comparison in terms of imaging between simulations and experiments for the INJ3 at 20 MPa.

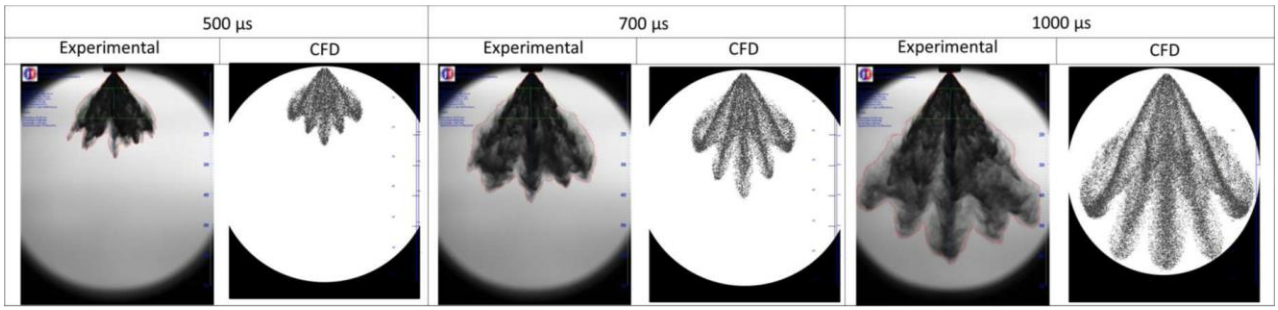

Figure 45. Comparison in terms of imaging between simulations and experiments for the INJ3 at 40 MPa.

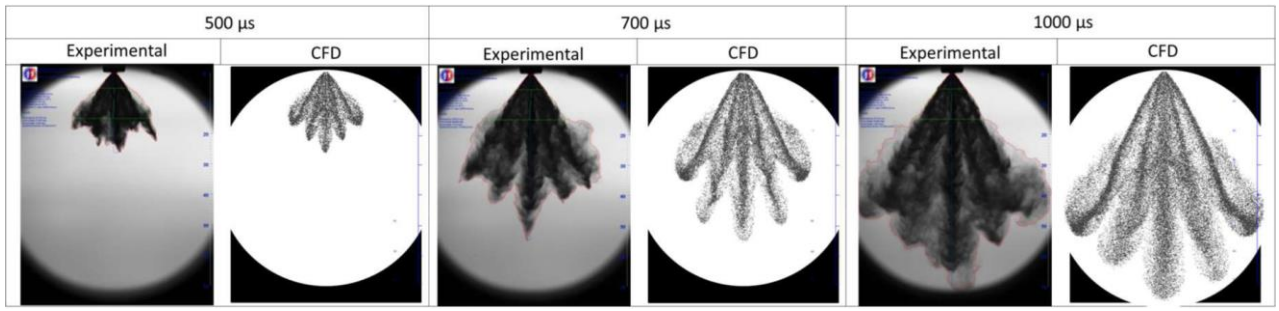

Figure 46. Comparison in terms of imaging between simulations and experiments for the INJ3 at 60 MPa.

As reported from the imaging comparison, the main spray characteristics such as the overall cone angle and relative penetrations between the different plumes are well captured by simulations for all investigated injection pressures.

In the light of the promising results obtained with the INJ3, the same numerical approach is adopted for the Spray G. Before moving to the discussion of the results, it is useful to anticipate at this stage that the adoption of a small initial droplet diameter does not allow to obtain an acceptable numerical representation of the Spray G, if compared to the experimental evidence. For this reason, larger initial diameters are also simulated. A first numerical comparison is proposed in Figure 47, which shows liquid penetrations for the different investigated droplet initial diameters, which is able to affect liquid penetration both at the beginning and at the end of the injection. In particular, if initial diameter decreases, initial liquid penetration decreases as well, due to a lower droplet momentum. Even if it is not so evident because of the reduced injection duration, moving towards the end of the injection, a more complicated trend can be noticed: starting from 110 µm and reducing the droplet diameter, penetration reduces as well. However,

moving from 50 µm to 20 µm liquid length increases. Finally, adopting a diameter of 10 µm leads to a remarkable increase of liquid penetration.

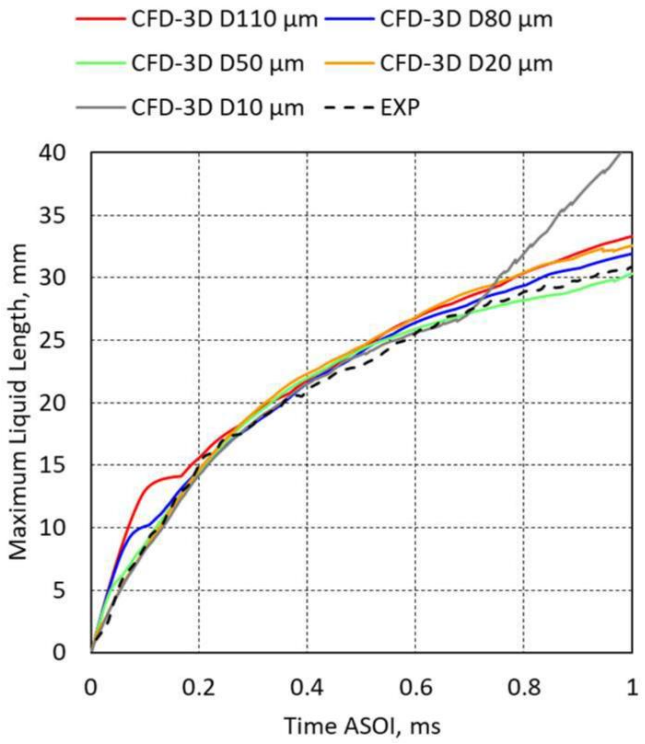

Figure 47. Comparison between experimental liquid penetrations and numerical ones, for each tested initial droplets diameter in the Spray G.

Two observations are necessary: the first one regards the slight over-penetration obtained with the initial diameters of 80 and 110 µm. This may be solved with a dedicated tuning of the secondary break-up. In fact, it is useful to remind that simulations are carried out on equal secondary break-up model, namely the Reitz's one and no specific tuning is carried out in order to focus the attention only to the primary break-up. The second remark deals with the poor results obtained with 10 µm as initial droplet diameter, as anticipated at the beginning of the paragraph. This is inconsistent with expectations as, in the light of previous results on the INJ3, such droplet sizing was considered reasonable. In order to understand the reasons behind such unexpected behaviour, a comparison between numerical snapshots and experimental imaging $0.5 \cdot 10^{-3} s$ after the start of injection is shown in Figure 48. While larger initial droplet diameters lead to a consistent numerical representation of the Spray G, smaller values produce large deviations from the experimental outcomes. Moving from 110 to 10 µm, a collapse of the spray plumes is

increasingly evident. Such phenomenon, clearly visible in the case with droplet initial diameter of 10 µm, is the main responsible for the over-penetration observed before, and it is mainly due to the higher back pressure (0.6 MPa) compared to the INJ3 operating condition (0.1 MPa).

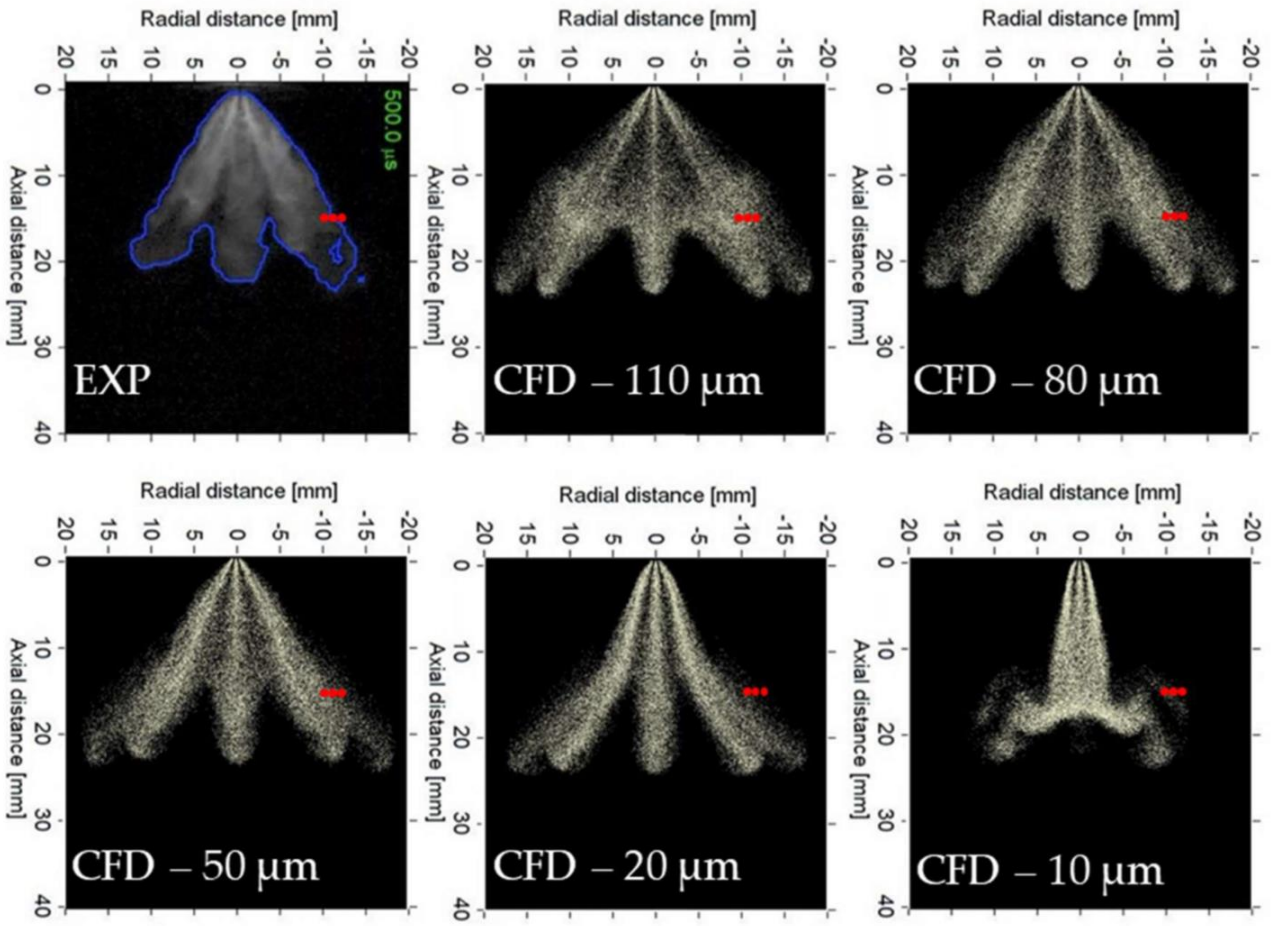

Figure 48. Comparison in terms of imaging between experimental and numerical outcomes for the Spray G. The initial droplet diameters for each numerical simulations are reported in the figures. Red points represent positions where comparisons in terms of PDA data are carried out.

In fact, as visible in Figure 49, with low backpressure (INJ3), the pressure difference between the core of the spray and the outer region is almost negligible; conversely, at higher backpressure (Spray G), the difference is remarkable. Because of the lower pressure in the spray core region, plumes are attracted by each other, and only larger diameters ensure a droplet momentum able to overcome attraction between plumes. For droplet initial diameters higher than 50 µm, numerical spray closely resembles the actual one, even if small differences can be noticed considering the overall cone angle. However, this is mainly due to the fact that numerical

images account for all the droplets, even the smallest ones. On the contrary, the experimental acquisition system is characterized by a mass threshold of 1 %, so the smallest droplets are excluded. It is useful to note that, not by chance, the collapsing tendency of the spray with small initial diameters closely resembles the behaviour of spray under flash-boiling conditions, in which droplets exiting from the nozzle are characterized by diameters much smaller than those under non-flashing conditions [92].

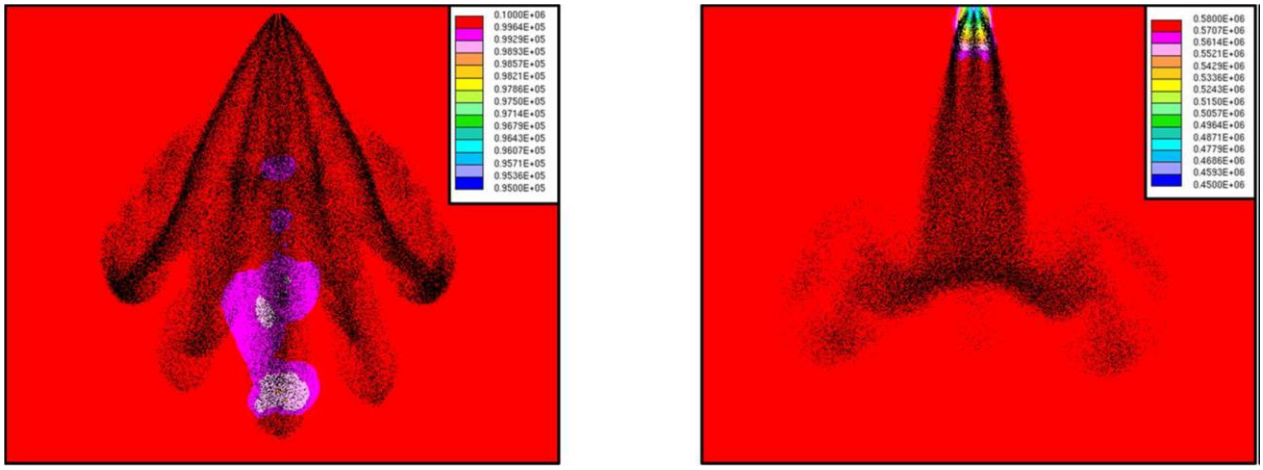

Figure 49. Pressure contours of INJ3 spray (on the left) and Spray G (on the right) at 500 µs after the start of the injection. Pressure is expressed in MPa. The reported sections pass through injector axes.

Even numerical-experimental comparison in terms of droplet sizing (SMD) confirms the importance of larger diameters. For the sake of validity of the experimental data, comparison is carried out only at three locations. Figures 50, 51, and 52 show comparisons on a plane 15 mm far from the injector tip at different radial locations (10,11, and 12 mm). It is worthwhile to specify that numerical SMDs are calculated using the following expression:

$$SMD = \frac{\sum_i COUNT_i \cdot D_i^3}{\sum_i COUNT_i \cdot D_i^2} \tag{93}$$

where D_i is the diameter of the i-th droplet passing through the measurement point during the whole injection process, and $COUNT_i$ is the numerical count of the computational parcel. It is clearly visible that only larger initial droplet diameters allow to match experimental values at

measurement stations. On the contrary, small sizing leads to a not acceptable under-estimation of the experimental data.

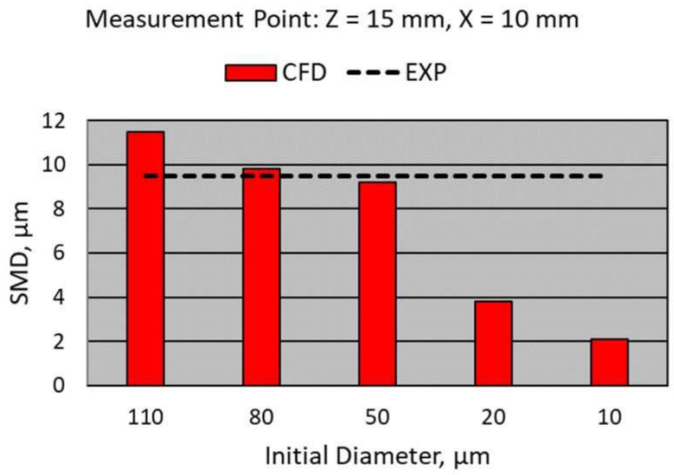

Figure 50. Comparison between numerical and experimental diameters, for different droplet initializations in the Spray G, at an axial distance of 15 mm far from the injector tip and a radial one of 10 mm.

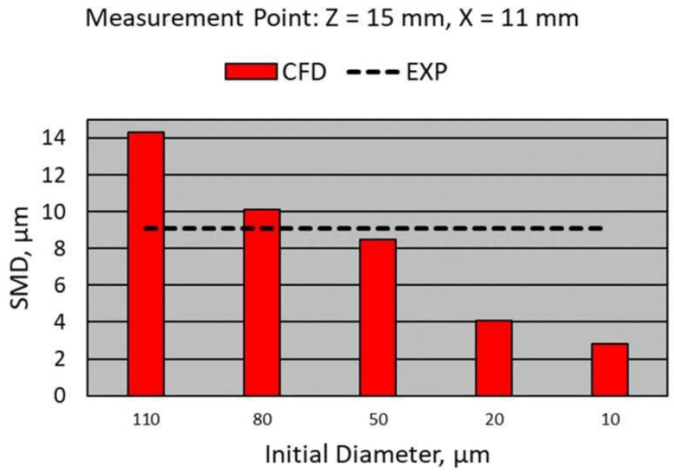

Figure 51. Comparison between numerical and experimental diameters, for different droplet initializations in the Spray G, at an axial distance of 15 mm far from the injector tip and a radial one of 11 mm.

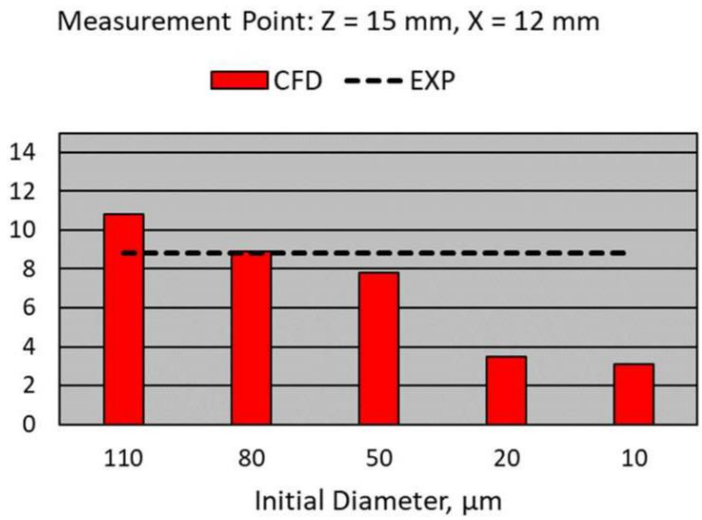

Figure 52. Comparison between numerical and experimental diameters, for different droplet initializations in the Spray G, at an axial distance of 15 mm far from the injector tip and a radial one of 12 mm.

Before moving to the inner-nozzle flow simulation, a few considerations are drawn on the importance of secondary break-up. In fact, the same collapsing effect obtained with reduced initial droplet diameters can be achieved by means of larger diameters along with an enhanced secondary break-up. As an example, initial droplet diameter equal to 80 µm is considered. Secondary break-up model is switched from Reitz's one to KHRT. This latter provides a faster and more effective secondary break-up. Therefore, as shown in Figure 53, plume collapsing and a rapid increase of the liquid length at the end of the injection are noticed, similarly to the previous case with Reitz's model for the secondary break-up and 10 µm as initial droplet diameter. The same can be stated for the SMD: with higher initial diameters but a promoted break-up, numerical droplet sizing under-estimate experimental data, as visible in Figure 54. Therefore, besides a proper atomization of the liquid column (which is the main focus of this study), a reliable secondary break-up model is also mandatory to match experiments. Such topic will be explored in detail in the next chapter.

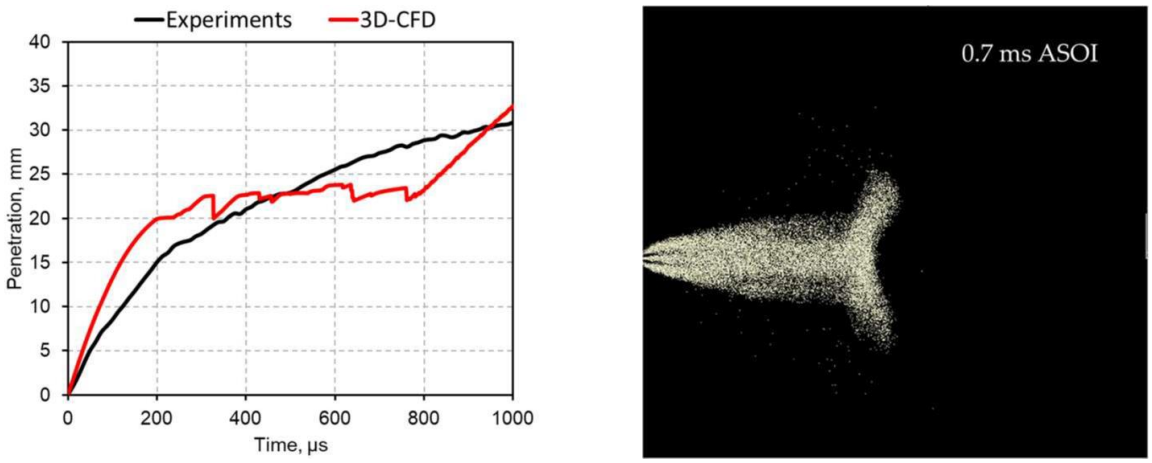

(a) (b)

Figure 53. (a) Comparison between experimental and numericla liquid length using KHRT secondary break-up model in the Spray G. (b) Collapsing numerical spray at 0.7 ms after start of the injection.

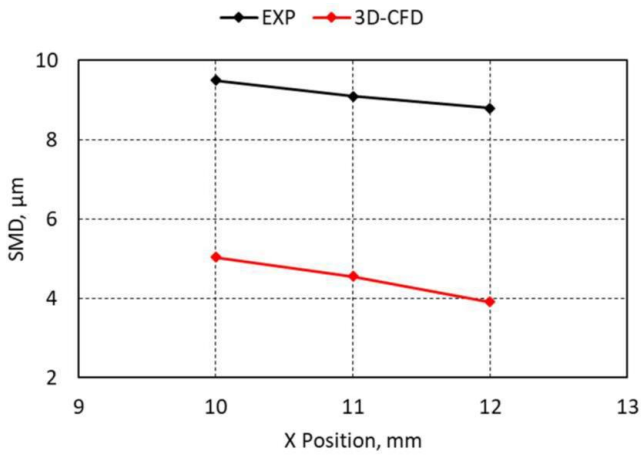

Figure 54. Comparison between numerical and experimental SMD for the Spray G, using KHRT model.

In light of the results shown above, the diffused approach based on the adoption of small diameters to initialize droplets seems to be acceptable (even if wrong) only with reduced backpressures (i.e., nearly equal to ambient pressure), while at higher backpressures such an approach provides numerical results extremely different from experimental outcomes. As a further confirmation of such evidence, an inner-nozzle flow simulation on the Spray G is proposed hereafter, able to provide information about the liquid column exiting from the injector nozzle. It is mandatory to point out that the adoption of droplet diameters comparable to injector holes

cannot be considered as a universal approach. Even if correct for most of the industrial applications (such as gasoline and Diesel injectors under standard internal combustion engine operations), there are some situations in which initial droplet diameters have to be carefully investigated (such as in the case of gasoline injectors under flash boiling conditions). A first comparison between experimental and numerical in-nozzle flow outcomes for the Spray G injector start with the total injected mass flow rate, as reported in Figure 55. Numerical mass flow rate closely reproduces the static value detected in the experiments, i.e., approximately 14 g/s. Moving to the hydraulic coefficients, Figure 56. shows the numerical discharge coefficients of each individual injector hole, and their average its corresponding the experimental value. A similar comparison is proposed also for the area coefficient and the velocity coefficient in Figure 57 and Figure 58, respectively. Thanks to the agreement in terms of global mass flow rate, numerical mean discharge coefficient C_d is significantly close to its experimental counterpart; similar satisfactory results are obtained also for the velocity coefficient C_v, and the area coefficient C_a. Differences between numerical and experimental data are lower than 3 %.

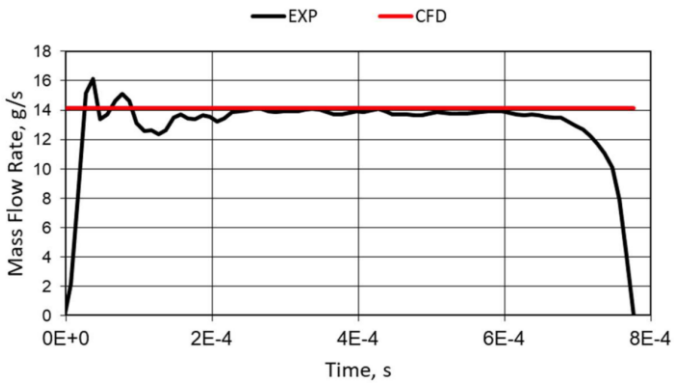

Figure 55. Comparison between experimental mass flow rate and numerical one, derived from in-nozzle flow simulation of Spray G.

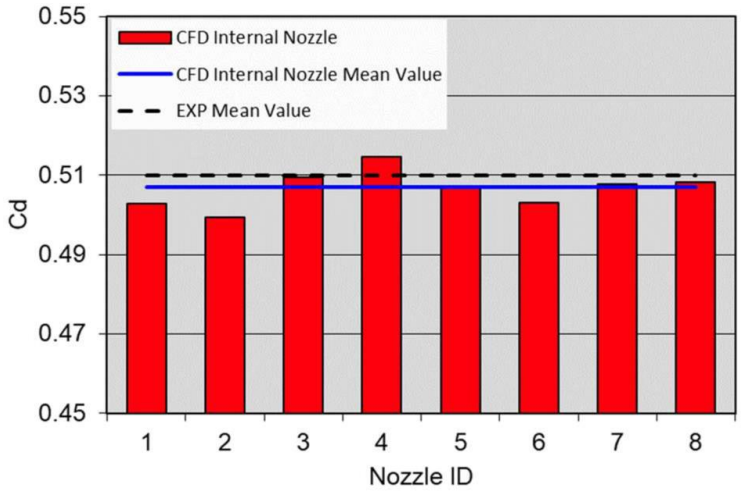

Figure 56. Numerical-experimental comparison in terms of discharge coefficients for the Spray G.

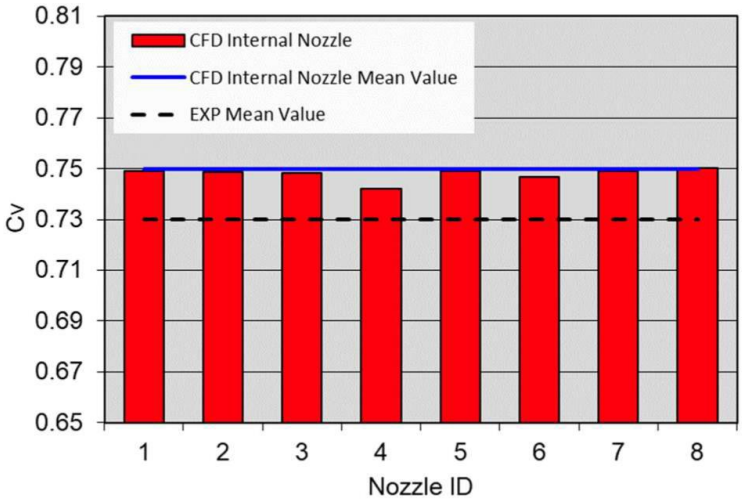

Figure 57. Numerical-experimental comparison in terms of velocity coefficients for the Spray G.

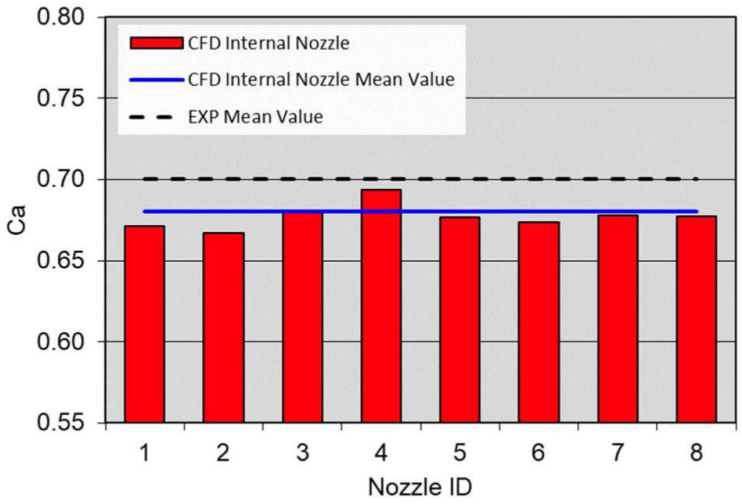

Figure 58. Numerical-experimental comparison in terms of velocity coefficients for the Spray G.

A C_a equal to nearly 0.7 means that part of the section area is not exploited by the flow. Figure 59 confirm this statement since only a portion of the exiting sections is occupied by liquid; similarly, only a portion of the area is characterized by positive axial velocity (i.e., exiting flow), as it is visible in Figure 60.

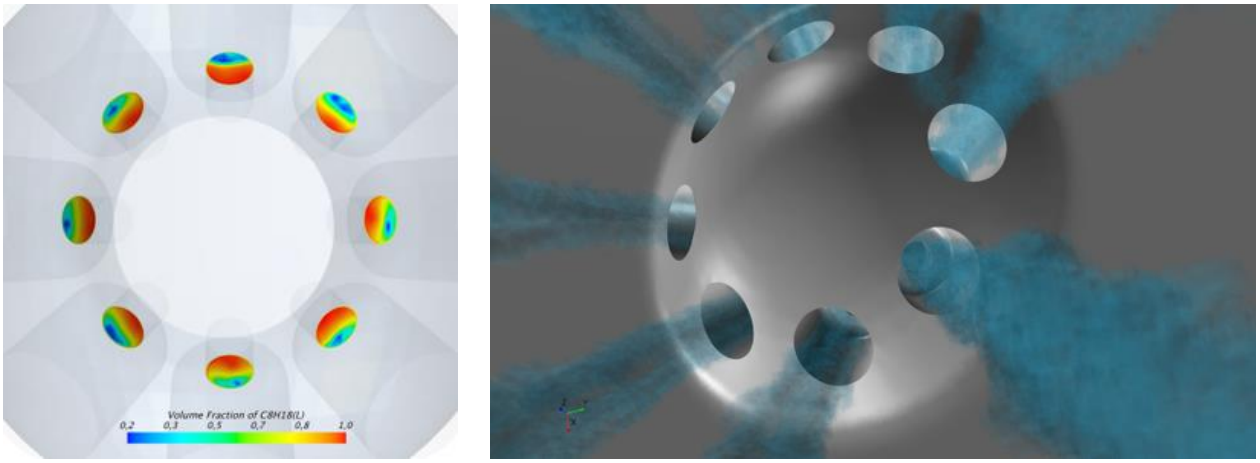

(a) (b)

Figure 59. (a) Liquid volume fraction at the nozzle exit sections for the Spray G. (b) 3D rendering of liquid fraction (i.e. blue visible regions are characterized by the highest liquid volume fraction).

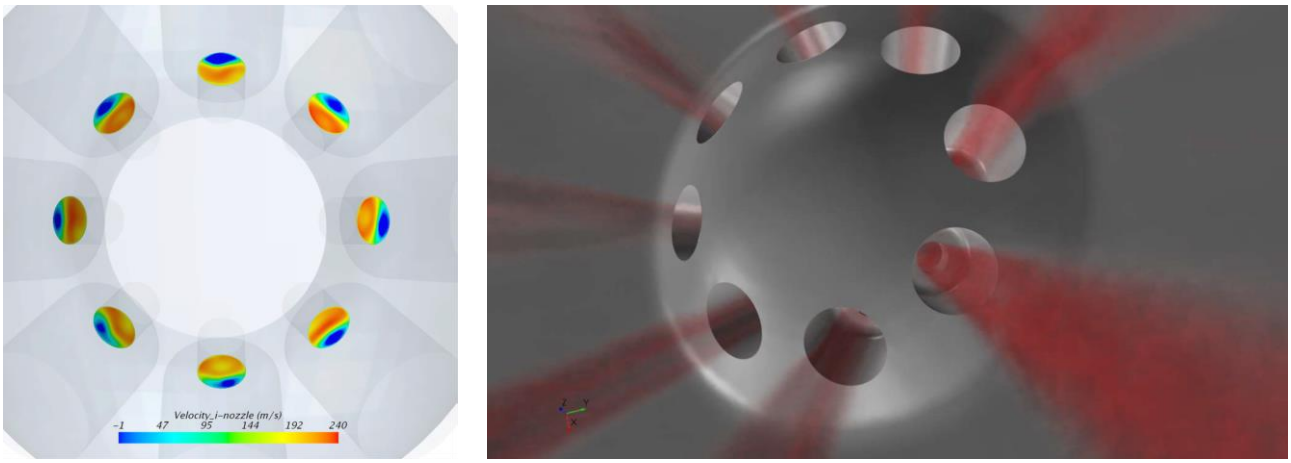

(a) (b)

Figure 60. (a) Local axial velocityat extiting section for each Spray G nozzle hole. (b) 3D rendering of the velocity magnitude (i.e. red visible regions are characterized by the highest velocity magnitude).

In order to validate the calculated plume directions, in Figure 61 experimental plume centroid locations at 50 mm from the injector tip are compared with the projections of the calculated resulting velocity vectors. Experimental data are provided by Delphi [93] on different Spray G injectors (this explains multiple black dots in the graph), while numerical positions are extrapolated using α_x and α_y. Even for such comparison, simulation output properly resembles the experiments.

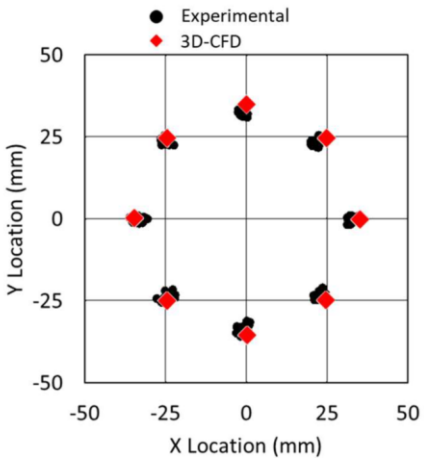

Figure 61. Numerical-experimental comparison in terms of plume centroid location at 50 mm far from the Spray G nozzle.

6. Results – Secondary break-up Analysis

In this chapter, an extensive investigation of secondary break-up modeling in 3D-CFD Lagrangian simulations is presented, for both gasoline and diesel injectors. In particular, the calibration and validation of the new GruMo break-up model is carried out, pointing out the differences with traditional models such as the Reitz Diwakar and KHRT.

6.1 Secondary break-up in Gasoline Injectors

As stated earlier, the set of functions of the GruMo for gasoline injectors is calibrated on the INJ1 for three different operative conditions. Thereafter model validation is carried out on both the INJ2 and INJ3.

At first, Eulerian internal-nozzle simulation results on the INJ1 are proposed for the three different investigated conditions, in order to analyse the effect of ambient pressure variations on the hydraulic coefficients of the injector. Mass flow rate is considered at first. Since the needle opening is not accounted for in the simulation, the initial transient is not included in the comparison and only the time-averaged static mass flow rate is reported. The experimental static value is properly matched by the simulation result, as visible in Figure 62. As for the hydraulic coefficients, a numerical-experimental comparison is reported in Table 9 for the same back pressure.

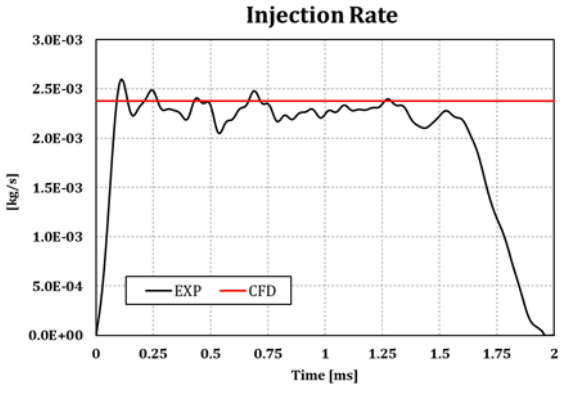

Figure 62. Comparison between experimental and numerical mass flow rates of the INJ1 for a back pressure of 1.0 bar(a) and a difference between rail and ambient of 100 bar.

	p=0.4 bar	p=1.0 bar	p=3.0 bar
C_d EXP	-	0.684	-
C_d 3D-CFD	0.648	0.650	0.655
C_a EXP	-	0.728	-
C_a 3D-CFD	0.727	0.734	0.755
C_v EXP	-	0.940	-
C_v 3D-CFD	0.891	0.886	0.868

Table 9. Experimental and numerical hydraulic coefficients of the INJ1 for the different conditions.

A satisfying agreement can be noticed as the maximum percentage error is lower than 6%. In addition, Table 9 reports the hydraulic coefficients, obtained via the 3D simulations, for the 0.4 and 3 bar cases. It is confirmed that differences in terms of C_d, C_a and C_v are almost negligible between the different conditions. For this reason, the experimental hydraulic coefficients available at 1 bar(a) are adopted for all the investigated conditions of the INJ1, in order to initialize the droplets in the Lagrangian simulations. Similarly, for the INJ2, the experimental hydraulic coefficients available at 1 bar(a) are exploited at the investigated back pressure of 0.4 bar.

Different Lagrangian simulations are carried out on the INJ1 with the aim to evaluate the effect of the ambient density on the proposed GruMo secondary break-up model parameters. In particular, they are purposely calibrated against experimental data for all the operations. It is worth to remember that the drop initialization is the same for all the conditions, as hydraulic coefficients are common. For a fair comparison, droplet initial conditions are kept constant for the different tested secondary break-up models as well. The first comparison between experimental and numerical data is proposed in Figure 63, in terms of liquid penetration length. For all the injectors, spray penetrations are computed as the distance from the tip (along the injector axis) at which 99% of the injected mass is found, according to a widely diffused practice [91]. Moreover, both electric and hydraulic delays are not included in the graphs dealing with the liquid length penetration. In other words, the time-axes begin with the appearance of the first droplets at the nozzle exit and not with the excitation start. Focusing on the INJ1 results, all the investigated secondary break-up models are able to reproduce the experimental liquid penetration curves at both 0.4 and 1.0 bar, while for the 3.0 bar condition, only the GruMo approach properly estimates

the liquid penetration. Conversely, the KHRT and Reitz-Diwakar (R-D) models with default constants underestimate and overestimate, respectively, the experimental findings.

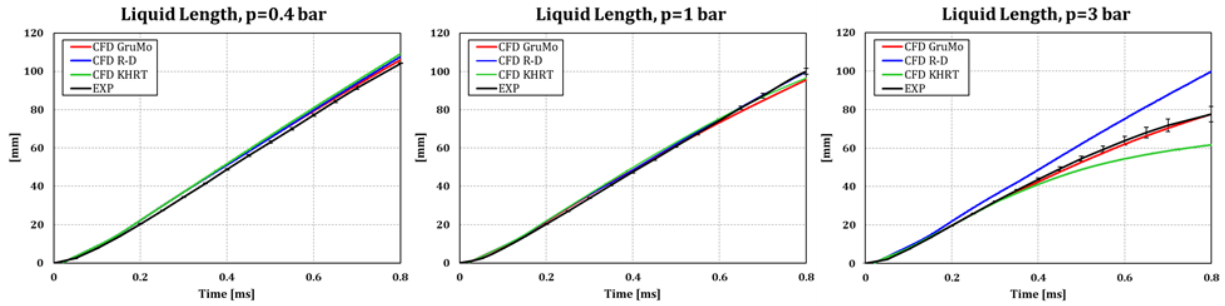

Figure 63. Comparison between numerical and experimental penetrations for the different investigated conditions and break-up models in the INJ1.

In order to evaluate the ability of the break-up model to properly predict the droplet disruption mechanism, a comparison in between PDA data and CFD is proposed in Figures 64, 65, and 66, respectively.

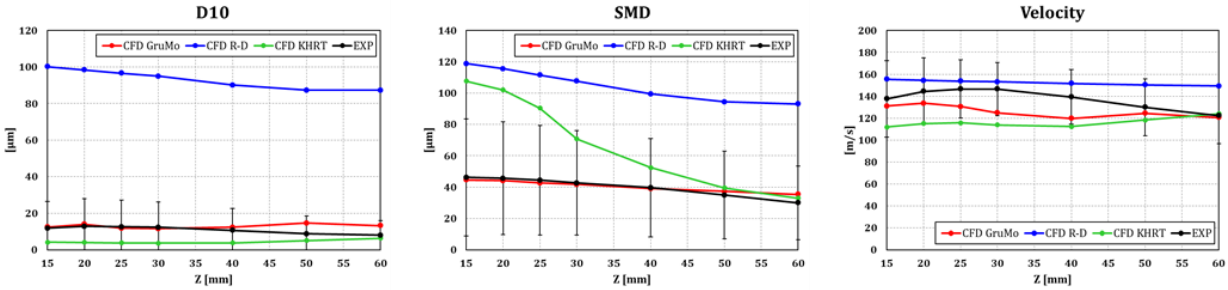

Figure 64. Comparison, between simulations and experiments for the INJ1, in terms of D10, Mean Velocity and Sauter Mean Diameter, at 0.4 bar.

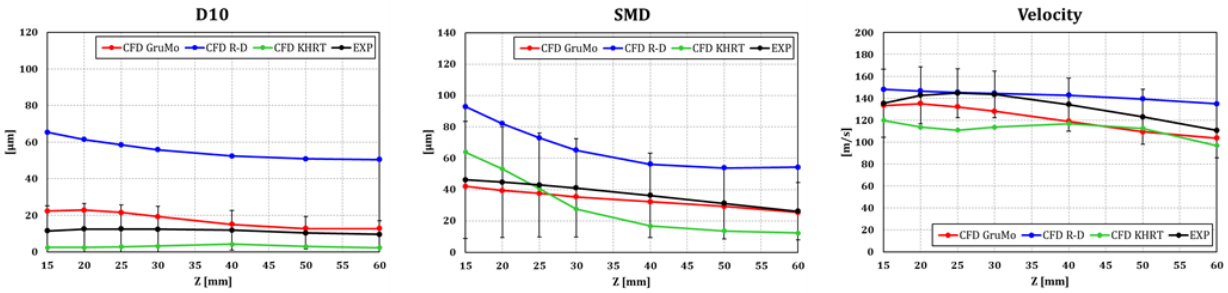

Figure 65. Comparison, between simulations and experiments for the INJ1, in terms of D10, Mean

Velocity and Sauter Mean Diameter, at 1.0 bar.

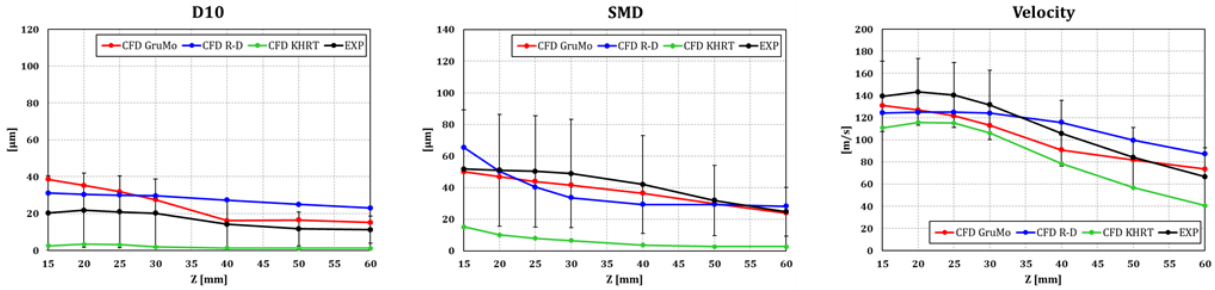

Figure 66. Comparison, between simulations and experiments for the INJ1, in terms of D10, Mean Velocity and Sauter Mean Diameter, at 3.0 bar.

Specifically, arithmetic mean diameter (D10), SMD and mean axial velocity provided by the different break-up models are compared with the experiments. To be consistent with the experimental counterpart, numerical results represent an average over a $2.0 \cdot 10^{-3} s$ window from excitation time (ET) start. PDA analysis confirms the results in terms of liquid penetration previously discussed. In fact, the GruMo model, thanks to a thorough case-by-case calibration work, is able to match droplet size and velocity for all the investigated conditions. For each measurement station, the error is lower than the standard deviation. Conversely, the KHRT and Reitz-Diwakar models show a strong dependency of the numerical results on the ambient pressure. As for the KHRT model, major errors are noticed for the extreme cases. At 0.4 bar, up to 30 mm far from the tip, a non-negligible overestimation of SMD; at 3.0 bar, instead, drop break-up is overestimated starting from the near-nozzle region and SMD is largely under-predicted for all the stations. As for the Reitz-Diwakar model, the only case where results seem to be acceptable is the one with the highest back pressure. For the other conditions, a relevant overestimation of SMD and, mostly, D10 is obtained. Two different conclusions can be drawn from this overview of the results. Firstly, with the exception of the GruMo approach, the tested secondary break-up models are unable to simultaneously provide a reliable estimation of the investigated quantities at all the conditions. In fact, there is no chance to match all the experiments here reported with a unique set of constants. This endorses the choice to replace the model constants with parameters that are functions of the operating conditions. Furthermore, the adoption of a zonal approach easily allows two extremely different rates of break-up to coexist in the domain. Near the tip

break-up is promoted, leading to a rapid decrease of the SMD which is more than halved in between the nozzle and the transition distance. If D10 is considered, the reduction is of one order of magnitude. Conversely, downstream the first measurement station, the droplet disruption rate is noticeably reduced. D10 is almost constant, at least for 0.4 and 1 bar cases, and SMD decreases very slowly. The last comparison between experimental and numerical outcomes for the INJ1 is carried out in terms of imaging in Figures 67, 68, and 69. On the numerical side, as only a quarter of the domain is simulated, the images are reflected to obtain a full representation of the spray. Moreover, since the concept of parcel is exploited in order to drastically reduce the number of droplets to trace, Lagrangian particles are plotted with the same diameter (i.e. there is no parcel-to-parcel difference) in order to obtain a more uniform and realistic representation of the spray. Despite more physical, the adoption of a variable diameter would lead to a very gaunt visualization of the plumes. Light-grey and black colours are assigned to parcels and background respectively, to mimic the front-light illumination of the experimental images. Accordingly to the experiments, only liquid parcels are shown and no information on the fuel vapour is visualized. The proposed GruMo model is the only one able to reliably represent the spray morphology at all the investigated conditions. Only the radial penetration of the droplets at 3 bar(a) seems to be slightly underestimated, and this is due to the experimental spray. In fact, despite it is not visible from the proposed snapshots that come from a unique injection event, the experimental spray is affected by a non-negligible variation of the bend angle during the sequential operation (caused by both the turbulence effect and the needle wobbling motion). Conversely, the numerical snapshots derive from a RANS simulation relying on a fixed plume direction for the droplet initialization. In other words, the simulation aims at reproducing the average behaviour of the spray and not a specific shot. As for the KHRT and Reitz-Diwakar models, deficiencies can be noticed at all the conditions. At 0.4 bar, the spray morphology is not coherent with the experimental counterpart; at 800 μs, the KHRT model predicts a very thin plume tip, while the Reitz-Diwakar one shows an unphysical step between 75 and 90 mm. Increasing the back pressure, the critical issues related to such models are even more evident. In order to obtain the accurate match between numerical and experimental results described above, the GruMo break-up model undergoes case-by-case tuning of the parameters. The values resulting from the thorough calibration process are reported in Figure 70 with respect to the ambient density (ρ_{amb}). C_{b2}, which affects the characteristic time scale of the Bag, is constant for all the operating conditions.

For C_{b1}, C_{s1} and C_{s2} a linear behaviour can be identified. In this regard, trend lines are proposed in the graphs, which are able to accurately represent the tendency of the model parameters.

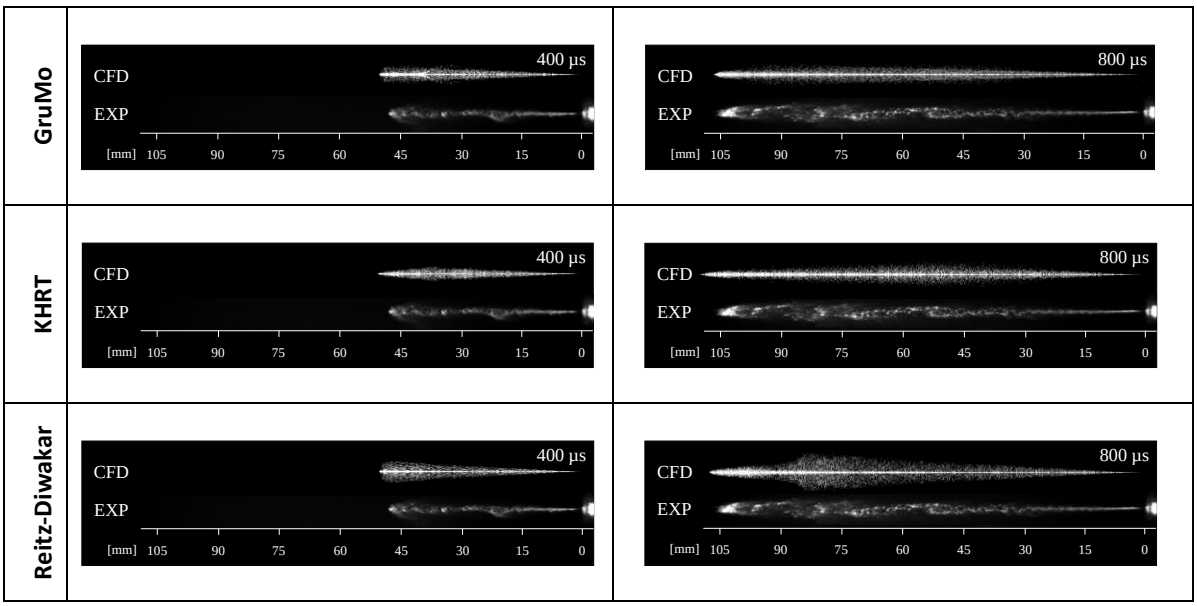

Figure 67. Numerical-experimental comparison, in terms of global spray shape evolution, for a back pressure of 0.4 bar in the INJ1. CFD is reported on the top, while experiment on the bottom.

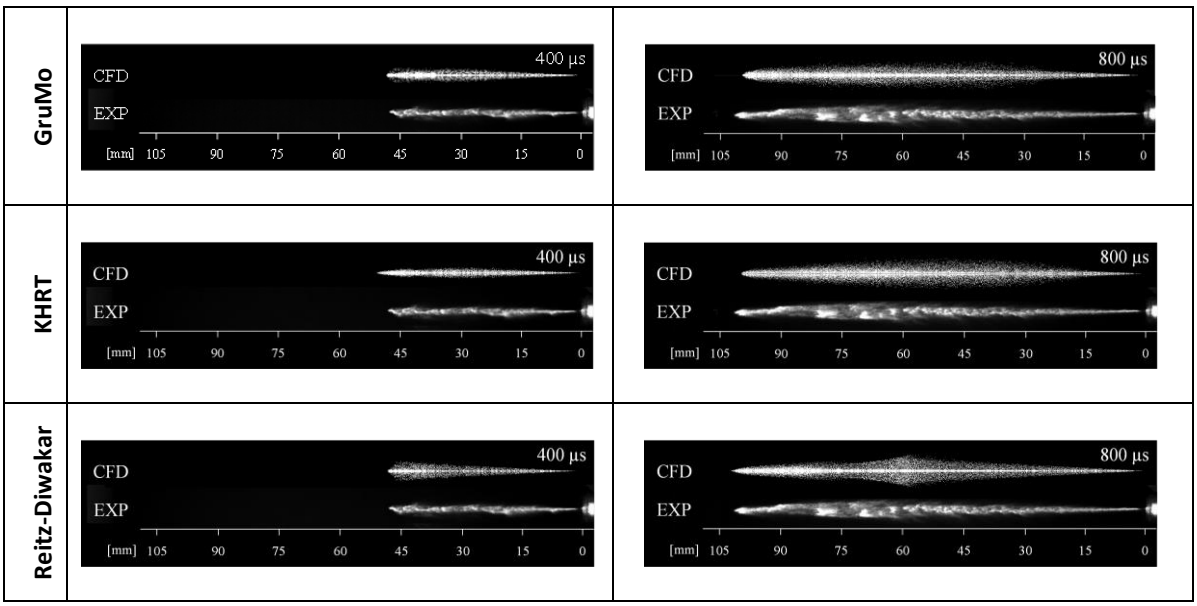

Figure 68. Numerical-experimental comparison, in terms of global spray shape evolution, for a back pressure of 1.0 bar in the INJ1. CFD is reported on the top, while experiment on the bottom.

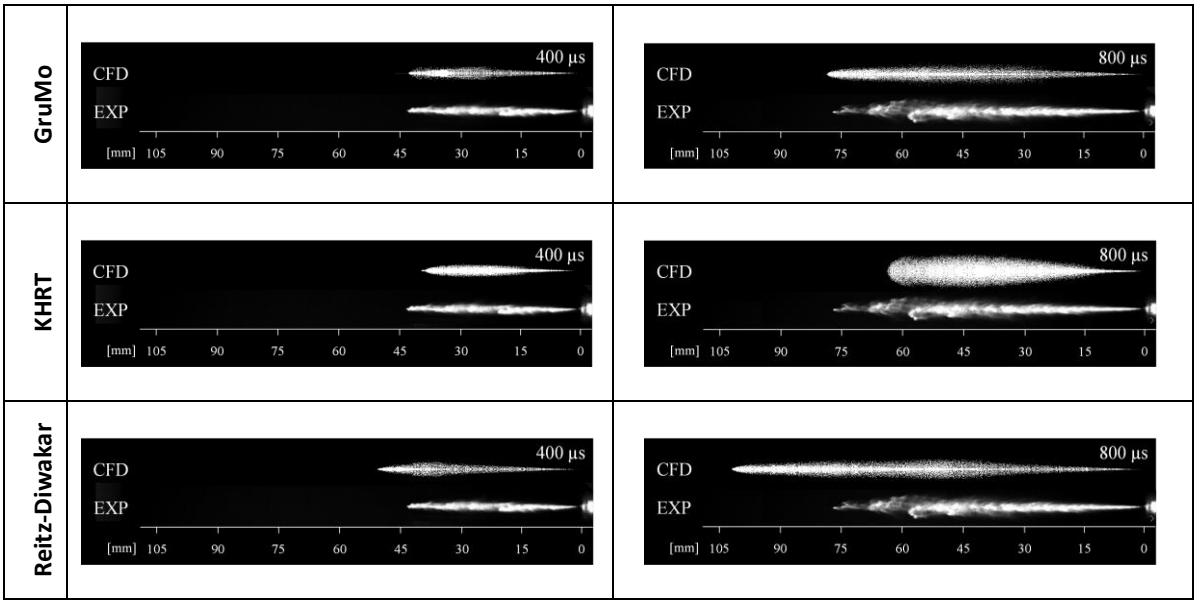

Figure 69. Numerical-experimental comparison, in terms of global spray shape evolution, for a back pressure of 3.0 bar in the INJ1. CFD is reported on the top, while experiment on the bottom.

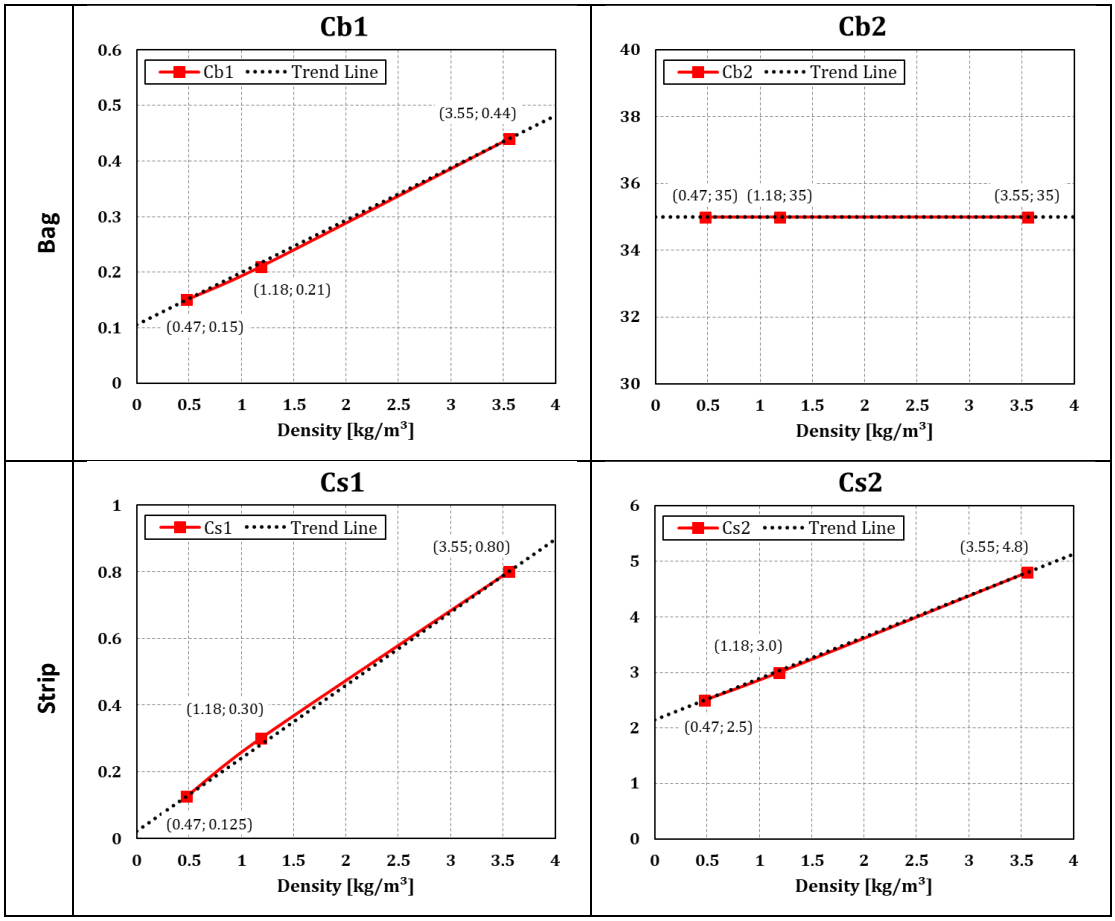

Figure 70. GruMo break-up model parameters as a function of the ambient density – gasoline

injectors.

Expressions of the trend lines are reported in equations (94) to (97). Slope 'm' and y-intercept 'q' are shown in Table 10.

$$C_{b1} = q_{c_{b1}} + m_{c_{b1}}\rho_{amb} \tag{94}$$

$$C_{b2} = q_{c_{b2}} + m_{c_{b2}}\rho_{amb} \tag{95}$$

$$C_{s1} = q_{c_{s1}} + m_{c_{s1}}\rho_{amb} \tag{96}$$

$$C_{s2} = q_{c_{s2}} + m_{c_{s2}}\rho_{amb} \tag{97}$$

$q_{c_{b1}}$	0.105
$m_{c_{b1}}$	0.094
$q_{c_{b2}}$	35.0
$m_{c_{b2}}$	0
$q_{c_{s1}}$	0.021
$m_{c_{s1}}$	0.219
$q_{c_{s2}}$	2.146
$m_{c_{s2}}$	0.747

Table 10. Slope and y-intercept of the GruMo model parameter trend lines.

To critically evaluate the resulting values, a detailed analysis is carried out on the INJ1 spray at the different ambient pressures. Specifically, for all the droplets in the computational domain at $0.5 \cdot 10^{-3} s$ after the injection start, We_g and $We_g/\sqrt{Re_d}$ quantities are investigated since they determine whether Bag and Stripping occur or not, respectively. $0.5 \cdot 10^{-3} s$ pertains to the static phase of the injection event and all the considerations proposed in the following can be approximately extended to the other instants. To gather the huge amount of data related to the presence of a large population of droplets, the Probability Density Function (PDF) and the

Cumulative Distribution Function (CDF) are used. Domain is split in the two zones where the GruMo break-up operates differently, the one between the injector tip and T_d (i.e. $DIST_{inj}$ ≤ 15 mm) and the one further downstream (namely $DIST_{inj}$ > 15 mm). Focusing on the Stripping mechanism, PDF, and CDF of $We_g/\sqrt{Re_d}$ obtained considering the droplets within the first 15 mm are proposed on the left side of Figure 71. In the original Reitz-Diwakar model, C_{s1} is equal to 0.5. However, CDF shows that the adoption of a T_d equal to 15 mm leads, for an ambient pressure equal to 0.4 and 1.0 bar, to a small percentage of droplets satisfying the condition of $We_g/\sqrt{Re_d}$ > 0.5, needed for Stripping to take place. For example, at 0.4 bar, less than 30% of the droplets (those closer to the injector tip where relative velocity and diameter are higher) would satisfy the requirement. For the remaining droplets, break-up would be frozen up to the Bag region. From a practical perspective, this means that there would not be chance for numerical results to reliably match experimental PDA data. For this reason, C_{s1} is set to 0.125 and 0.3 for 0.4 and 1 bar(a) cases, respectively. It is important to highlight that, among the possible combinations that allow a reasonable agreement with the experiments at 15 mm, the selected values of C_{s1} are the highest ones. In other words, parameters are kept as closed as possible to the original Reitz-Diwakar model constants. As for the highest back pressure, despite a value equal to 0.5 can be used according to the original Reitz-Diwakar model (as it would be sufficiently low to ensure Stripping for more than 80% of the droplets), C_{s1} is set to 0.8. The latter is preferred since it allows to obtain explicitly linear trends; if 0.5 was selected, a C_{s2} value coherent with the latter (thus different from the one proposed in present analysis) should be selected. As for the calibrated C_{s2} values, they allow a gradual break-up within T_d and they are coherent with those provided by Reitz and Diwakar in [18], [54], which range from 0.5 up to 20. Moving to the Bag mechanism, PDF, and CDF of We_g considering the droplets in the outer region are proposed on the right of Figure 71. In the original Reitz-Diwakar model, C_{b1} is equal to 6; even in this case, PDF and CDF suggest that, using such value, break-up would occur only for a small percentage of droplets, even for the 3.0 bar case, in which the higher ambient density provides larger We_g numbers. As depicted in the Figure 71, at 3 bar, disruption would be prevented for more than 50% of the injected droplets, with a consequent overestimation of the droplet size. For this reason, in the GruMo model, C_{b1} value is set equal to 0.15, 0.21 and 0.44 for 0.4, 1.0 and 3.0 bar(a) cases, respectively. Following the same principle adopted for the Stripping, i.e. to limit the differences compared to the original Reitz-Diwakar model constants, C_{b1} values are chosen as high as possible. As for C_{b2}, similarly to the Reitz-Diwakar model, it is kept constant but its value is here one order of magnitude higher than

the original one. This is necessary to compensate the reduction (still of nearly one order of magnitude) of C_{b1} compared to the reference model. In fact, the break-up rate is affected by both the stable diameter and the characteristic time. Since $D_{d,stable}$ is remarkably reduced to allow the Bag break-up to take place for the majority of the droplets, τ_b has to augment to avoid an abnormal increase of the break-up rate.

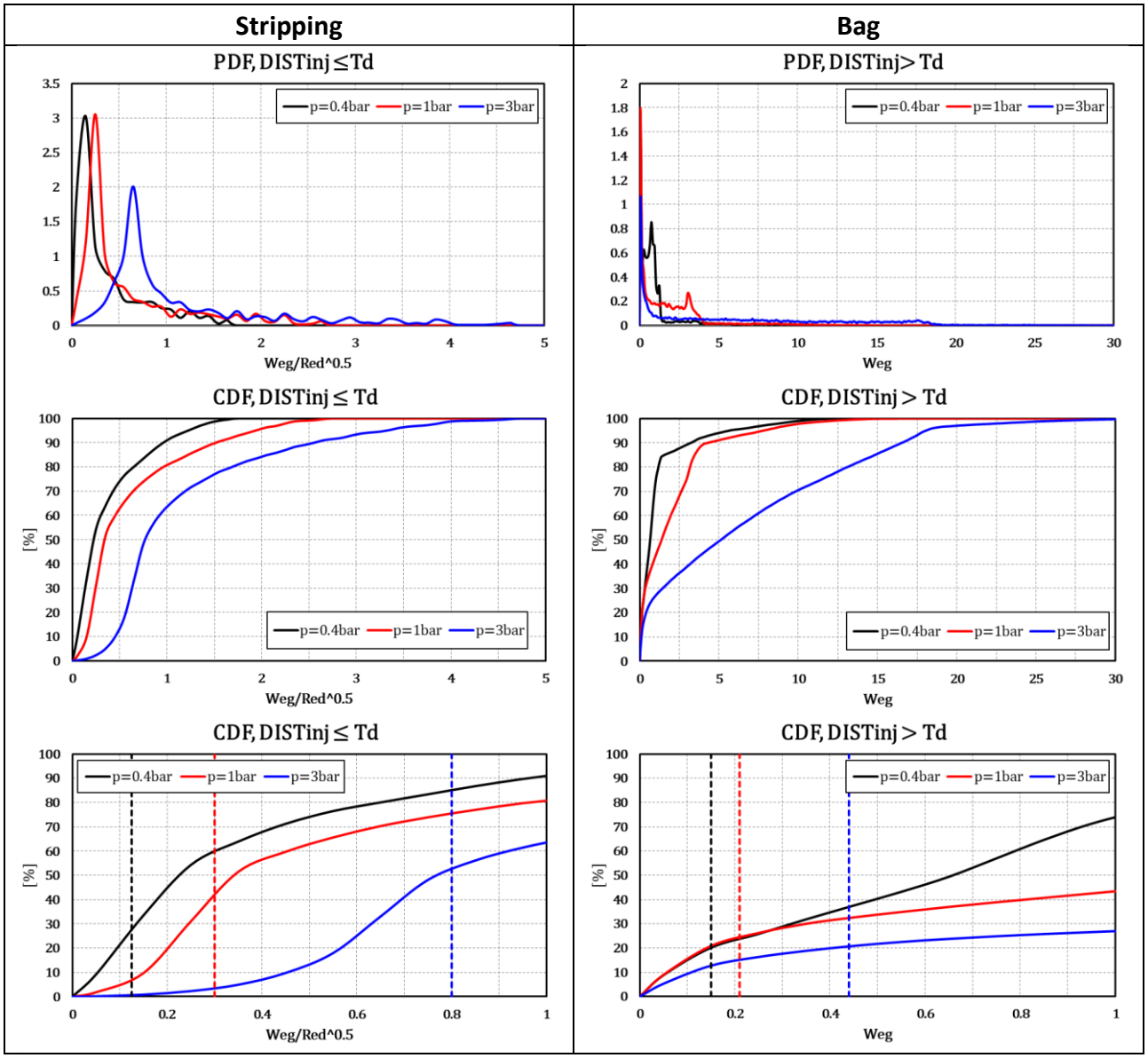

Figure 71. On the left, PDF, and CDF functions of $We_g/\sqrt{Re_d}$ for the Stripping. On the right, PDF and CDF functions of We_g for the Bag. On the bottom, details of the CDFs are reported, and the dashed lines show the adopted values for C_{s1} and C_{b1}.

It is useful to point out that the calibrated parameter values are tightly related to the adopted T_d, mostly for the Stripping. For example, at 0.4 bar, the adoption of a transition distance equal to 15 mm forces C_{s1} to assume a reduced value to make the Stripping effective on the majority of the droplets. The adoption of a remarkably lower T_d would increase the percentage of droplets able to undergo Stripping break-up with the original Reitz-Diwakar model constant, i.e. without decreasing the latter as in the present work. Therefore, despite the Stripping constants assume different values compared to the Reitz-Diwakar model, the main reason is related to the adopted T_d value. As for the Bag, despite the transition distance can still have an impact on the model parameters, the low values assumed by C_{b1} seem to be hardly explainable with the influence of T_d alone. In fact they are much lower than 6, which is typically assumed as critical Weber number, as widely discussed by Wierzba [75]. A possible explanation may be the need to compensate, in the GruMo model, the lack of a further break-up regime for very low We numbers, such as the Vibrational one [60], by extending the operating range of the Bag. In defence of the proposed approach, it is important to point out that the original Reitz-Diwakar model requires a similar decrement of C_{b1}, to provide a proper estimation of the droplet diameters at low ambient density conditions. Focusing the attention on T_d, from a physical standpoint, the validity of the selected value (namely 15 mm) cannot be straightforwardly assessed. Firstly, it is affected by the values of the model parameter; in fact, there is a mutual influence between parameters and T_d. In the proposed approach, model parameters are purposely calibrated to accomplish that Stripping occurs within the first 15 mm, i.e. to ensure that the latter represents a meaningful distance. Neglecting the effect of the calibrated parameters and referring, for a while, to the original Reitz-Diwakar model constants, the adopted T_d seems to be a compromise between the different analysed conditions. At 0.4 and 1 bar droplet We_g is limited, thus Stripping only occurs close to the injector tip and T_d equal to 15 mm results overestimated. Conversely, at 3.0 bar, the transition distance may be considered as under-predicted. Most of the droplets (nearly 90%) satisfies $We_g/\sqrt{Re_d} > 0.5$ condition, thus transition threshold may be shifted downstream. However, it is useful to remember that, mostly at low back pressure conditions, the Reitz-Diwakar model constants are not able to provide a reliable estimation of the droplet diameters. Thus, the evaluation of T_d based on $We_g/\sqrt{Re_d} > 0.5$ criterion may be critical. Even considering a recalibration of the Reitz-Diwakar model constants, at low back pressure conditions the Stripping would mainly occur close to the tip, while for the highest value of p_{amb} the same break-up mechanism would remain the governing one further downstream. In this scenario, 15 mm would

still represent (at least in terms of order of magnitude) a reasonable compromise to identify a region where Stripping may occur. Regardless the choice of the specific value for the parameter, there are at least two noteworthy aspects. Firstly, even if the adopted T_d represents a reasonable length to define a region where Stripping break-up may take place, a second check on the characteristic time of break-up is usually carried out in most of the models, such as the original Reitz-Diwakar. Once the conditions in terms of stable diameters are met for all the break-up mechanisms, a competition between $\tau_{Stripping}$ and τ_{Bag} is reasonably considered to determine the active one. Therefore, despite most of the droplets within 15 mm from the injector tip fulfil the condition $We_g/\sqrt{Re_d} > C_{s1}$, this does not automatically mean that Stripping takes place. Secondly, a distinction between two regions along the injector axis is not sufficient. In fact, relevant differences can be noticed along a traverse orthogonal to the axis as well. In the light of this, in practice, a rigid distance-based classification in two zones is unlikely. Despite being motivated by physics-based considerations (i.e. it represents a reasonable distance, as previously discussed), T_d is a purely numerical artefact to simplify calibration and to easily obtain correlation between model parameters and operating conditions.

The first validation of the GruMo break-up model is carried out on the INJ2. In order to emphasize the improvement achieved with the proposed approach, simulation outcomes obtained with the Reitz-Diwakar and KHRT models are presented as well. Similarly to the INJ1, droplet initial conditions are kept constant for the different secondary break-up models. At first, liquid penetration is compared in Figure 72. GruMo break-up model accurately reproduces the experimental curve, during the whole injection event. As for the KHRT model, a slight underestimation is noticed while the Reitz-Diwakar one significantly over-predicts the experimental data.

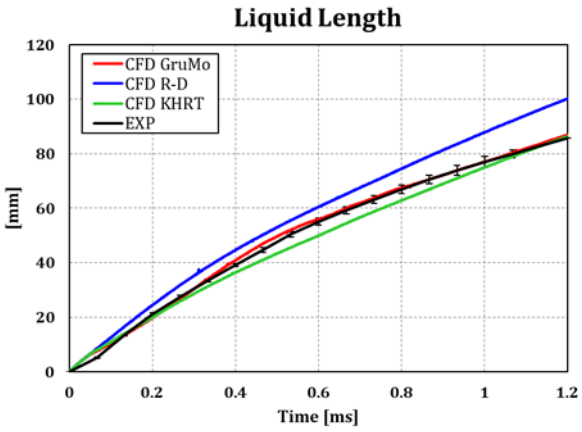

Figure 72. Comparison between numerical and experimental liquid penetrations for the INJ2.

An extended PDA data comparison is proposed in Figure 73. Both the GruMo and the KHRT reasonably match the experimental outcomes. While the former provides a more accurate representation of both droplet diameters and velocities, the latter shows a more pronounced underestimation of SMD downstream the nozzle. These results are coherent with the liquid penetration curves discussed before. Deficiencies shared by all the numerical outcomes deal with the velocity distributions along the y-scan both at 30 and 50 mm. Regardless the break-up model, simulations provide narrower profiles, i.e. droplet velocity rapidly decreases moving away from the plume axis. Conversely, experimental values are characterized by flattened profiles with high droplet velocities even in the periphery of the jet.

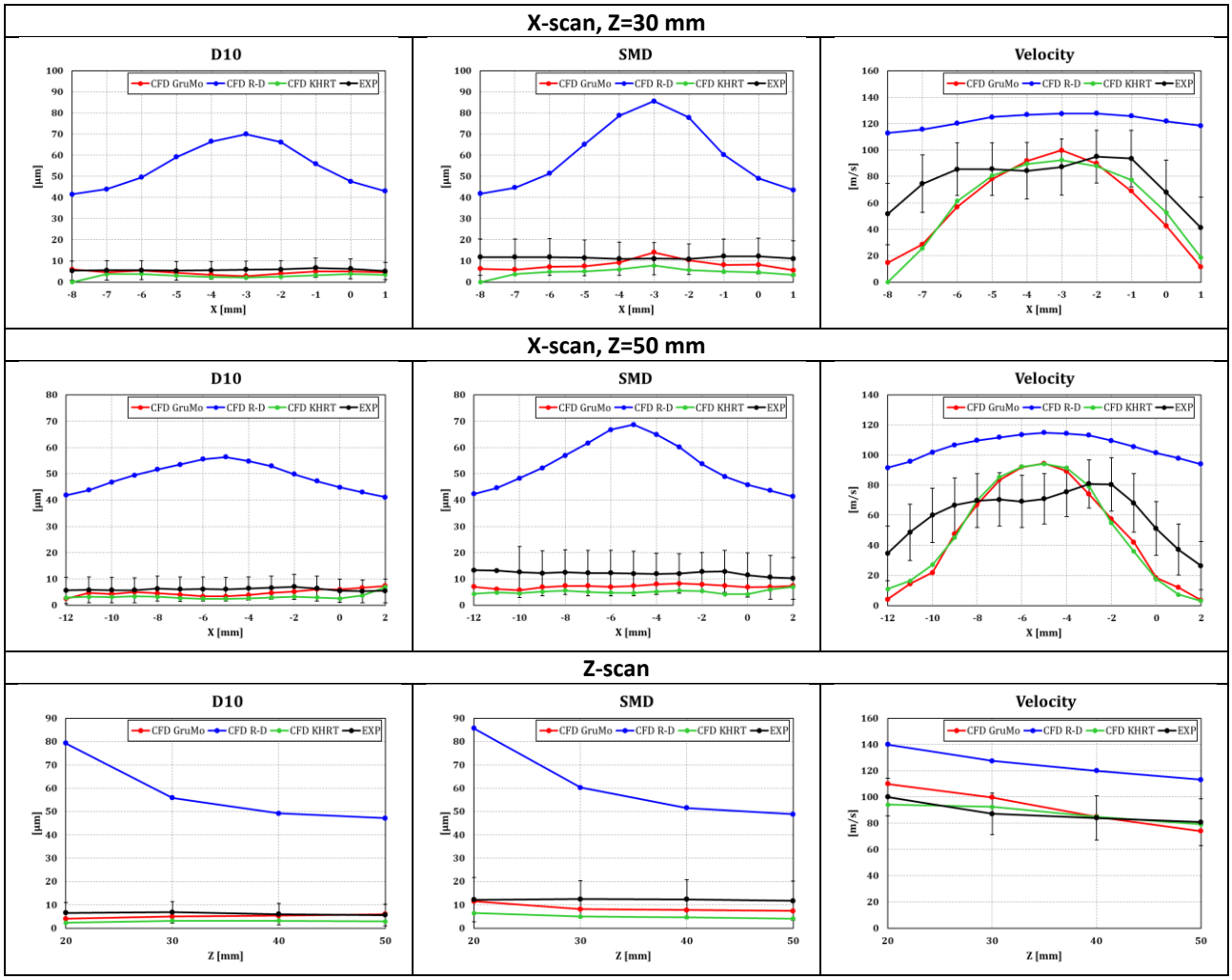

Figure 73. Comparison, in terms of PDA data, between numerical and experimental outcomes at different locations for the INJ2.

Similarly to the INJ1, the reason is related to the non-negligible shot-to-shot variability of the spray bend angle, affecting PDA data through the averaging over 300 shots. Therefore, experimental droplet diameter and velocity distributions along x-scans result to be somewhat uniform. This behaviour (mostly in terms of velocity) is hard to reproduce in CFD, unless several simulations with a different bend angle are run and then, results are averaged. Observing the Reitz-Diwakar model results, a remarkable overestimation of the experimental values can be noticed, in terms of both size and velocity of the droplets. The final comparison for the INJ2 is carried out in terms of imaging. Since the experimental procedure is common, the same criteria adopted for the INJ1 are exploited to produce the numerical images of the INJ2. Moreover, as even in this case only half of the domain is simulated, images are reflected to obtain a representation of the whole spray as depicted in Figure 74. Spray morphology predicted by GruMo model is the one which better

resembles the experimental counterpart. The KHRT slightly under-predicts the radial penetration of the droplets, because of the overestimation of the break-up. As for the Reitz-Diwakar model, imaging shows the limits of using this model with default constants. Since the droplet disruption is largely underestimated, resistance generated by the gaseous phase is lower than expected. In fact, drag force depends on the cross-sectional area of the droplets, i.e. on the diameter. The faster the break-up is, the larger the number of droplets (with smaller diameter) becomes. This increases the total cross-sectional area of the droplets and, thus, the drag force. In this specific case, the latter is under-predicted by the Reitz-Diwakar model because of the slower break-up imposed by its constants. As a consequence, spray results in the "curtain" shape shown in Figure 74, which visibly differs compared to the experimental one.

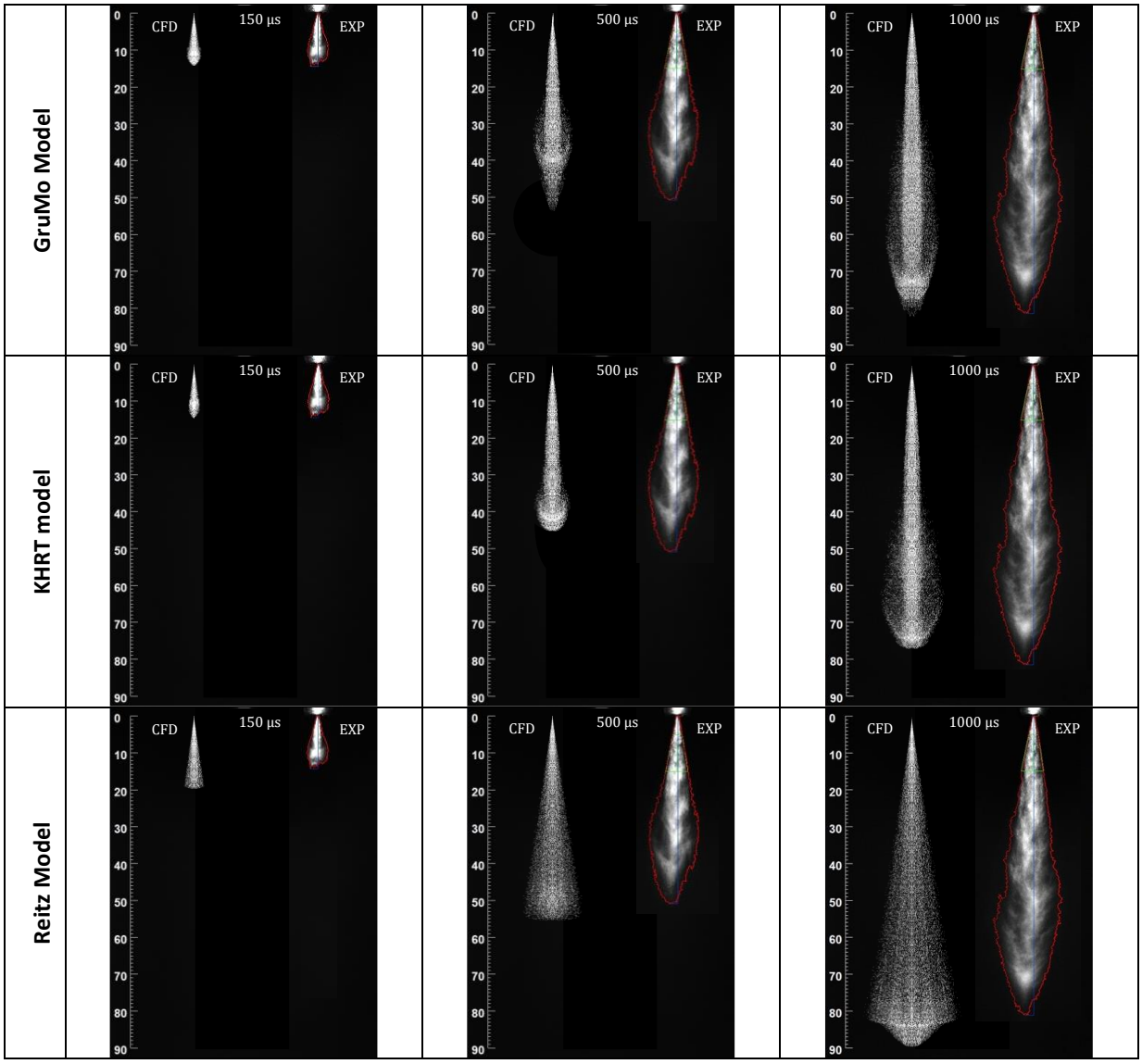

Figure 74. Comparison in terms of imaging between simulations and experiments, for all the investigated break-up models in the INJ2. Snapshots refer to the front view (y-z plane).

Moving on the INJ3, it allows to evaluate GruMo break-model at a different ambient density compared to the INJ2. In addition, it is a multi-hole nozzle, which is a further significant difference with respect to the previous analysed injectors. Once again, both the KHRT and Reitz-Diwakar models are added for the sake of comparison and droplet initialization is kept constant for the different secondary break-up approaches. Similarly to the previous nozzle, results are evaluated in terms of liquid penetration, PDA, and imaging. As for the first, Figure 75 shows that GruMo model accurately reproduces the experimental curve. Conversely, the latter is overestimated by the Reitz-Diwakar model and underestimated by the KHRT one, respectively.

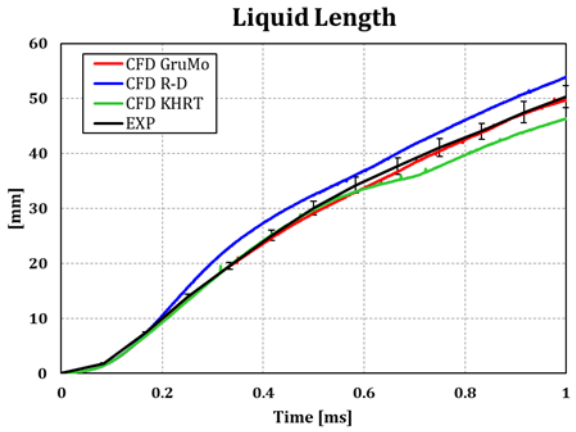

Figure 75. Comparison between experimental and numerical liquid penetration for the different break-up models for the INJ3.

Moving to PDA measurements, quality of the numerical results is evaluated in Figure 76. Overall, GruMo break-up model provides a reliable estimation of both diameters and velocities at all the investigated positions. However, for scans at 50 mm, despite D10 is properly matched, SMD is slightly underestimated by the proposed approach. This is related to the large standard deviation of the experimental data, which implies non-negligible differences between the different droplet diameters. This leads to an increase of SMD values, while limiting D10. On the CFD side, standard deviation is much lower as confirmed by comparing D10 and SMD, which are characterized by almost the same values. As for the Reitz-Diwakar and KHRT models, results are similar to the ones obtained for the INJ2. The former remarkably underrates the break-up process, providing diameters and velocities well above the experimental targets. The latter properly estimates droplet velocities, while D10 and, mostly, SMD are underestimated. Finally, capabilities of the proposed break-up model are investigated by means of a comparison between experimental and numerical spray snapshots, as reported in Figure 77.

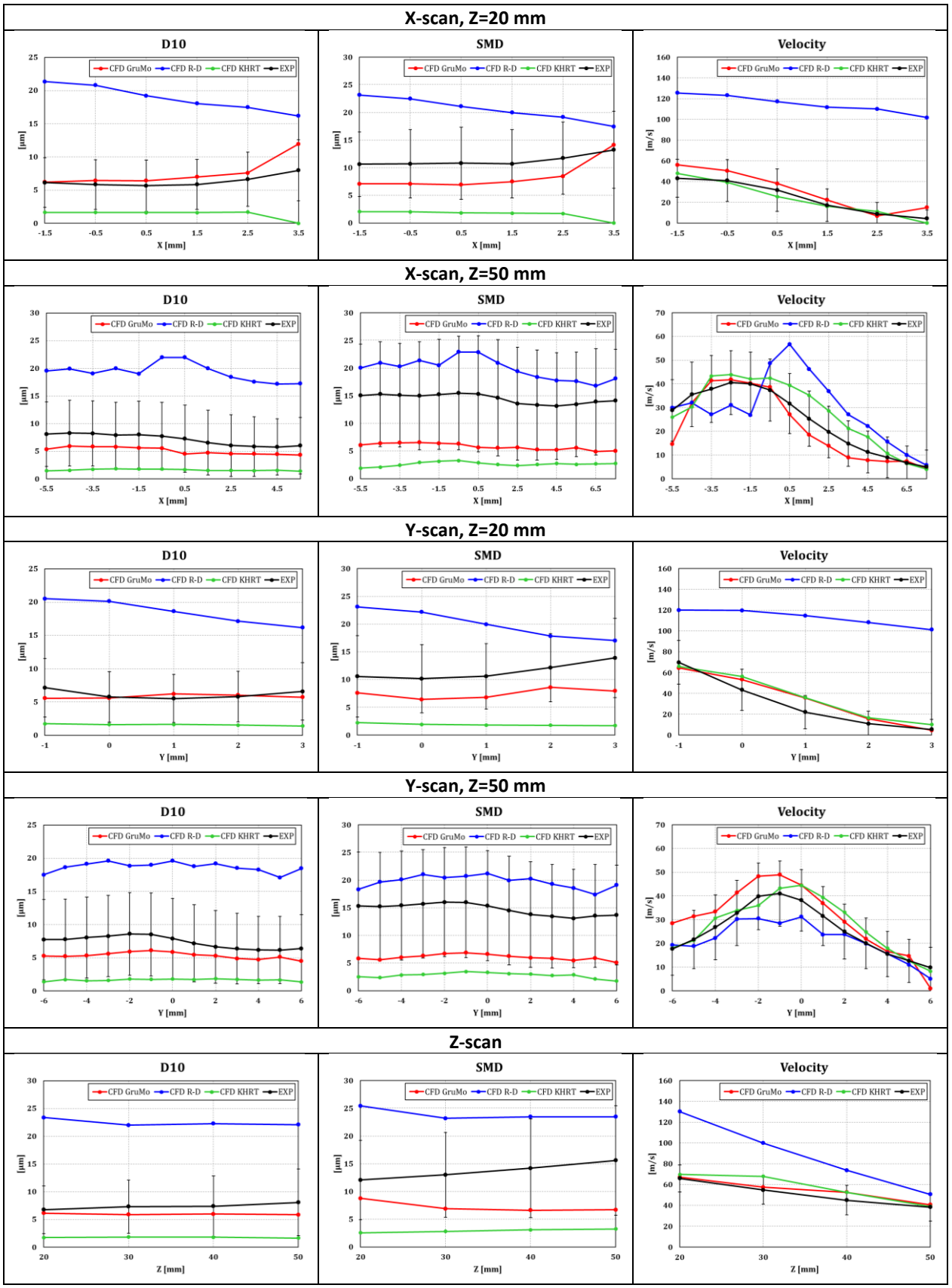

Figure 76. Comparison, in terms of PDA data, between numerical and experimental outcomes at different locations for the INJ3 with different secondary break-up models.

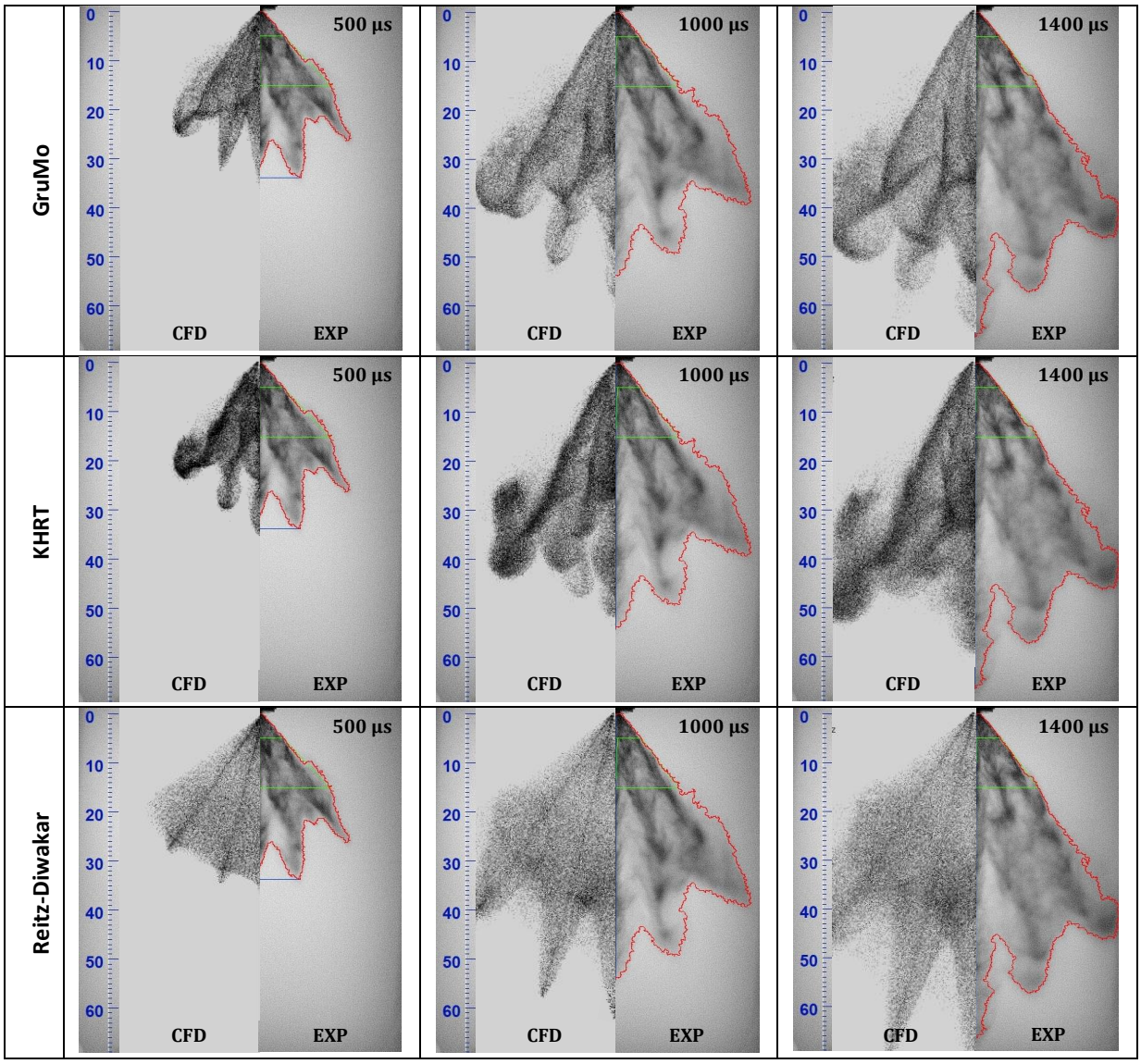

Figure 77. Comparison in terms of imaging between simulations and experiments, for all the investigated break-up models in the INJ3. Snapshots refer to the front view (y-z plane).

Even in this case, the same criteria adopted for the previous injectors are exploited to generate the numerical images. However, compared to INJ1 and INJ2, parcels and background colours are modified to reproduce the effect of the back-light illumination of the experimental apparatus. Spray morphology resulting from the GruMo break-up model is close to the experimental one. Break-up overestimation provided by the KHRT model is visible in the plume directions. While in the experiments they keep straight, in CFD they tend to collapse because of the strong momentum reduction. Conversely, the Reitz-Diwakar model underrates the break-up process, leading to the characteristic "curtain" shape already observed for the INJ2 and to a spray penetration overestimation.

6.2 Secondary break-up in Diesel Injectors

At first, Spray A, Spray C and Spray D, are investigated at the same operating condition, characterized by an ambient density equal to 22.8 kg/m^3 (standard condition), with both GruMo and Reitz model. For the first, model constants are calibrated on the Spray A and are equal to C_{b1}= 1.5, C_{b2} = 0.8, C_{s1} = 0.5 and C_{s2}= 17.5. Lagrangian simulations for all the injectors are validated against experimental data in terms of liquid and vapour penetration curves and imaging. Liquid penetration is evaluated as the distance from the tip, along the injector axis, at which the 99% of the injected mass is found [91]. Similarly, vapour penetration is evaluated as the furthest distance at which a vapour concentration of 0.1% is found. As for the Spray A, a first comparison between experimental and numerical data is carried out in terms of liquid and vapour penetrations, as reported in Figure 78, GruMo break-up model provides a good representation of the liquid penetration curve in both ballistic and steady stages of the injection, while a slight underestimation of the vapour penetration is noticed. The main reason of such under-prediction will be investigated with further sensitivities to different simulation parameters. On the other hand, Reitz-Diwakar break-up model produces liquid and jet penetrations lower than the experimental counterparts, due to the higher break-up rate.

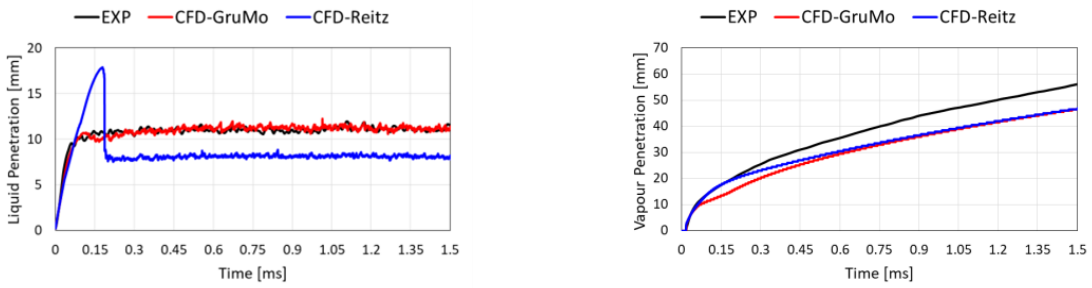

(a) (b)

Figure 78. Comparison between experimental and numerical data in terms of liquid penetration (a) and vapour penetration (b), for the Spray A operating with an ambient density equal to 22.8 kg/m^3.

The results are confirmed comparing numerical and experimental outcomes in terms of imaging. Liquid is reported in Figure 79, while vapour in Figure 80.

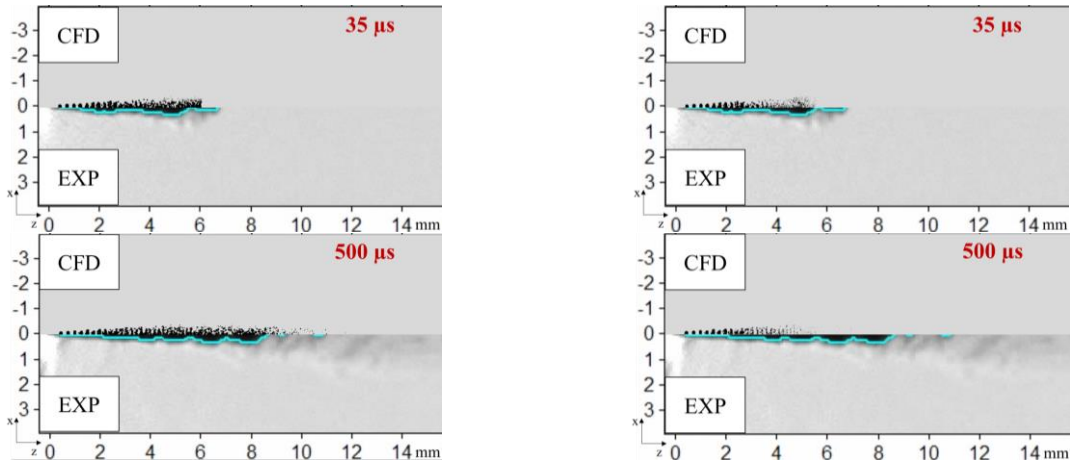

(a) (b)

Figure 79. Comparison in terms of liquid phase snapshots using (a) the GruMo model, and (b) the Reitz-Diwakar one, for the Spray A operating with an ambient density equal to 22.8 kg/m^3.

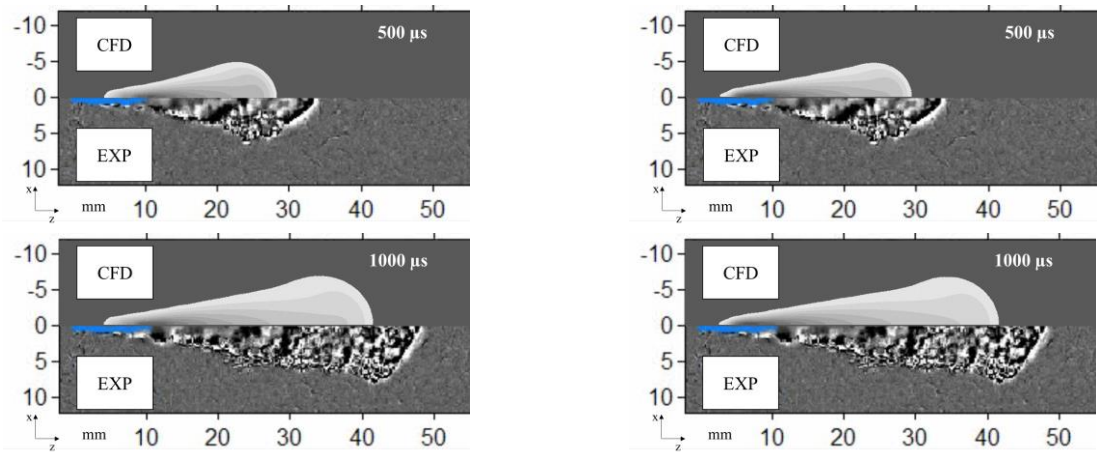

(a) (b)

Figure 80. Comparison in terms of vapor phase snapshots using (a) the GruMo model and (b) the Reitz-Diwakar one, for the Spray A operating with an ambient density equal to 22.8 kg/m^3.

In the light of the promising results for the Spray A, the GruMo model is applied to both spray C and Spray D. Liquid and vapour penetration comparisons for both the injectors are reported in Figure 81.

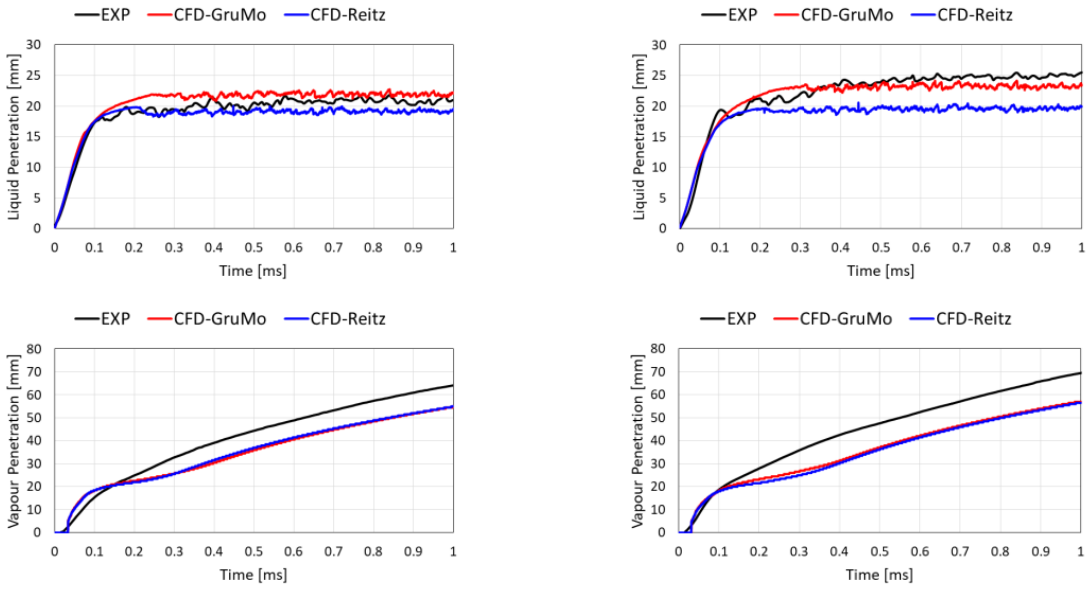

(a) (b)

Figure 81. Comparison between numerical outcomes and experimental results in terms of liquid (up) and vapour (down) penetrations, for Spray C (a) and Spray D (b).

Simulations with the GruMo model show a good agreement between the numerical and experimental liquid penetration curves. It is interesting to notice that the numerical liquid penetration of the Spray D is higher than the Spray C one, as indicated by the experiments. On the contrary, simulations with the Reitz-Diwakar model are characterized by an underestimation of the liquid penetration for both injectors and a negligible difference between the two numerical curves can be noticed. As for the vapour penetration, both GruMo and Reitz-Diwakar models provide an underestimation of the experimental curves of Spray C and Spray D. Numerical and experimental snapshots of the vapour jets are reported in Figure 82, for both the sprays. As for the liquid, no experimental image is available. The comparison proposed in Figure 82 visually confirms the results proposed in Figure 81 in terms of vapour penetration curves.

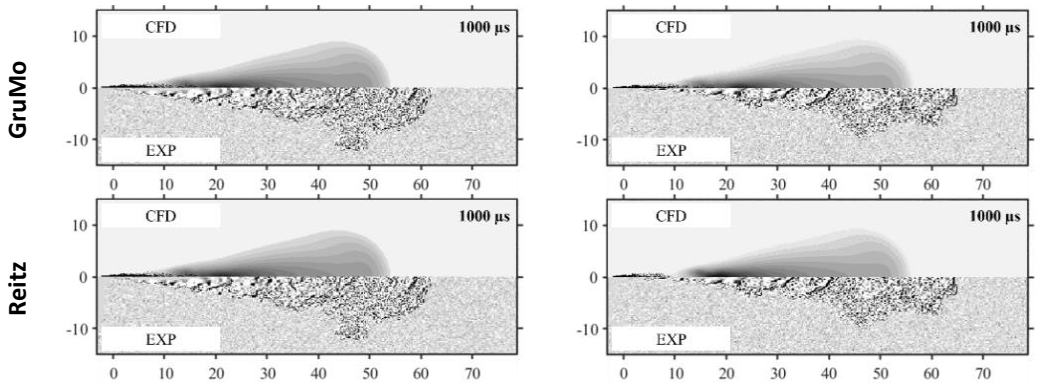

Figure 82. Effect of the secondary break-up model on the vapor jet, for Spray C (a) and Spray D (b).

As mentioned before, different parameters are investigated for the Spray A injector, such as the ambient density, the turbulence model, the minimum mesh size, the time-step, and the number of parcels introduced per time-step. Similarly to the approach described for gasoline injectors, in order to evaluate the effect of ambient density on the GruMo model in diesel injectors, three different operating conditions are tested. Also in this case, each condition is purposely calibrated against experimental data. Numerical results are validated against experimental data in terms of liquid penetration, as reported in Figure 83.

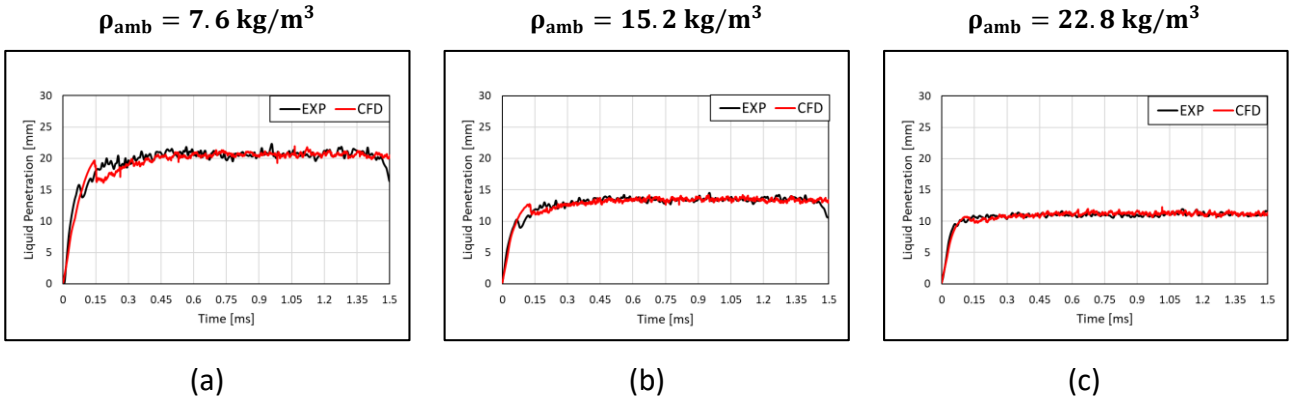

Figure 83. GruMo break-up model parameters as a function of the ambient density – diesel injectors.

As for the 7.6 kg/m^3 and 15.2 kg/m^3 conditions, no experimental vapor penetration curves were available. The GruMo model is able to reproduce the experimental outcomes in terms of liquid penetration for all the investigated ambient densities, thanks to a case-by-case tuning of the parameters. Linear trends of the model parameters are reported in Figure 84; in particular, the

value of C_{s1} is constant for all the investigated conditions, and equal to 0.5 (i.e. the default value used in the Reitz Diwakar model).

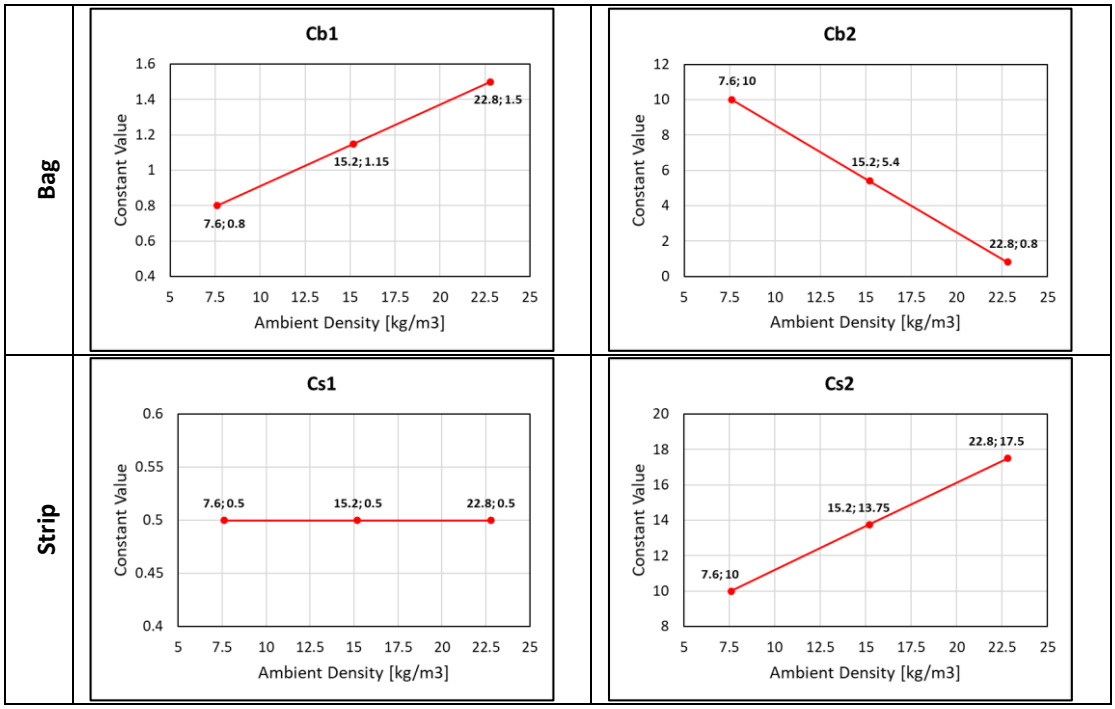

Figure 84. Comparison between experimental and numerical mass flow rates of the INJ1 for a back pressure of 1.0 bar(a) and a difference between rail and ambient of 100 bar.

The transition distance T_d is set to 8 mm in this case, since diesel injectors are characterized by operative conditions that broadly differ from the gasoline injectors one; the main consequence is that Spray A maximum liquid penetration (10-20 mm) is one order of magnitude smaller than the INJ1 one (80-100 mm). The value of 8 mm is chosen after an iterative calibration process, and it guarantees a good agreement between numerical and experimental outcomes for both the initial slope of the liquid penetration curve, and the static value. As previously described for gasoline injectors, analysis of We_g and $We_g/\sqrt{Re_d}$ quantities are carried out by means of Probability Density Function (PDF) and Cumulative Distribution Function (CDF), considering the droplets population at $5 \cdot 10^{-3}\ s$ after the start of injection; results of such study are reported in Figure 85.

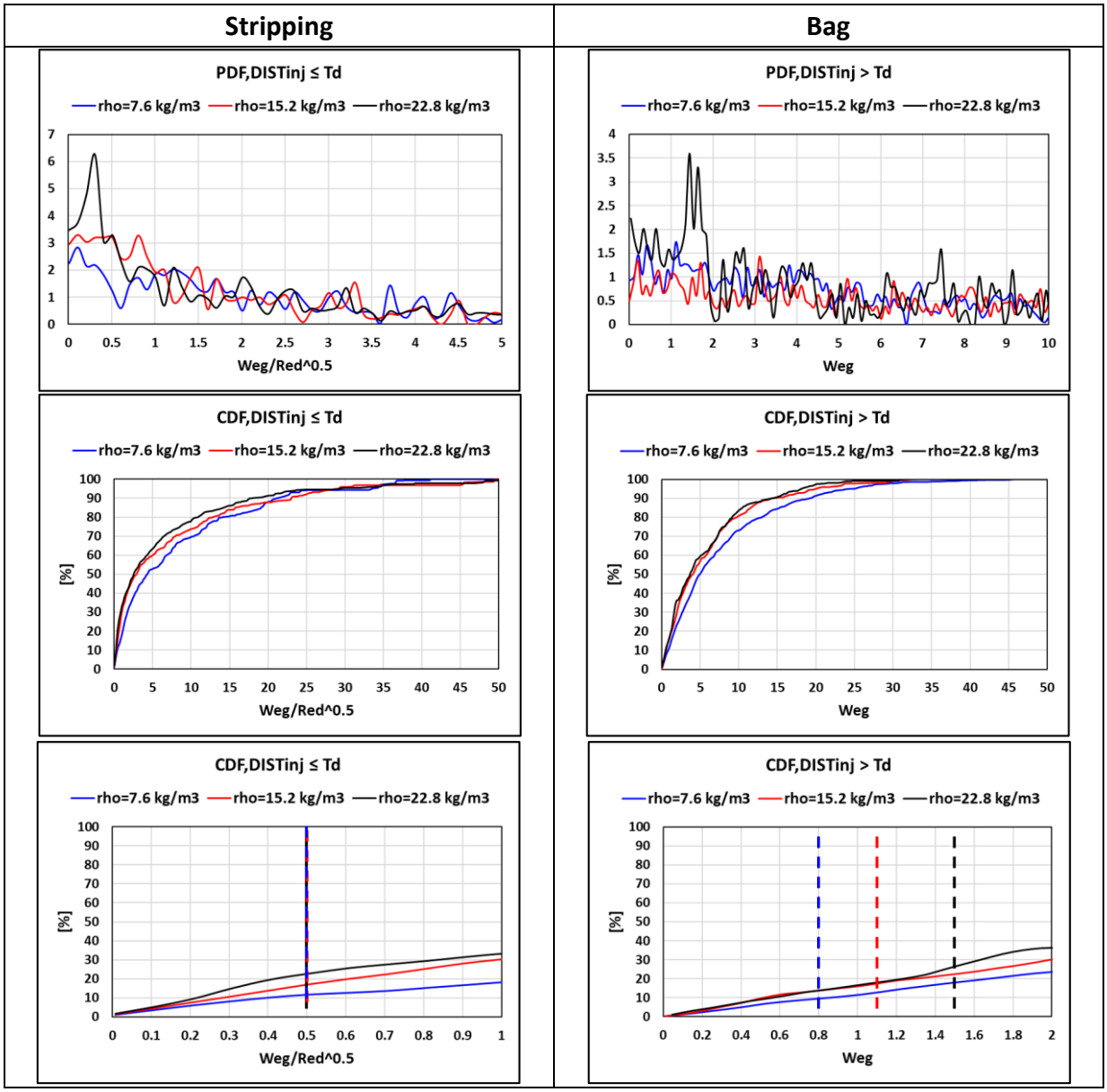

Figure 85. PDF and CDF analysis on the GruMo model for diesel injectors. On the bottom, details of the CDFs are reported and the dashed lines show the adopted values for C_{s1} and C_{b1}.

As for the C_{s1}, a differenttrend compared to gasoline injectors can be noticed. In fact, with the adoption of a T_d equal to 8 mm, a large percentage of droplet satisfies the condition of $We_g > \sqrt{Re_d}$, needed for stripping to take place. For that reason, it is not necessary to further reduce the value of C_{s1} to guarantee a proper break-up in the near nozzle region. On the other hand, simulation results for all the operative conditions shows a strong and not-linear dependency of the initial liquid penetration slope against small changes of C_{s1} value. For that reason, the latter is kept constant for all the ambient densities. As for the calibrated C_{s2} values, they allow a gradual break-

up within the transition distance, and they are not far from the default value used by Reitz and Diwakar [18],[54]. Focusing on the Bag mechanism, using a C_{b1} equal to 6 as in the original Reitz Diwakar model, break-up would occur for the 50-60 % of the droplets for all the ambient densities, leading to an overestimation of the static liquid penetration. For this reason, in the GruMo model, value of C_{b1} is set to 0.8, 1.15, and 1.5 for 7.6, 15.2, and 22.8 kg/m^3 cases, respectively. As for the C_{b2} parameter, values are chosen to ensure a proper break-up far from the nozzle tip, and the correlation is linear and inversely proportional with the ambient density (the C_{b2} decrease with the increase of the ambient density leads to a stronger break-up).

As for the turbulence treatment, a comparison between the k-ε Standard and the k-ε RNG model is carried out, in order to understand the effect on the spray development. At first, a comparison between numerical and experimental data is carried out in terms of both liquid and vapor penetration, as reported in Figure 86. Experimental and numerical snapshots of both liquid and vapor phase are reported in Figure 87 and Figure 88, respectively. As for the liquid penetration, both Standard and RNG model properly reproduce experimental data; in the case of the RNG model, a slight overshoot in the curve can be noticed around $2 \cdot 10^{-3}\ s$, meaning that the secondary break-up is underestimated in the first part of the injection. As for the vapor penetration, a slight improvement in the numerical results can be noticed by using the RNG model, since the value increase after $0.5 \cdot 10^{-3} s$. However, in the first stage of the injection, both Standard and RNG underestimate the experimental vapor penetration.

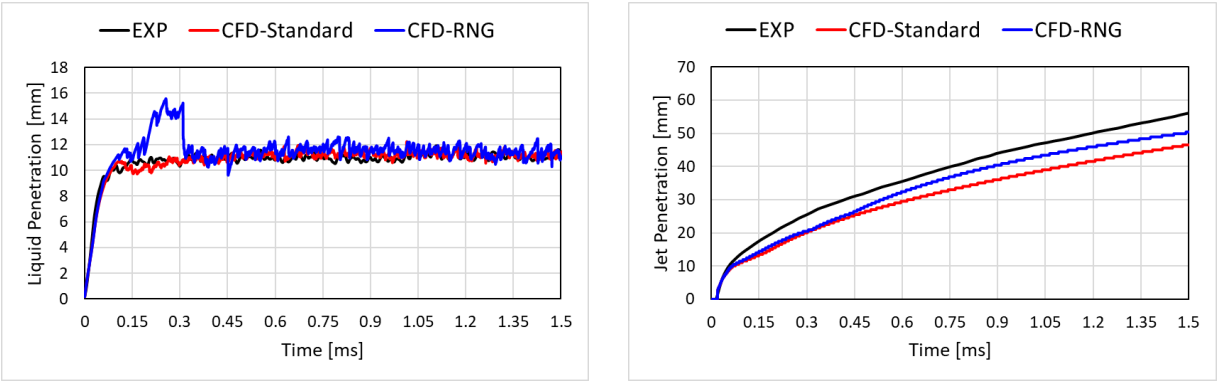

(a) (b)

Figure 86. Effect of turbulence model on (a) liquid penetration, and (b) vapor penetration in the Spray A.

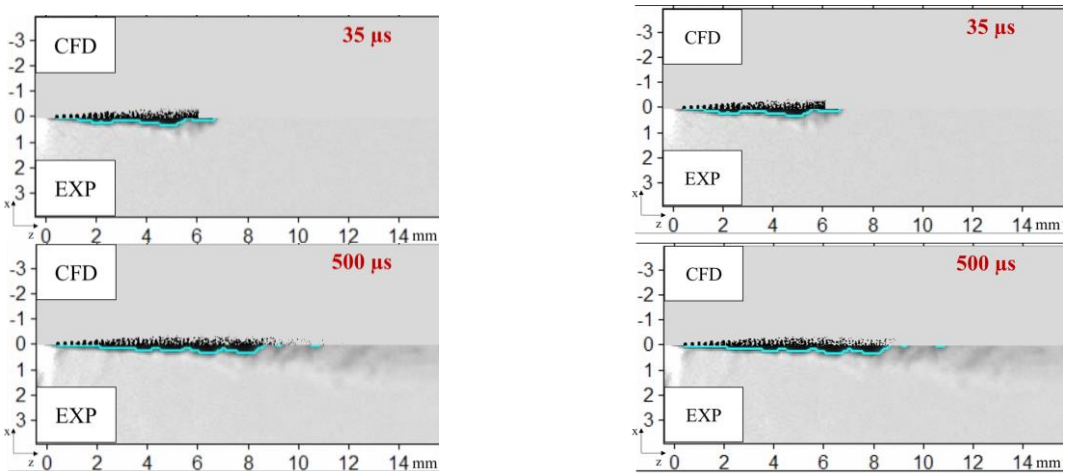

(a) (b)

Figure 87.Comparison in terms of liquid phase snapshots using (a) the k-ε Standard model, and (b) the k-ε RNG one in the Spray A.

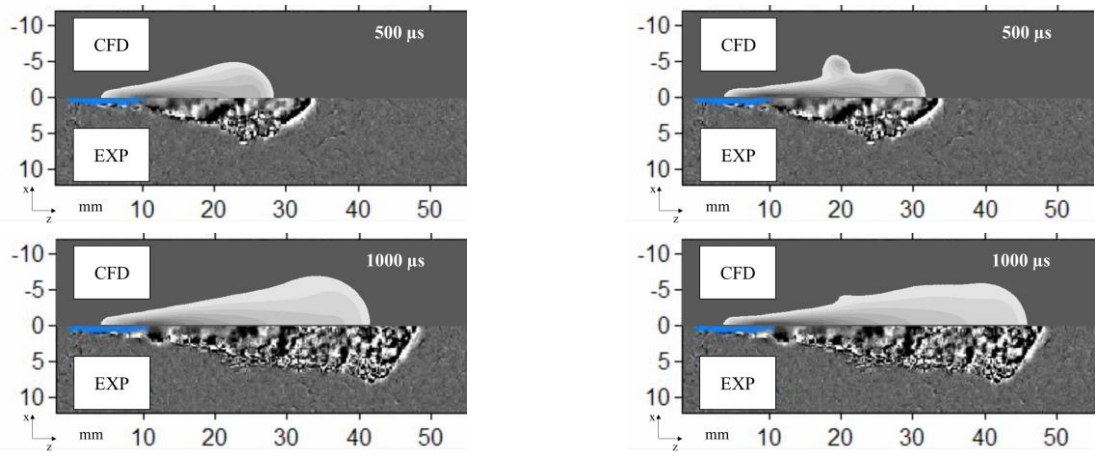

(a) (b)

Figure 88. Comparison in terms of vapor phase snapshots using (a) the k-ε Standard model, and (b) the k-ε RNG one in the Spray A.

As for the liquid images, no substantial differences can be depicted between the Standard model and the RNG one, while in the vapor comparison, the latter produces lateral waves in the vapor shape during the first stage of the injection, that cannot be noticed in the experimental image.

Finally, the effects of mesh size, parcel number, and time-step variation on both liquid and vapor penetration are exploited in Figure 89, 90, and 91 respectively. Number of injected parcels does not affect neither liquid penetration nor vapor one. Simulation time-step value has a slight effect on the transient stage of the injection, while no noticeable influence can be depicted for the vapor penetration. As for the mesh size, the effect on both liquid and vapor penetration is prominent: in fact, the larger is the cell volume, the smaller will be the change of gas velocity due to momentum exchange with liquid drops. On the other hand, if the mesh resolution is high, the gas velocity increases faster. In the case of small grid sizes, the droplets being injected at early times transfer their momentum to small gas volumes and cause a fast increase of gas velocity. Due to the smaller relative velocities, the next droplets are less decelerated, resulting in an increase of spray penetration. For this reason, spray penetration increases if the grid is refined, and decreases if a coarser grid is used. Moreover, it is possible to notice that 0.5 mm corresponds with the condition of 'mesh size convergence': in fact, further reduction of the grid size (i.e. 0.4 mm) does not involve a considerable change in both liquid and vapor penetration.

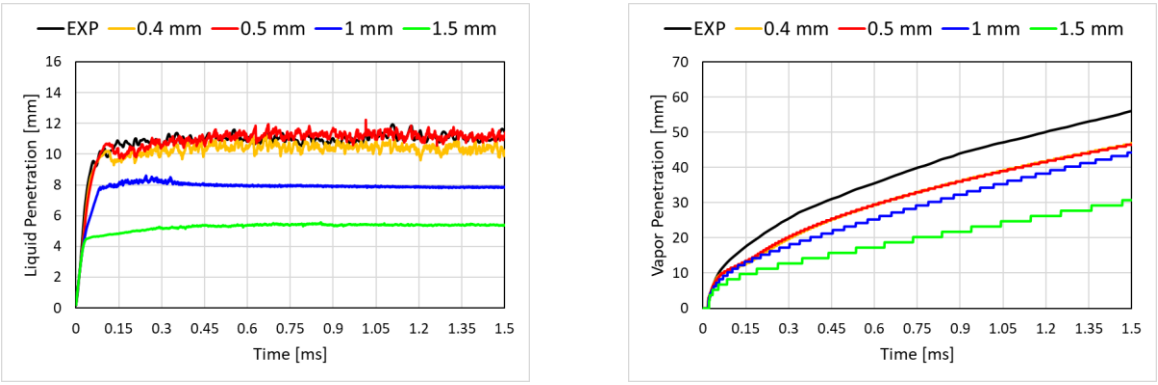

(a) (b)

Figure 89. Effect of mesh size on (a) liquid penetration, and (b) vapor penetration in the Spray A.

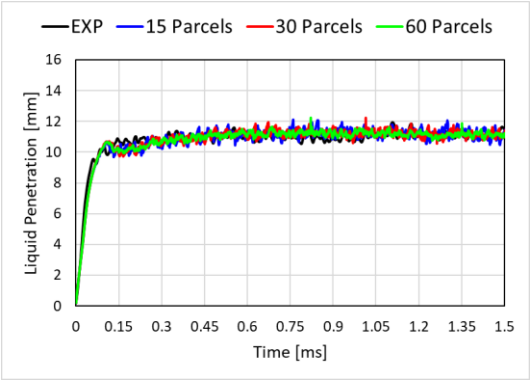

(a)

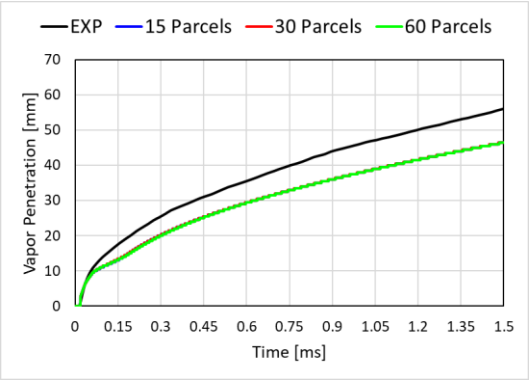

(b)

Figure 90. Effect of injected parcel number on (a) liquid penetration, and (b) vapor penetration in the Spray A.

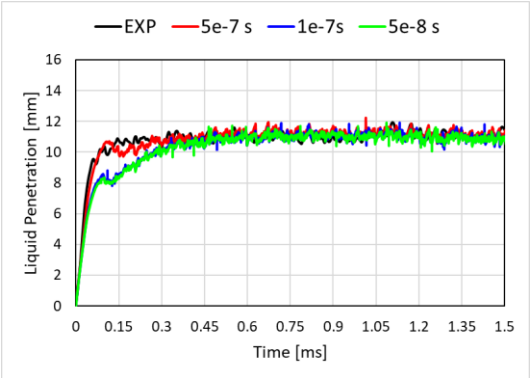

(a)

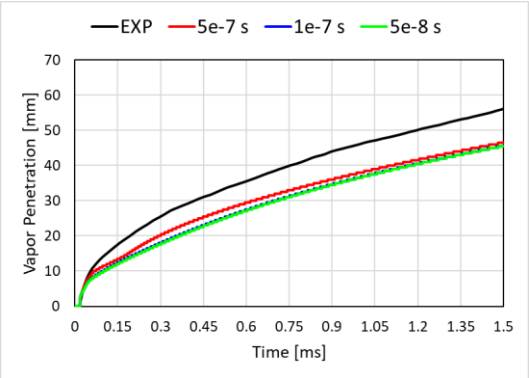

(b)

Figure 91. Effect of simulation time-step on (a) liquid penetration, and (b) vapor penetration in the Spray A.

7. Results – Flash-Boiling Model

As introduced earlier, the INJ2 is simulated under both standard and flashing conditions, with the aim to evaluate the new flash-boiling model implemented in the commercial code STAR-CD, licensed by Siemens. In the subcooled case, droplet initialization is based on experimental momentum and mass flow rate outcomes, while at flashing conditions the flash boiling atomization model automatically evaluates droplet properties at the nozzle exit. Reitz Diwakar secondary break-up model is calibrated in the subcooled case and then it's employed without variations in the flashing one, with the aim to evaluate the reliability of the flash-boiling breakup model contribution to the estimation of the reduction of droplet size due to bubbles burst inside the liquid droplets. A first comparison between experimental and numerical outcomes is carried out in terms of imaging. Three snapshots are chosen and reported in Figures 92 and 93. As visible from the imaging comparison, at subcooled conditions the main spray characteristics such as jet penetration and cone angle are well represented by the simulations; as for the flashing operating point, it is possible to state that there is a slight overestimation of the cone angle value even if the global morphology of the spray is well predicted. To quantitatively validate the numerical framework, a comparison between numerical and experimental liquid penetration curves is reported in Figure 94. Error bars are shown in the experimental curves to point out the standard deviation values. Numerical liquid penetrations closely reproduce experimental results in both cases; a slight underestimation of the penetration in the last stage of the injection is reported for the flashing case, due to the previously commented overestimation of the cone angle.

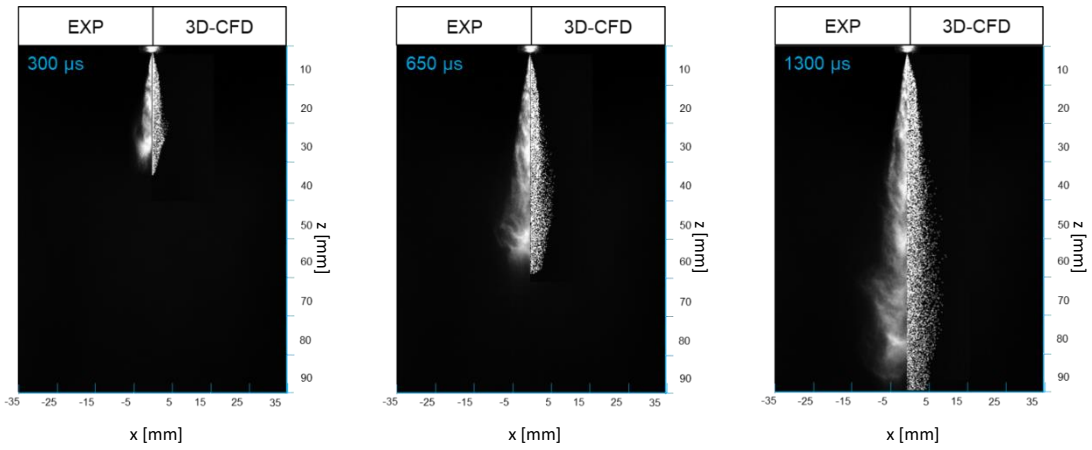

Figure 92. Comparison in terms of imaging between experimental outcomes and numerical simulations at (a) 300 µs, (b) 650 µs, and (c) 1300 µs after the start of injection at subcooled

conditions.

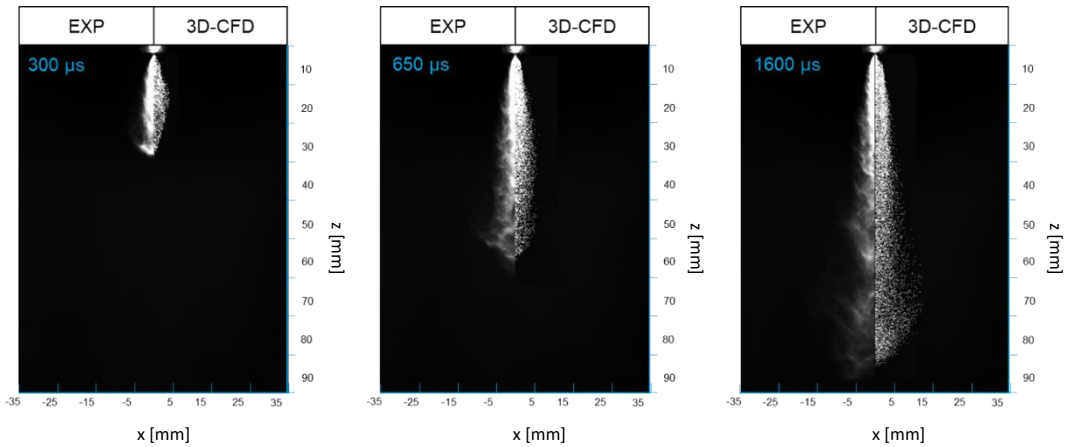

Figure 93. Comparison in terms of imaging between experimental outcomes and numerical simulations at (a) 300 µs, (b) 650 µs, and (c) 1300 µs after the start of injection at flashing conditions.

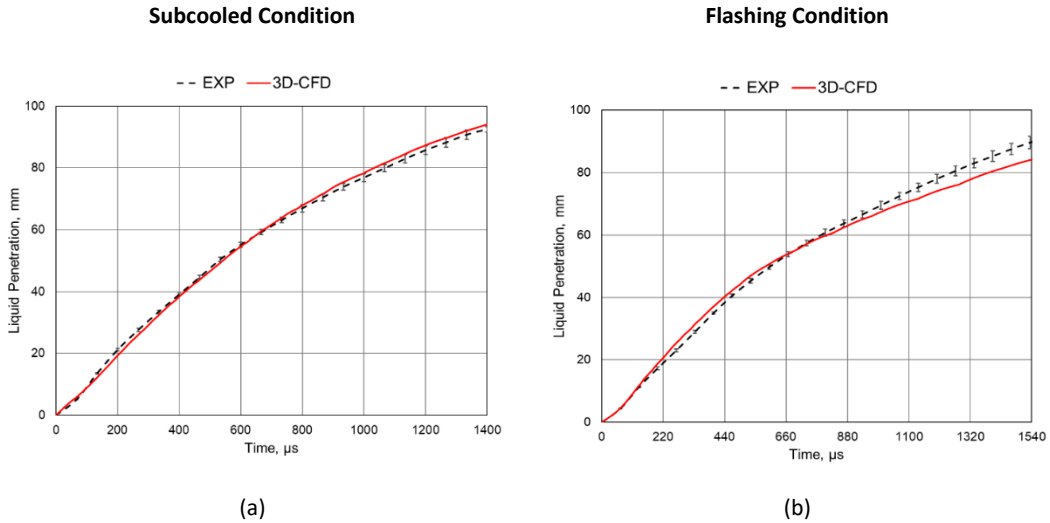

Figure 94. Liquid penetration comparison for (a) subcooled and (b) flashing cases.

Since a reduction of the droplet size is expected when flash boiling occurs, the last comparison is carried out in terms of PDA data. PDA analysis is carried out along the nozzle axis at 20 mm, 30 mm, 40 mm, and 50 mm far from the injector tip; comparisons between numerical and experimental mean droplet diameter (D10) and velocity magnitude are depicted in Figures 95 and

96. It can be seen that both D10 and velocity values are well predicted by the numerical simulations at all the measurement stations; it is useful to point out that PDA values are filtered in a time interval of $2 \cdot 10^{-3} s$ with the aim to analyse the characteristics of the spray in the static phase of the injection. As for the flashing case, the adopted model is able to predict the reduction of droplet diameters due to flashing along the axial direction.

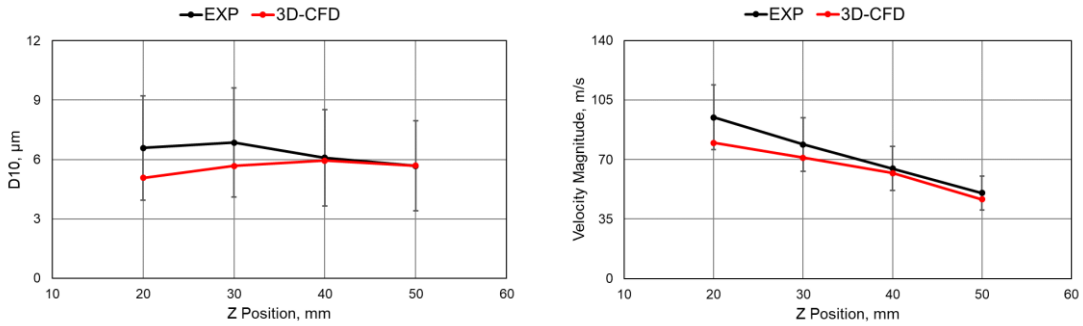

(a) (b)

Figure 95. Comparison between simulations and experiments in terms of (a) D10 and (b) velocity magnitude at subcooled condition.

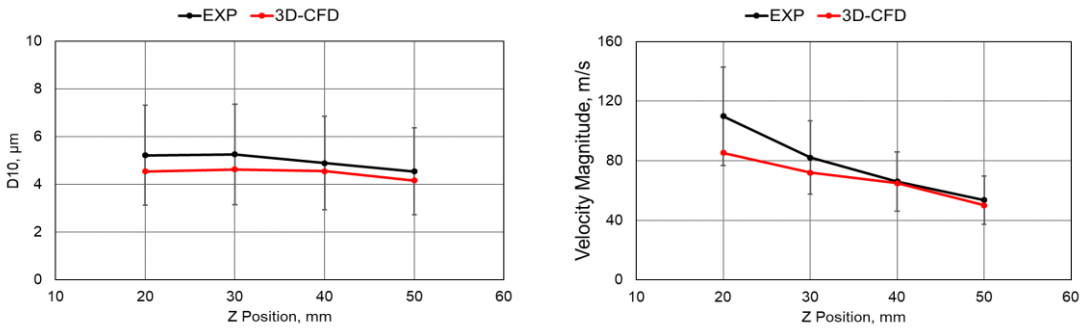

(a) (b)

Figure 96. Comparison between simulations and experiments in terms of (a) D10 and (b) velocity magnitude at flashing condition.

8. Conclusions

Spray modeling plays a fundamental role in 3D-CFD simulations as it affects the further air-fuel mixing process and combustion. Currently adopted Lagrangian method for the analysis of both gasoline and diesel injectors are influenced by lack of generality and predictive capability against parametric variations, such as the operative conditions and the nozzle architecture. Physical phenomena such as droplets break-up and evaporation, are strongly influenced by both injection and ambient conditions, by the fuel properties, and by the injector geometry. Moreover, injectors are usually validated by experiments and numerical simulations in quiescent vessels, in which a mixing fan ensures uniform ambient conditions and a neglectable air motion at the start of injection; on the other hand, during an ICE operating cycle, the charge motion is prevalent and allows a proper air-mixing throughout the combustion chamber, while the ambient conditions in terms of temperature and pressure quickly change and cannot be considered as uniform in the chamber at the start of injection.

The main objective of this research activity was to formulate an extensive methodology for the numerical characterization of the injection process for both GDI (Gasoline Direct Injection) and Diesel engines, characterized by the introduction of fuel directly into the engine cylinder. In particular, the attention was focused on three different phenomena, namely primary break-up, secondary break-up, and flash-boiling, which play a significant role in the spray development.

At first, the impact of the primary break-up simulation in GDI sprays is addressed. Atomization modeling in common industrial practice often relies on the adoption of droplet diameter distribution functions inherited from experimental PDA data. However, for the sake of validity of the latter, measurements are usually carried out at least 15-20 mm away from the injector tip, where droplets have already undergone the secondary break-up. Therefore, droplet initial diameters adopted in Lagrangian simulations are characterized by values even one order of magnitude smaller than nozzle hole diameters. Even if questionable, such an approach is able to provide numerical results in line with experimental ones if the backpressure is close to the ambient one. For this purpose, Lagrangian simulations at ambient conditions and different injection pressures are carried out on a 5-hole GDI prototype injector, named INJ3. Such simulations are characterized by initial droplet diameters lower than 10 μm and inherited from experimental PDA data. The same atomization strategy is also applied to the well-known Spray G

injector, characterized by a backpressure equal to 0.6 MPa. In this case, the adoption of small diameters (nearly 10 μm) coming from tests is responsible for relevant misalignments with reference to the experimental outcomes. In fact, unlike experimental evidence, the numerical spray tends to collapse similarly to flash boiling conditions. Therefore, larger droplet diameters (closer to the hole size of 165 μm) are tested, able to provide a representation of the spray in line with the experiments. In order to confirm the importance of choosing droplet diameters comparable with the hole size, an internal nozzle flow simulation of the Spray G is carried out. Such a simulation provides relevant information on droplet initial conditions to be applied in the Lagrangian simulations, particularly in terms of droplet diameters. These last are found to be slightly larger than 130 μm, thus similar to nozzle hole dimension and one order of magnitude larger than values provided by PDA measurements 15 mm away from the injector tip. Therefore, compared to droplet distribution functions inferred from experiments (or even poorly predictive atomization models), a simple blob model with droplet size equal to hole diameter, together with a proper secondary break-up model, may better perform in terms of 3D-CFD numerical results.

Moving on the secondary break-up analysis, the alternative GruMo model is proposed with the aim to minimize the case-by-case tuning effort usually required with strong variations of injection parameters and ambient conditions, for both gasoline and diesel sprays. The proposed approach is similar to the widely adopted Reitz-Diwakar model but, compared to the latter, it is characterized by a zonalization of the break-up regimes in order to simplify and speed up its calibration. Moreover, model constants become variable parameters based on the operating conditions. In order to simplify the approach (at least at this stage), here the attention is limited to the effect of the ambient density, which is one of the most impacting variables on the spray behaviour and, thus, on the tuning parameters. Two different sets of model parameters are proposed for gasoline and diesel injectors, as the operative conditions drastically change in terms of injection pressure, fuel properties, and ambient pressure. Gasoline model parameters are calibrated via constant volume vessel simulations on a single-hole GDI research injector, named INJ1, using a complete experimental dataset consisting of injection rate, spray imaging and PDA data; on the other hand, diesel model parameters are calibrated on the well-known Spray A injector provided by ECN, validating numerical simulations with experimental outcomes in terms of both liquid and vapor penetration, and spray imaging. Both sets of model parameters are found to be linear functions of the ambient density. A detailed analysis based on Weber number allows to explain the reason of the values assumed by the model parameters after the calibration process

at the different conditions. The proposed model is then validated on the INJ2 and INJ3 for the gasoline version, and on the Spray C and Spray D for the diesel one. It is important to point out that the only difference between the analysed operations for the calibration of the model, consists in the ambient density, in order to isolate the effect of the latter. Injection parameters as well as gas temperature are kept constant. For all the injectors primary break-up is simulated with a blob model, and effective initial diameters and velocities are evaluated from the nozzle hydraulic coefficients. The same operating points and injectors are simulated with the Reitz-Diwakar and KHRT models as well, both adopted with constants that are fixed (regardless the conditions) and inherited from their respective reference papers. Despite the two consolidated models are effective in some cases, the GruMo approach is shown to perform sensibly better. Moreover, the use of the Reitz-Diwakar and KHRT models confirms the impossibility to obtain reliable estimations of droplet diameter and velocity at different conditions with a unique set of calibration constants. This supports the adoption of variable parameters in the proposed GruMo model. As for the Diesel injectors, numerical results for Spray A, Spray C, and Spray D, show an underestimation of the vapor penetration using both the GruMo model and the Reitz one. For this reason, an extensive investigation on both numerical and physical parameters is carried out on the Spray A. Focusing on the turbulence treatment, the k-ε RNG model is capable to reduce the underestimation of the vapor penetration in the axial direction, compared to the k-ε Standard; on the other hand, it shows a misalignment with experimental data in the first stage of the injection in terms of liquid penetration and vapor contour. As for the mesh size, simulations show that the computational grid with characteristic dimension of 0.5 mm, represent a convergence point since a further reduction of the minimum size does not involve a considerable change in both liquid and vapor penetration. Finally, the total number of injected parcels, and the simulation time-step, do not significantly affect the vapor penetration value.

The last activity of this work consists in the validation of a flash boiling model to be adopted in Lagrangian simulations, implemented in the last version of the commercial code STAR-CD, and performed on the INJ2. Numerical results are validated against experimental outcomes provided by SprayLAB of Perugia University, and droplet initial conditions are inherited from experimental momentum measurements. For both subcooled and flashing conditions, numerical results show a good agreement with experimental data, in terms of imaging, liquid penetration and PDA data (D10 and velocity magnitude). As for the flash boiling atomization model, a slight overestimation of the cone angle in the flashing case can be noticed, according to the imaging

comparison. This is confirmed by the penetration curves where, in the flashing case, a slight underestimation of the liquid length emerges. As demonstrated by the comparison between numerical and experimental values of D10, the flash boiling breakup model is able to predict the reduction of droplets size along the envelope of the spray due to vapor bubble nucleation and burst inside the liquid droplets.

Bibliography

[1] Cracknell, R., et al., Assessing the Efficiency of a New Gasoline Compression Ignition (GCI) Concept, SAE International; 2020.

[2] Lawler B, Lacey J, Güralp O, Najt P, Filipi Z. HCCI combustion with an actively controlled glow plug: The effects on heat release, thermal stratification, efficiency, and emissions. Appl Energy 2018; 211:809–19.

[3] Serrano D, et al. Ultra-Lean Pre-Chamber Gasoline Engine for Future Hybrid Powertrains. SAE Int J Adv Curr Prac Mobility 2019;2(2):607–22.

[4] Benajes J, Novella R, Gomez-Soriano J, Martinez-Hernandiz PJ, Libert C, Dabiri M. Evaluation of the passive pre-chamber ignition concept for future high compression ratio turbocharged spark-ignition engines. Appl Energy 2019; 248:576–88.

[5] Paltrinieri, S., et al., Water Injection Contribution to Enabling Stoichiometric Airto-Fuel Ratio Operation at Rated Power Conditions of a High-Performance DISI Single Cylinder Engine. SAE International; 2019.

[6] Komatsu, M. and T. Takaoka, Development of Toyota Plug-In Hybrid System. SAE International; 2011.

[7] Amer, A.a.R., T., Multidimensional Optimization of In-Cylinder Tumble Motion for the New Chrysler Hemi, in Spring Fuels & Lubricants Meeting & Exhibition, SAE, Editor; 2002.

[8] Yanzhe S, et al. The Optimization of Intake Port using Genetic Algorithm and Artificial Neural Network for Gasoline Engines. SAE Technical Papers 2015;2015.

[9] Gaikwad, S., Arora, K., Korivi, V., Cho, S., Steady and Transient CFD Approach for Port Optimization, in SAE World Congress & Exhibition; 2009, SAE.

[10] Das, S., S.-I. Chang, Kirwan, J. Spray Pattern Recognition for Multi-Hole Gasoline Direct Injectors Using CFD Modeling; 2009, SAE International.

[11] Kim T, Park S. Optimizing injector nozzle hole layout of a direct-injection spark ignition engine for wide open throttle condition. Energy Convers Manage 2019; 181:59–67.

[12] Basha, S.A. and K. Raja Gopal, In-cylinder fluid flow, turbulence, and spray models—A review. Renewable and Sustainable Energy Reviews, 2009. 13(6): p. 1620-1627.

[13] D. Gosman, A. and D. Clerides, Diesel Spray Modelling: A Review. 1998.

[14] Liao, Y. and D. Lucas, A literature review of theoretical models for drop and bubble breakup in turbulent dispersions. Chemical Engineering Science, 2009. 64(15): p. 3389-3406.

[15] Saha, K., Agarwal, A.K.,Ghosh, K., Som, S., Two-Phase Flow for Automotive and Power Generation Sectors. 2018: Springer.

[16] Subramaniam, S., Lagrangian–Eulerian methods for multiphase flows. Progress in Energy and Combustion Science, 2013. 39(2): p.215-245.

[17] Sparacino, S.; Berni, F.; d'Adamo, A.; Krastev, V.K.; Cavicchi, A.; Postrioti, L. Impact of the Primary Break-Up Strategy on the Morphology of GDI Sprays in 3D-CFD Simulations of Multi-Hole Injectors. Energies 2019, 12, 2890. https://doi.org/10.3390/en12152890.

[18] Reitz, R.D.; Diwakar, R. Effect of Drop Breakup on Fuel Sprays. SAE Int. 1986.

[19] Patterson, M.A.; Reitz, R.D. Modeling the Effects of Fuel Spray Characteristics on Diesel Engine Combustion and Emission. SAE Int. 1998.

[20] P. Aleiferis et al., Combustion and Flame, Vol. 157 (4), 735-756, 2010, doi.org/10.1016/j.combustflame.2009.12.019

[21] M. Xu et al., SAE Int. J. Fuels Lubr., Vol. 6 (1), 137-148, 2013, doi.org/10.4271/2013-01-1614

[22] W. Shengqi, M. Xu et al., ILASS Americas 25th Annual Conference, Pittsburgh, PA, May 2013

[23] P. Aleiferis et al., Fuel Vol. 105, 143–168, 2013, doi.org/10.1016/j.fuel.2012.07.044

[24] E. Sher et al., Progress in Energy and Combustion Science, Vol 34 (4), 417-439, 2008.

[25] P. Aleiferis, et al., International Journal of Heat and Mass Transfer, vol. 53, 4588–4606, 2010, doi.org/10.1016/j.ijheatmasstransfer.2010.06.033

[26] J. Serras-Pereira et al., "Cavitation, primary break-up and flash boiling of gasoline, iso-octane and n-pentane with a real-size optical direct-injection nozzle" Fuel, vol. 89, 2592–2607, 2010, doi.org/10.1016/j.fuel.2010.03.030

[27] Postrioti, L.; Cavicchi, A.; Brizi, G.; Berni, F.; Fontanesi, S. Experimental and Numerical Analysis of Spray Evolution, Hydraulics and Atomization for a 60 MPa Injection Pressure GDI System. SAE Int. 2018.

[28] A. Cavicchi et al., Fuel, Volume 263, 2020, 116657, ISSN 0016-2361. doi.org/10.1016/j.fuel.2019.116657

[29] A. Cavicchi, S. Sparacino, F. Berni, L. Postrioti, S. Fontanesi. AIP Conference Proceedings, 2191, art. no. 020043, 2019, doi.org/10.1063/1.5138776.

[30] Siemens, Star-CD v. 2019.1 User Guide

[31] Launder, B.E., and Spalding, D.B. 1974. 'The numerical computation of turbulent flows', Comp. Meth. in Appl. Mech. and Eng., 3, pp. 269-289.

[32] Rodi, W. 1979. 'Influence of buoyancy and rotation on equations for the turbulent length scale', Proc. 2nd Symp. on Turbulent Shear Flows.

[33] El Tahry, S.H. 1983. 'k-ε equation for compressible reciprocating engine flows', AIAA, J. Energy, 7(4), pp. 345–353.

[34] Yakhot, V. and Orszag, S.A. 1986. 'Renormalization group analysis of turbulence — I: Basic theory', J. Scientific Computing, 1, pp. 1–51.

[35] Yakhot, V., Orszag, S.A., Thangam, S., Gatski, T.B. and Speziale, C.G. 1992. 'Development of turbulence models for shear flows by a double expansion technique', Phys. Fluids, A4(7), pp. 1510–1520.

[36] Norris, L.H. and Reynolds, W.C. 1975. 'Turbulent channel flow with a moving wavy boundary', Report No. FM–10, Department of Mechanical Engineering, Stanford University, USA.

[37] Rodi, W. 1991. 'Experience with two-layer models combining the k-ε model with a one-equation model near the wall', AIAA-91–0216.

[38] Papp, J. L., Ghia, K. N. 1999. 'Modification of the High-Re RNG k-e Turbulence model for Low-Re, Near-Wall Effects', 30th AIAA Fluid Dynamics Conference, AIAA 99-3700.

[39] Menter, F.R. 1993. 'Zonal two equation k-ω turbulence models for aerodynamic flows', Proc. 24th Fluid Dynamics Conf., Orlando, Florida, USA, 6-9 July, Paper No. AIAA 93-2906.

[40] Bracco, F.V. 1985. 'Modeling of engine sprays', SAE Technical Paper Series 850394.

[41] Gosman, A.D. and Ioannides, S.I. 1983. 'Aspects of computer simulation of liquid-fuelled combustors', AIAA, J. Energy, 7(6), pp. 482–490.

[42] Milne-Thompson, L.M. 1968. "Theoretical Hydrodynamics". 5th edition, McMillan & Co., New York.

[43] Bird, R.B., Stewart, E.W., and Lightfoot, E.N. 1966. "Transport Phenomena". John Wiley & Sons, New York.

[44] C. W. Hirt and B. D. Nichols. 1981. "Volume of Fluid (VOF) Method for the Dynamics of Free Boundaries", J. Comput. Phys., 39, pp. 201-225.

[45] J. Manin, Y. Jung, S.A. Skeen, L.M. Pickett, S.E. Parrish, and L. Markle. Experimental characterization of DI gasoline injection processes. SAE Technical Paper, 2015-01-1894, 2015.

[46] P. Strek, D. Duke, A. Swantek, A. Kastengren, C.F. Powell, and D.P. Schmidt. X-Ray radiography and CFD studies of the Spray G injector. SAE Technical Paper, 2016-01-0858, 2016.

[47] Duke, D.J.; Kastengren, A.L.; Matusik, K.E.; Swantek, A.B.; Powell, C.F.; Payri, R.; Vaquerizo, D.; Itani, L.; Bruneaux, G.; Grover, R.O., Jr.; et al. Internal and Near Nozzle Measurements of Engine Combustion Network "Spray G" Gasoline Direct Injectors. Exp. Therm. Fluid Sci. 2017, 88.

[48] Parrish, S.E. Evaluation of Liquid and Vapor Penetration of Sprays from a Multi-Hole Gasoline Fuel Injector Operating Under Engine-Like Conditions. SAE Int. 2014.

[49] Payri, R.; Salvador, F.J.; Martí-Aldaraví, P.; Vaquerizo, D. ECN Spray G external spray visualization and spray collapse description through penetration and morphology analysis. Appl. Therm. Eng. 2017, 112, 304–316.

[50] Payri, R.; Gimeno, J.; Marti-Aldaravi, P.; Vaquerizo, D. Momentum Flux Measurements on an ECN GDi Injector. SAE Int. 2015.

[51] Engine Combustion Network. Available online: https://ecn.sandia.gov

[52] Postrioti Lucio, Battistoni Michele, Ungaro Carmine, Mariani Alessandro. Analysis of Diesel Spray Momentum Flux Spatial Distribution. SAE Int J Engines 2011;4(1): 720–36.

[53] Postrioti, L., et al., Momentum Flux Measurement on Single-Hole GDI Injector under Flash-Boiling Condition. Vol. 24; 2015.

[54] Reitz, Rolf. (1987). Modeling atomization processes in high-pressure vaporizing sprays. Atomisation Spray Technology. 3. 309-337.

[55] Hiroyasu H., Arai M. (1990) Structures of Fuel Sprays in Diesel Engines, SAE International, SAE paper 900475.

[56] Cavicchi A, et al. Evaluation of the single jet flow rate for a multi-hole GDI nozzle. in AIP Conference Proceedings. 2019.

[57] Nicholls, J.A. 1972. 'Stream and droplet breakup by shock waves', in NASA SP–194 (Eds. D.T. Harrje and F.H. Reardon), pp. 126–128.

[58] Senecal, P.K., Richards, K.J., Pomraning, E., Yang, T., Dai, M.Z., McDavid, R.M., Patterson, M.A., Hou, S. and Shethaji, T. 2007. 'A New Parallel Cut-Cell Cartesian CFD Code for Rapid Grid Generation Applied to In-Cylinder Diesel Engine Simulations', SAE Paper 2007-01-0159.

[59] C., B., Mixture Formation in Internal Combustion Engines; 2006: Springer.

[60] Pilch M, Erdman CA. Use of breakup time data and velocity history data to predict the maximum size of stable fragments for acceleration-induced breakup of a liquid drop. Int J Multiph Flow 1987;13(6):741–57.

[61] Reitz, R.D. Diwakar, R. Structure of High-Pressure Fuel Sprays. SAE International; 1987.

[62] Braga RM, et al. 3D Numerical Characterization of a Multi-Holes Injector in a Quiescent Vessel and Its Application in a Single-Cylinder Research Engine Using Ethanol. SAE International; 2017.

[63] XIN J, RICART L, REITZ RD. Computer Modeling of Diesel Spray Atomization and Combustion. Combust Sci Technol 1998;137(1-6):171–94.

[64] Hiroyasu H, Arai M, Shimizu M. Break-up length of a liquid jet and internal flow in a nozzle. ICLASS-91 1991:275–82.

[65] Ren Yi, Li Xianguo. Assessment and validation of liquid breakup models for highpressure dense diesel sprays. Front Energy 2016;10(2):164–75.

[66] Malaguti Simone, Fontanesi Stefano, Cantore Giuseppe, Montanaro Alessandro, Allocca Luigi. Modellingof primary breakup process of a gasoline direct engine multi-hole spray. Atomizat Sprays 2013;23(10):861–88.

[67] Wang, X., Zhao, H. Numerical Simulation of the Gasoline Spray with an Outward- Opening Piezoelectric Injector: A Comparative Study of Different Breakup Models; 2018, SAE International.

[68] Reitz Rolf D, Beale Jennifer C. Modeling spray atomization with the Kelvin- Helmholtz/Rayleigh-Taylor hybrid model. Atomization Sprays 1999;9(6):623–50.

[69] Brulatout Jonathan, Garnier François, Mounaïm-Rousselle Christine, Seers Patrice. Calibration strategy of diesel-fuel spray atomization models using a design of experiment method. Int J Engine Res 2016;17(7):713–31.

[70] Costa M, Sorge U, Allocca L. CFD optimization for GDI spray model tuning and enhancement of engine performance. Adv Eng Softw 2012; 49:43–53.

[71] Nsikane, D., K. Vogiatzaki, Morgan, R. Predictive Engine Simulations based on a novel DoE/RANS approach with coefficient tabulation; 2019.

[72] Van Dam Noah, Rutland Christopher. Adapting diesel large-eddy simulation spray models for direct-injection spark-ignition applications. Int J Engine Res 2016;17 (3):291–315.

[73] Arcoumanis, C., Gavaises, M. French, B. Effect of Fuel Injection Processes on the Structure of Diesel Sprays. SAE International; 1997.

[74] Rabin E., S.A.R., Lowhead R. B., Displacement and shattering of propellant droplets. Rocketdyne Propulsion Field Lab; 1960.

[75] Wierzba A. Deformation and breakup of liquid drops in a gas stream at nearly critical Weber numbers. Exp Fluids 1990;9(1-2):59–64.

[76] C. Price et al., Atomization and Sprays, 26 (12) pp. 1197-1239, 2016 doi.org/10.1615/AtomizSpr.2016015807

[77] C. Price et al., Fuel 221, pp.518-541, 2018, doi.org/10.1016/j.fuel.2018.01.088

[78] J. Senda, ICLASS 2018, ID 432

[79] M. Adachi et al., JSAE Review, vol. 17, pp. 231-237, 1996, doi.org/10.1016/0389-4304(96)00025-2

[80] J. Senda, Y. Hojyo, H. Fujimoto, SAE Technical Paper 941925, 1994, doi.org/10.4271/941925

[81] Schmidt, D., and F. Bedford, "An Analysis of the Convergence of Stochastic Lagrangian/Eulerian Spray Simulations". Vol. 102. 2018.

[82] Y. Han, Z., and R. Reitz, "Turbulence Modeling of Internal Combustion Engines Using RNG κ-ϵ Models". Vol. 106. 1995. 267-295.

[83] Linstrom, P.J.; Mallard, W.G. NIST Chemistry WebBook; National Institute of Standards and Technology: Gaithersburg, MD, USA, 2017.

[84] Zhao, H.; Quan, S.; Dai, M.; Pomraning, E.; Senecal, P.K.; Xue, Q.; Battistoni, M.; Som, S. Validation of a Three-Dimensional Internal Nozzle Flow Model Including Automatic Mesh Generation and Cavitation Effects; ASME: New York, NY, USA, 2014; Volume 136.

[85] Cicalese, G.; Berni, F.; Fontanesi, S. Integrated in-cylinder/CHT methodology for the simulation of the engine thermal field: An application to high performance turbocharged DISI engines. SAE Int. J. Engines 2016, 9.

[86] Cicalese, G.; Berni, F.; Fontanesi, S.; D'Adamo, A.; Andreoli, E. A Comprehensive CFD-CHT Methodology for the Characterization of a Diesel Engine: From the Heat Transfer Prediction to the Thermal Field Evaluation. In Proceedings of the International Powertrains, Fuels & Lubricants Meeting, Beijing, China, 16–19 October 2017.

[87] Berni, F.; Cicalese, G.; D'Adamo, A.; Fontanesi, S. Critical aspects on the use of thermal wall functions in CFD in-cylinder simulations of spark-ignition engines. SAE Int. J. Commer. Veh. 2017, 10.

[88] Berni, F.; Cicalese, G.; Fontanesi, S. A modified thermal wall function for the estimation of gas-to-wall heat fluxes in CFD in-cylinder simulations of high-performance spark-ignition engines. Appl. Therm. Eng. 2017, 115, 1045–1062.

[89] Schnerr Professor Dr.-Ing.habil, G., Physical and Numerical Modeling of Unsteady Cavitation Dynamics. 2001.

[90] Allocca, L., et al., ECN Spray G Injector: Assessment of Numerical Modeling Accuracy. 2018, SAE International.

[91] Sim, J., et al., Spray Modeling for Outwardly-Opening Hollow-Cone Injector. 2016.

[92] Postrioti, L.; Bosi, M.; Gioia, R.D.; Bonandrini, G. GDI spray evolution and sizing characteristics in Flash-Boiling conditions. In International Congress: SIA Powertrain; SIA: Versailles, France, 2015.

[93] Third International Workshop of The Engine Combustion Network. 2014. Available online: https://ecn.sandia.gov/ecn-workshop/ecn3-proceedings